Design, Analysis, and Implementation of Multi-port Refraction Based Electro-Optic Switches

Yiying Zuo
Photonic Systems Group
McGill University

Your file Votre référence
ISBN: 978-0-494-32339-7
Our file Notre référence
ISBN: 978-0-494-32339-7

Index

List of Figures

List of Tables

Abstract

Electro-optic (EO) beam deflectors are voltage-controlled devices widely used for scanning and switching applications. For example, high-speed, low-loss optical switches aimed at future optical networks can be built on EO deflectors. Novel EO deflectors distinguish themselves with a much-improved steering performance, high-speed response and simple fabrication requirements. Patterned ferroelectric crystals such as $LiTaO_3$ are first poled to provide the required prism shaped domain structures. The application of an electrical field across the entire crystal can then be used to drive the trajectory of the beam as it travels through the poled wafer. The electric field induces an index change of opposite magnitude on the adjacent domain regions in the EO device, causing the optical beam to refract at the interfaces.

Although rectangular geometry is extensively employed in EO devices, nonrectangular scanners have demonstrated better deflection performance. Two new nonrectangular geometries capable of further enhancing the deflection performance of EO beam scanners, proposed in this dissertation, were constructed. Their parabola and half-horn geometries provide 2-3 degrees of steering, which is 2 – 3 times greater than the steering provided by rectangular deflectors.

EO deflectors based on the parabola and the half-horn geometries, which can provide larger deflection angles, were built. These devices demonstrated a deflection angle of 3.1°, less than 5 dB of insertion loss from fiber to fiber, and -40 dB of crosstalk.

Two packaged optical switches using rectangular EO deflectors were demonstrated. By combining these EO deflectors with fiber collimators and high voltage packaging, high speed optical switches were built and characterized. The switch design was based on a 500μm z-cut $LiTaO_3$ single crystal wafer fabricated using the domain inversion method. The 1x2 switch had a maximum deflection angle

of 1.22° with an applied voltage of 1.1 kV and the 1x4 switch had a maximum deviation angle of 2.14°, with an applied voltage of 1 kV. The average insertion loss and crosstalk figures were 2.36 dB and -36 dB, respectively. The worst case switching time was 86 ns.

Résumé

Les déflecteurs de faisceaux électro-optiques (EO) sont des dispositifs activés par une tension qui sont largement utilisés dans des applications de balayage optique et de commutation. Par exemple, des commutateurs optiques à haute-vitesse et faible pertes, destinés aux futurs réseaux optiques, peuvent être construits à partir de déflecteurs EO. De nouveaux types de déflecteurs EO se distinguent par des angles de déviation bien supérieurs, une réponse très rapide et une grande simplicité de fabrication. Certains domaines d'un cristal ferro-électrique tel le $LiTaO_3$ sont d'abord inversés sous l'influence d'un champ électrique, pour produire des structures constituées de prismes. L'application d'un champ électrique sur la totalité du cristal permet ensuite de modifier la trajectoire d'un rayon lumineux traversant les structures de prismes. Le champ électrique crée des modification de l'indice de réfraction de magnitude opposée dans les domaines adjacents du dispositif EO, causant une réfraction du rayon aux interfaces.

Même si des géométries rectangulaires ont été abondamment utilisées dans des dispositifs électro-optiques, des structures non-rectangulaires ont démontré une meilleure performance de déflection. Deux géométries non-rectangulaires capables d'améliorer la performance de déflection de dispositifs EO sont présentées dans cette thèse, et ont été implémentées. Leurs géométries à base de parabole et de demi-cor leur permettent d'accomplir des déviations de 2 à 3 degrés, ce qui est deux à trois fois mieux qu'avec des déflecteurs rectangulaires.

Des déflecteurs EO, basés sur des géométries de parabole ou de demi-cor, ayant un potentiel de déflection important, ont été construits. Ces dispositifs ont démontré un angle de déflection de 3,1°, 5 dB de pertes d'insertion et –40 dB de crosstalk.

Deux commutateurs optiques utilisant des déflecteurs rectangulaires ont été

assemblés et ont été démontrés. Combinant les déflecteurs EO avec des collimateurs à fibre et un assemblage haute tension, des commutateurs optiques à haute vitesse ont été construits et caractérisés. La conception du commutateur était basée sur un cristal $LiTaO_3$ de 500 microns d'épaisseur, taillé selon son axe z, et soumis à la méthode d'inversion de domaines. Le commutateur 1x2 a produit un angle de déflection de 1,22° quand soumis à une tension de 1,1 kV et le commutateur 1x4 un angle de 2,14° quand soumis à une tension de 1 kV. La perte d'insertion moyenne et le crosstalk étaient respectivement de 2,36 dB et –36 dB. Le temps de commutation était au maximum de 86 ns.

Chapter 1: Introduction

1.1 Motivation for All-photonic Networks

Computer networks and telecommunication networks play an essential role at work and at home. People communicate in real-time with others, sometimes on different continents, through telephones or cell phones. Emails and messengers provide rapid transmission of written messages across great distances. The Internet has had a major impact on communication, commerce, education and entertainment. In short, our living environment in the twenty first century is deeply dependent on networks.

Modern networks have a history of more than 100 years. After the first manually connected telephone system was established in the mid-1880s, the telecommunications technology evolved from analog switching to digital switching, as it exists in the Public Switched Telephone Network (PSTN). Today, telephony includes not only fixed-line transmission (the residential home phone), but also wireless systems. In the early 1990s, the first analog cellular system—Advanced Mobile Phone System (AMPS)—was supplemented by digital systems: Code Division Multiple Access (CDMA), or Time Division Multiple Access (TDMA) or Global System for Mobile Communications (GSM), which used wireless bandwidth more efficiently. The wireless systems are still evolving to provide new services in what is called third generation wireless technologies. At the same time, computer networks have expanded to all corners of the world, connecting an ever-increasing number of computers.

The explosive growth of multimedia interaction, which carries video, voice, and other data in massive quantities, has tremendously increased the demand for bandwidth. The total number of Internet users has also risen significantly over the years. For example, at the end of March 2006, there were more than 1 billion Internet users worldwide [1].

In the last few years, the bandwidth of networks has undergone major increases due to the rapid progress of optical fiber transmission technologies. Optical networks are based on an optical layer (fiber) and provide high-speed communication services around the world. Untill now, optical fibers and optical components have been widely used in long-distance transport networks such as undersea transmission. But these networks are still built on electronic cross connects and add/drop multiplexing switching systems. They feature frequent optical/electrical signal conversions, which are well-known bottlenecks. The prospect of an all-photonic network to eliminate signal conversions is a widely recognized and sought after objective within the global telecommunications industry. The Agile All Photonics Network (AAPN) is a good example of an all-photonic network.

1.2 Optical Networks—AAPN

AAPN was launched in 2003 as a research network in Canada. This project was funded by the Government of Canada's Natural Sciences and Engineering Research Council (NSERC) and by Canadian companies including Telus, Nortel, and JDS Uniphase. The main purpose of creating this kind of network was to develop an all-photonic network core that could potentially stretch very close to the end-user to reduce optical/electrical signal conversions [2]. Agility, which is the key to the future network, is defined as:

- "the ability to perform time domain multiplexing, to dynamically allocate bandwidth to traffic flows as the demand varies;
- control and routing functionality concentrated at the edge switches that surround the photonic core, and;
- rapidly reconfigurable all-photonic space-switching in the core."[2].

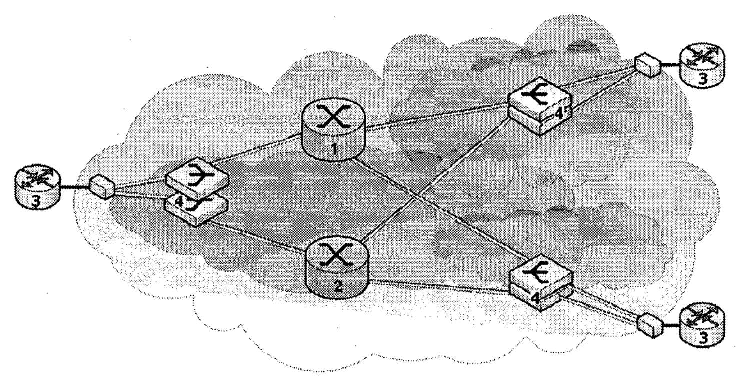

Fig. 1.2.1 Topology of the AAPN network: 1 and 2 are core photonics switches; 3 represents edge nodes; 4 represents wavelength multiplexers and demultiplexers.

As shown in Fig. 1.2.1, AAPN chooses a composite star network topology due to device costs, capacity models, and traffic demand [3]. The signal within the transport network remains in the optical domain, which eliminates the optical-to-electrical (O/E) and electrical-to-optical (E/O) signal conversions. To reach the millisecond reconfiguration times and space-switching requirements, synchronous optical time division multiplexing (OTDM) techniques are introduced. Dense Wave Division Multiplexing (DWDM) technology is used in the AAPN combined with a photonics core switch applied to each wavelength as shown in Fig.1.2.2 [3]. Optical packets, or blocks of data, are in the form of time slots of 10 microsecond's duration, which is a challenge to the photonics core switch considering the short switching times required.

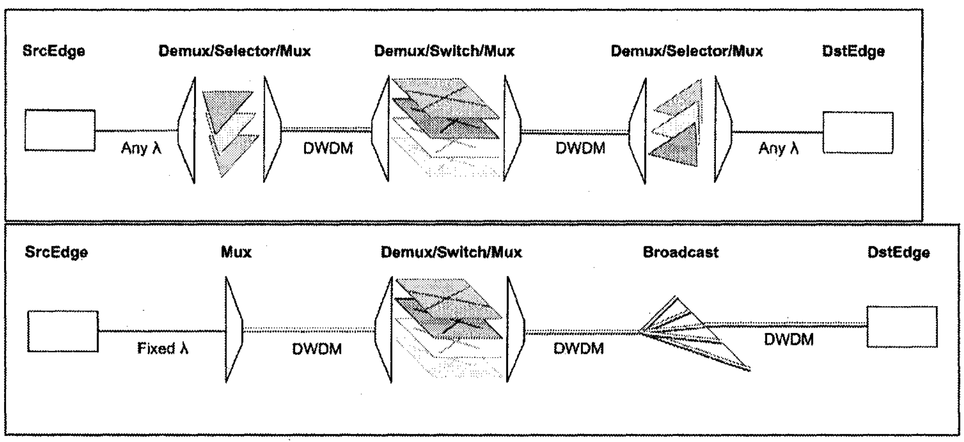

Fig. 1.2.2 DWDM multiplexing technology in AAPN with selective wavelength (up) or fixed wavelength (down) structures; different colors indicate different wavelengths [3].

In AAPN, the edge nodes provide the interface to networks of various kinds, such as Ethernet, SONET, and ATM as shown in Fig. 1.2.3. The broadband O/E or E/O signal converters and wavelength allocations are also established at the edge node.

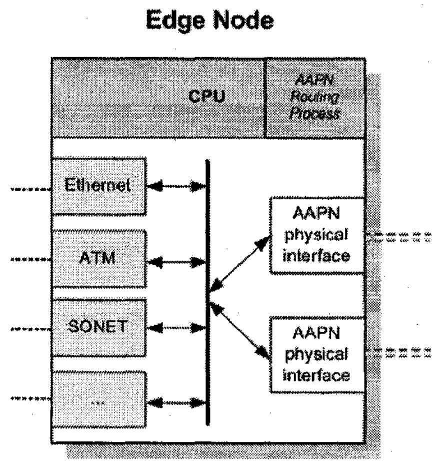

Fig. 1.2.3 Edge node of the network [3]

Although the optical signal remains in the optical domain in the photonic switch in the AAPN network, the switching mechanism involves non-optical techniques such as the electro-optic effect. Fig. 1.2.4 [4] shows the control of the photonic core switch.

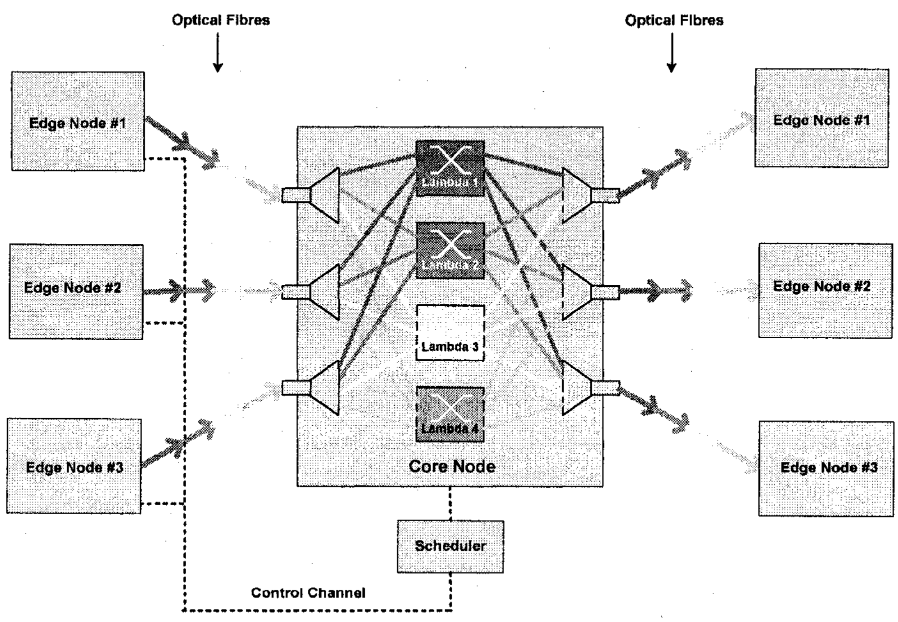

Fig. 1.2.4 Control of the photonic core switch in the electrical domain [4]

1.3 Optical Switching Mechanisms

The switching mechanism of a photonic switch uses various technologies, such as Microelectromechanical Systems (MEMs), waveguide switches, bubble switches, acoustic switches, and so on. Table 1.3.1 [16] lists the strengths, the limitations, and the materials used in some of the switching technologies, and Table 1.3.2 compares their performances. Other performance comparisons of the current technologies for optical switches are provided: switching speed (Fig. 1.3.1 [16]), insertion loss (Fig. 1.3.2 [16]). A time line shows when the various technologies were introduced (Fig. 1.3.3 [16]).

Table 1.3.1. The introduction of the different technologies of optical switches

MEMS [14] (Material: silicon; silica on silicon)	Uses small mirrors to redirect light in 2D/3D or to move an optical waveguide mechanically. Strength: Large port counts can be achieved. Limitations: Slow switching speeds due to mechanical motion.
Bubble [5] (Material: silica on silicon)	Uses total internal reflection off a thermally or voltage generated "bubble" of a different index. Strength: High reliability. Limitations: Slow switching speeds. Total insertion loss is high for large port counts.
Electro-optical (Material: Bulk $LiNbO_3$)	Uses the electro-optic effect to refract or reflect the beam. Strength: Fast switching speed. Limitations: High voltages required to achieve the electro-optic effect.
Electro-optical (EO) [15] (Material: waveguide-$LiNbO_3$)	Uses voltage to change index of Y-splitter or to control interference in MZI/MMI (interferometric switch). Strength: Fast switching speed. Limitations: Large port count is difficult to achieve.
Thermal-optical [13]	Uses a heater to change index of Y-splitter or to control interference in

(Material: polymer, silica or silica on silicon)	MZI (interferometric switch). Strength: Suid well for integration. Limitations: Heating and cooling is inherently a slow process. Good performance is difficult to achieve for large port counts.
Acousto-optical [6] (Material: $LiNbO_3$ or fiber)	Uses sound waves to deflect light traveling through crystals or through fused fiber couplers. Strength: Fast switching speed. Limitations: Higher switch speed and high extinction ratio are mutually exclusive in the fiber case.
Liquid-crystal [9] (Material: Liquid crystals combined with PBS)	Rotates the polarization state of linearly polarized input light to redirect the beam. Strength: High reliability. Limitations: Motion of liquid crystals is slow and very temperature sensitive.
Holographic [10] (Material: liquid crystals or $LiNbO_3$, KLTN)	Electrically or optically controlled index changes in a material cause diffraction of beam to appropriate output. Strength: Large port counts are feasible. Limitations: Poor diffraction efficiency leads to high insertion loss.
Optical phased arrays [8] (Material: waveguides, bulk, liquid crystals)	1-D array with varying optical path lengths. Resultant diffraction redirects the beam. Strength: Large port counts can be achieved. Limitations: Diffraction efficiency poor due to "gaps" in the index variation because of finite, distinct controlling electrodes.
Magneto-optic [11] (Material: orthoferrites and PBS)	Based on Faraday Effect, using an orthoferrite crystal to rotate the polarization state of linearly polarized input (similar to liquid crystal switches). Strength: Large port counts can be achieved. Limitations: Not clear, though very few are researching this technique.

SOAs [12] (Material: semiconductor optical amplifier)	Semiconductor Optical Amplifiers (SOAs) can block or amplify the signal. Strength: Good insertion loss and crosstalk. Limitations: Noise introduced by SOAs. Large ports are hard to achieve.
Mechanical [7] (Material: polymer or silicon)	Uses small optical components (prisms and so on) to redirect light. Strength: Large port counts can be achieved. Limitations: Slow switching speeds due to the mechanical motion.

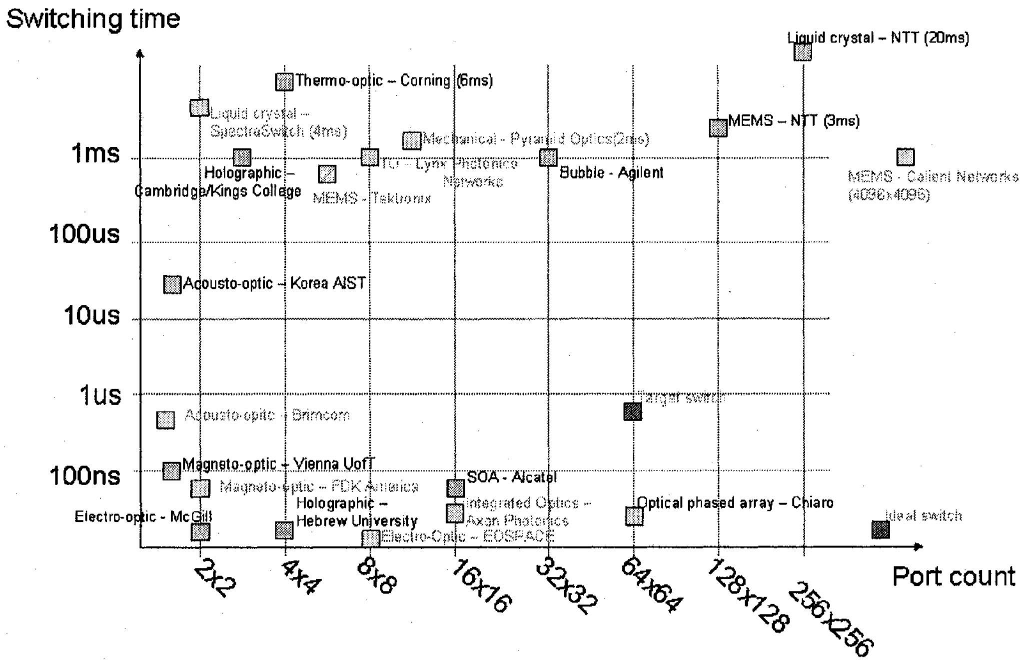

Fig. 1.3.1 Switching time vs. port number for different switching technologies

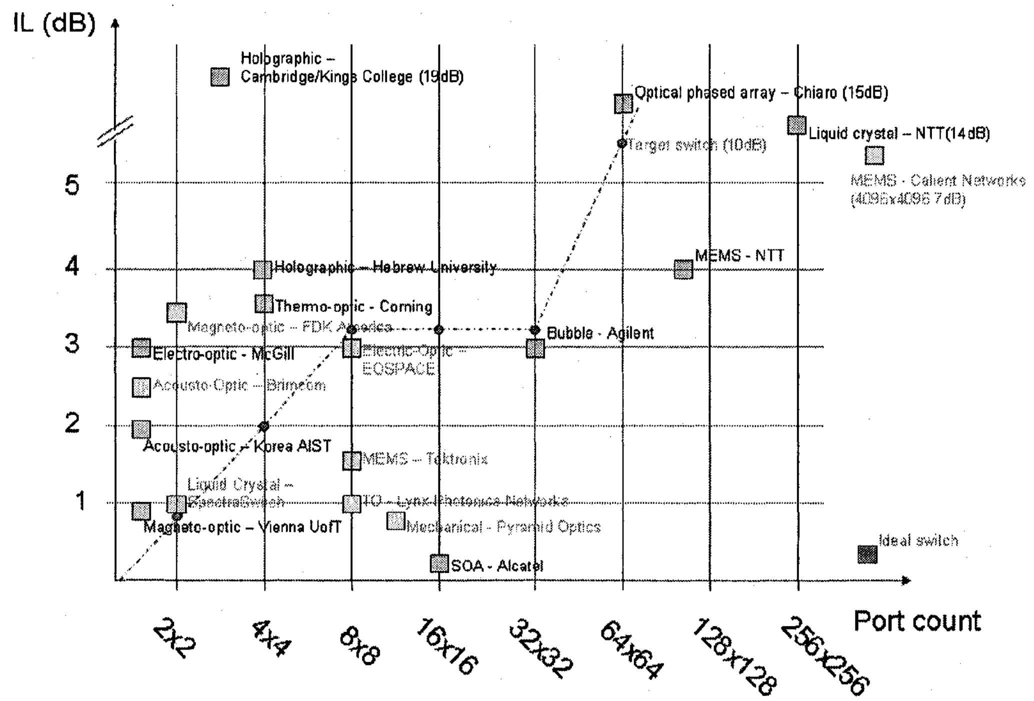

Fig. 1.3.2 Insertion loss vs. port number for different switching technologies

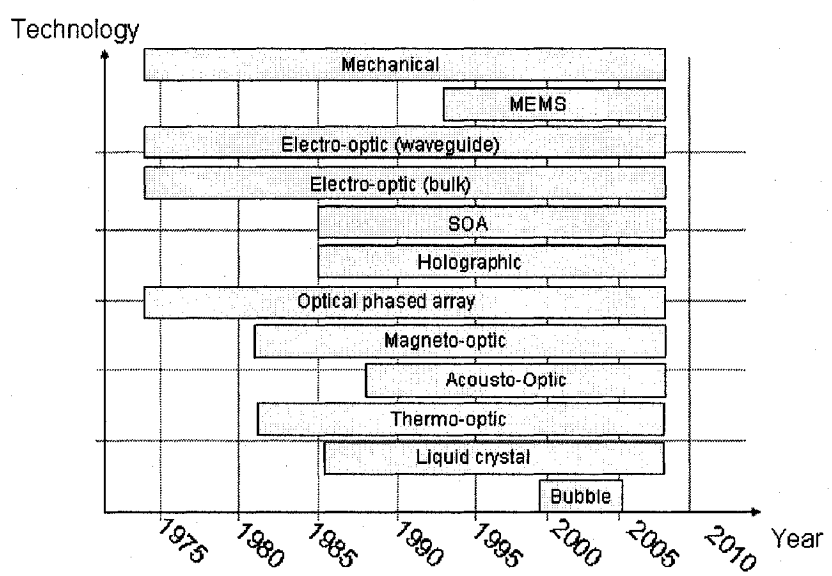

Fig. 1.3.3 Time line for different switching technologies

Table 1.3.2 Comparison of the performances of optical switches

	MEMS	Electro-optic	SOA	Acousto-optic	Liquid crystal	Thermal	Bubble	Holographic	Optical phased array	Mechanical
Port count	**Very High** 1000x1000	**Low** 8x8	**Average** 16x16	**High** 1x300	**Low** 1x16	**Low** 8x8	**Average** 32x32	**High** 4x1024	**Average** 64x64	**Average** 64x64
Switch time	**Slow** ms	**Fast** ns	**Fast**	**Fast** us	**Slow** ms	**Slow** ms	**Slow** ms	**Fast** ms	**Fast** ns	**Slow** ms
Insertion loss	**Average** 0.3-5dB	**Average** 1-5dB	**Low** 0-5dB	**Average** 2-5dB	**very low** <1dB	**Low** 1-3dB	**Low** 2.9dB	**High** 16-20dB	**High** 8 dB	**Low** 0.7-3dB
Crosstalk	**Excellent** 50-70dB	**Good** 20-30dB	**Good** 26-60dB	**Good** 25-30dB	**Good** 26-30dB	**Good** 20-40dB	**Excellent** 70dB	**Bad** 16-36dB	**Bad** 18-25dB	**Excellent** 50-80dB
Physical size	some are small and some large	**Medium** long slim around 2cm*1cm^2	**Small**	**Large** greater than 3cm^3	**Medium**	**Medium** around 1.5cm^3	?	**Small** 10cm^3	**Small** less than or around 1 cm^3	**Small** less than 1 cm^3
Power consumption	**Medium**	**Medium**	**Medium**	**High**	**Medium**	**very low**	?	**High**	**Medium**	**Medium**
PDL (NA; High, Low)	**NA**	**High**	**High/ NA**	**High**	**High**	**High/ NA**	**Medium**	**High**	**High**	**NA**
# of stages	**Low**	**High**	**High**	**Low**	**High**	**High**	**Medium**	**Low**	**Low**	**High**
Wavelength dependence	**NA**	**NA/High**	**High**	**High**	**High**	**Medium**	**Low**	**High**	**High**	**NA**

As shown in the above figures and tables, EO switches, especially those based on bulk material, become a good choice considering the AAPN requirements. They can provide rapid switching speed to perform OTDM at the frame or packet level, are easy to manufacture and can be economically assembled. They are now the most commonly used technology in the EO device market.

1.4 Thesis Work

1.4.1 Research Focus

My research work consisted in finding the optimum design for the bulk EO switches of the AAPN. It focused on the following areas:

- Better designs for EO deflectors, which built on non-rectangular geometries on bulk EO materials.
- The design, fabrication, and packaging of multi-port EO switches based on these EO deflectors.

1.4.2 Organization of the Dissertation

Chapter 2 introduces the EO theory and the EO deflectors. The current equivalence theory is extended in Section 2.3 and serves as the theoretical foundation for the design and the analysis of new nonrectangular EO deflectors. The limitations on the deflection angle of rectangular shaped devices are analyzed in Section 2.4. After a brief literature review in Section 2.5, Section 2.6 proposes the deflection performance indicator as a merit to compare all the devices.

Chapter 3 reviews the fabrication process of the EO devices. Masks are first sketched according to the different designs. The processes of photolithograph, metallization, evaporation, and liftoff are introduced in Section 3.2, and section 3.3 describes the domain inversion using the electric field poling.

Chapter 4 proposes two new EO deflectors that are based on the optimal design discussed in chapter 2. A new parabolic geometry and another new nonrectangular deflector with half-horn geometry are derived, which exhibit the best-known steering performance among all EO devices. Simulations using several software packages, such as Code V, Beam Propagation Method (BPM), and Matlab have been conducted to verify the equivalent theory and to examine the deflection functionality. A comparison of the simulated performance of these devices is also given. Based on the new geometries, two novel EO deflectors are proposed. Section 4.4 describes the design and the simulation of the deflectors. The concepts of the design of the non-blocking 2x2 EO switches built on these deflectors are also presented. Experimental results of the new geometries and the new deflectors are given in Section 4.5.

Chapter 5 demonstrates the packaged 1x2 and 1x4 EO switches. The optical system design and the simulations of the switches are given in section 5.2. Section 5.3 presents the results of the free space test, the package design, and the test of the packaged devices. In section 5.4, the high-speed test and damping test are presented.

Chapter 6 reviews the research work presented in previous chapters. Some of the problems that occurred during the design, fabrication, and experiment are discussed. Future work on the EO deflectors and EO switches is also outlined.

1.4.3 Original Contributions

EO devices have been studied for more than 25 years. Based on the previous work of other researchers regarding EO materials, prism type devices, and EO switches, I extended the current equivalent theory of EO deflectors. The optimal design of the EO deflectors to achieve the largest steering angle is proposed. Also, several packaged EO switches have been designed, fabricated, packaged, and tested. The key contributions in my research are as follows:

- Proved that the iterated-prism structure is equivalent to the index gradient structure when they both share the same external shape.

- Proved that a parabola deflector provides the best steering performance, among all EO deflectors.
- Proposed an additional type of beam deflector shape (half-horn) used to obtain better deflection angles.
- Demonstrated packaged ultra-fast 1x2 and 1x4 optical switches with switching times of 80 ns, 2-4 dB insertion loss, and -30dB crosstalk.
- Demonstrated 2x2 optical deflectors based on the parabola and half-horn shaped deflectors.
- Proposed the design concept of 2x2 optical switch based on the EO deflectors.

This research has led to the following publications from the Photonics Systems Group of McGill University:

Journals:

[1]. Y. Zuo, M. Mony, B. Bahamin, V. Aimez, and D.V. Plant, "Bulk Electro-Optic Deflector Based Switches," *Applied Optics*, Accepted, Dec., 2006.

[2]. Y. Zuo, M. Mony, V. Aimez, and D.V. Plant, "Half-horn and Parabolic EO Deflector-based Switches," *Photonics Technology Letters*, Submitted, Dec., 2006.

[3]. Y. Zuo, B. Bahamin, E. J. Tremblay, C. Pulikkaseril, E. Shoukry, M. Mony, P. Langlois, V. Aimez, and D.V. Plant, "1x2 and 1x4 Electro-optic Switches," *Photonics Technology Letters*, Vol.17, No.10, 2080-2082, 2005.

Conferences:

[1]. Y. Zuo, M. Mony, V. Aimez, and D. V. Plant, "New Geometrical Shaped EO Deflectors," *Conference on LEOS, the 19th Annual Meeting of the IEEE*, Montreal, Quebec, Canada, October 29th-November 2nd, 2006.

[2]. Y. Zuo, B. Bahamin, P. Langlois, V. Aimez, and D.V. Plant, "Half-Horn

and Parabola Shaped Electro-Optic Beam Deflectors," *AO/COSI/IP/SRS*, Charlotte, North Carolina, June 6-9, 2005.

[3]. Y. Zuo, B. Bahamin, P. Langlois, V. Aimez, and D. V. Plant, "Packaging and Performance of an Ultra-Fast 1x4 Optical Switch," Vol. 2, pp. 1031-3, *Conference on Lasers and Electro-Optics (CLEO)*, IEEE, Baltimore, MD, USA, May 22-27, 2005.

[4]. E.J. Tremblay, C. Pulikkaseril, E. Shoukry, B. Bahamin, Y. Zuo, M. Mony, P. Langlois, V. Aimez, and D.V. Plant, "A 1x2 fast fiber-optic switch based on electro-optic beam scanning," Vol. 1, pp. 2, *Conference on Lasers and Electro-Optics (CLEO)*, May 16-21, 2004, IEEE, San Francisco, CA, USA.

[5]. E.J. Tremblay, C. Pulikkaseril, Y. Zuo, and D.V. Plant, "Ferroelectric domain inversion in $LiTaO_3$ using an external pulsed poling field," *Conference on Photonics North*, 182-006, May 25-29, 2003, SPIE, Montreal, QC, Canada.

[6]. C. Pulikkaseril, E. J. Tremblay, Y. Zuo, and D.V. Plant, "Free-space switching using multiple electrooptic interfaces," *Conference on Photonics North*, 182-671, May 25-29, 2003, SPIE, Montreal, QC, Canada.

1.5 References

[1] http://www.internetworldstats.com/top20.htm

[2] http://www.aapn.mcgill.ca/eng/index.html

[3] L. Mason, A. Vinokurov, N. Zhao, and D.V. Plant, "Topological design and dimensioning of Agile All-Photonic Networks (AAPNs)," *Elsevier Computer Networks Journal*, Vol. 50, pp. 268-287, 2006.

[4] J. Zheng, C. Peng, and G.V. Bochmann, "An Effective Fault Detection and Localization Scheme for All-Optical Overlaid-Star TDM Networks," submitted to *JON.*

[5] S. Venkatesh, J.E. Fouquet, R. Haven, M. DePue, D. Seekola, H. Okano, and H. Uetsuka, "Performance improvements in bubble-actuated photonic cross-connect switches," *Conference Lasers and Electro-Optics Society (LEOS)*, Vol. 1, pp. 39-40, 2002.

[6] H.S. Park, K.Y. Song, S.H. Yun, and B.Y. Kim, "All-fiber wavelength-tunable acoustooptic switches based on intermodal coupling in fibers," *Journal of Lightwave Technology*, Vol. 20, pp. 1864-1868, 2002.

[7] M. Hoffmann, D. Nusse, and E. Voges, "An electrostatically actuated 1/spl times/2 moving-fiber switch," *Photonics Technology Letters, IEEE*, Vol. 15, pp. 39-41, 2003.

[8] JA. Thomas and Y. Fainman, "Optimal Cascade Operation of Optical Phased-Array Beam Deflectors," *Applied Optics,* Vol. 37, pp. 6196-6212, 1998.

[9] S. Toshikazu, K. Kazuo, N. Kazuhiro, and N. Noboru, "256 x 256 turnover-type free-space multichannel optical switch based on polarization control using liquid-crystal spatial light modulators," *Applied Optics*, vol. 34, pp. 2581-2589,

1995.

[10] J. Qi, H. Xianyu, J. Liang, and G.P. Crawford, "Active U-turn electrooptic switch formed in patterned holographic polymer-dispersed liquid crystals," *Photonics Technology Letters, IEEE,* Vol. 15, pp. 685 – 687, 2003.

[11] Y.S. Didosyan, H. Hauser, and G.A. Reider, "Magnetooptic switch based on domain wall motion in orthoferrites," *IEEE Transactions on Magnetics*, Vol. 38, pp. 3243–3245, 2002.

[12] C.M. Gallep and E. Conforti, "Reduction of Semiconductor Optical Amplifier Switching Times by Preimpulse Step-Injected Current Technique," *Photonics Technology Letters, IEEE,* vol. 14, pp. 902--904, 2002.

[13] HC. Tapalian, JP. Laine, and PA. Lane, "Thermooptical switches using coated microsphere resonators," *Photonics Technology Letters, IEEE,* Vol. 14, pp. 1118-1120, 2002.

[14] J. Kim, C.J. Nuzman, B. Kumar, D.F. Lieuwen, J.S. Kraus, A. Weiss, C.P. Lichtenwalner, A.R. Papazian, R.E. Frahm, N.R. Basavanhally, D.A. Ramsey, V.A. Aksyuk, F. Pardo, M. E. Simon, V. Lifton, H.B. Chan, M. Haueis, A. Gasparyan, H.R, Shea, S. Arney, C.A. Bolle, P.R. Kolodner, R. Ryf, D.T. Neilson, and J.V. Gates, "1100x1100 Port MEMS-Based Optical Crossconnect with 4-dB Maximum Loss," *Photonics Technology Letters, IEEE,* Vol.15, pp. 1537, 2003.

[15] M.P. Earnshaw, and D.W.E. Allsopp, "Semiconductor space switches based on multimode interference couplers," *Journal of Lightwave Technology*, vol. 20, pp. 643-650, 2002.

[16] M. Mony and Y. Zuo, "Survey of Optical Switching Technologies," internal report for AAPN Theme 2 meeting (2003).

Chapter 2: EO Effect and EO Deflectors

2.1 Introduction

The Electro-Optic (EO) effect or Pockel's effect is a phenomenon by which "the index of refraction of certain types of crystals is changed with the application of an electric field." [1] Devices obtained in this way, and whose operation relies on this principle, are referred to as "EO devices." The response time of EO devices is extremely short because the EO effect relies on minute displacements in the atomic crystal structure [1].

EO devices have various applications including sensors, scanners, deflectors, and switches [2]. In this chapter, attention is paid to EO deflectors, which can steer an optical beam. Electro-optic beam deflectors can be used in optical displays, photographic recording, switching/routing, printing, data storage, space tracking and acquisition, as well as laser control. These devices exhibit high bandwidth, fast response time, moderate deflection, low power consumption, and are generally very compact when compared to other deflectors. Given these benefits, EO beam deflectors are currently widely used for applications in optical switching. For example, high-speed, low-loss optical switches for future optical networks can be built using EO deflectors [3]-[5]. These novel EO switches are distinguished by a much-improved steering performance, high-speed response, and simple fabrication requirements.

The EO effect is briefly presented in Section 2.2 and two methods of analysis and design, prism analysis and index analysis, are described in Section 2.3. Section 2.4 introduces the limitation of the rectangular shaped devices and a literature review of existing EO devices is then summarized in Section 2.5. Conclusions and references are given in Section 2.6 and 2.7.

2.2 EO Effect and EO Deflectors

2.2.1 EO Effect

In general, the EO effect is a phenomenon where the refractive index is modified when a steady electric field is applied to a crystal. More specifically, the nine elements η_{ij} of tensor η are changed according to the external E-field *E(Ex, Ey, Ez)*, and thus, the index ellipsoid is also changed. If only the linear effect is considered, the γ_{ijk} (Pockel's coefficient) works as:

$$\eta_{ij}(E) = \eta_{ij0} + \sum_k \gamma_{ijk} E_k \tag{1}$$

So, the index change would be:

$$\begin{vmatrix} \Delta(\frac{1}{n^2})_1 \\ \Delta(\frac{1}{n^2})_2 \\ \Delta(\frac{1}{n^2})_3 \\ \Delta(\frac{1}{n^2})_4 \\ \Delta(\frac{1}{n^2})_5 \\ \Delta(\frac{1}{n^2})_6 \end{vmatrix} = \begin{vmatrix} \gamma_{11} & \gamma_{12} & \gamma_{13} \\ \gamma_{21} & \gamma_{22} & \gamma_{23} \\ \gamma_{31} & \gamma_{32} & \gamma_{33} \\ \gamma_{41} & \gamma_{42} & \gamma_{43} \\ \gamma_{51} & \gamma_{52} & \gamma_{53} \\ \gamma_{61} & \gamma_{62} & \gamma_{63} \end{vmatrix} \begin{vmatrix} E_x \\ E_y \\ E_z \end{vmatrix} \tag{2}$$

where 1, 2, 3, etc. is the symbol in the index ellipsoid as follows:

$$\left(\frac{1}{n^2}\right)_1 x^2 + \left(\frac{1}{n^2}\right)_2 y^2 + \left(\frac{1}{n^2}\right)_3 z^2 + 2\left(\frac{1}{n^2}\right)_4 yz + 2\left(\frac{1}{n^2}\right)_5 xz + 2\left(\frac{1}{n^2}\right)_6 xy = 1 \tag{3}$$

So, in trigonal 3m crystals such as $LiTaO_3$ or $LiNbO_3$, the coefficient tensor is now:

$$\begin{vmatrix} 0 & \gamma_{12} & \gamma_{13} \\ 0 & -\gamma_{12} & \gamma_{13} \\ 0 & 0 & \gamma_{33} \\ 0 & \gamma_{42} & 0 \\ \gamma_{42} & 0 & 0 \\ \gamma_{12} & 0 & 0 \end{vmatrix} \tag{4}$$

The refractive index of uniaxial crystals has the following properties:

$n_x = n_y$ and $n_z = n_e$.

When applying an E-field of $E = (0, 0, E_z)$,

$$\frac{1}{\Delta n_x^2} = \gamma_{13} E_z \qquad \frac{1}{\Delta n_e^2} = \gamma_{33} E_z \tag{5}$$

$$\Delta n_x \approx -\frac{1}{2} n_x^3 \gamma_{13} E_z \qquad \Delta n_e \approx -\frac{1}{2} n_e^3 \gamma_{33} E_z \tag{6}$$

where the $\gamma_{33} \approx 3\gamma_{13}$ and $\Delta n_e > \Delta n_x$

In this case, the E-field has the same direction as the z-axis (optical axis). When the E-field is opposite to the optical axis, a positive index change can be achieved.

Larger Δn_e should be realized to achieve better optical performance. Thus, a linear light source in the TM mode (the E-field is parallel to the z direction) is utilized as the incident light.

2.2.2 EO Response Time

The potential large bandwidth or high-speed property of light waves, which is critical in the applications such as communication, medicine, aerospace, and so on, is one of the most important attributes of EO devices. The EO effect relies on minute displacements in the atomic crystal structure, which is ultra-fast. In chapter 5, the response time of the packaged EO switches will be tested and analyzed. We will also show how lumped electrodes are deposited to establish an E-field on the EO deflectors.

To achieve even larger bandwidth such as 40GHz or higher, the normal lumped electrodes cannot satisfy the requirement anymore because of their physical constraints. The lumped electrodes act as a capacitor storing charges when a voltage is applied, and the bandwidth of the EO device is limited by the product of capacitance and load resistance. The calculation of the capacities of the electrodes is given in chapter 5. To minimize the problem, RF transmission lines with traveling-wave electrodes can be introduced. Applications with 40GHz or higher bandwidth have been produced in EO guided-wave modulators [6], [7]. Although all the devices in my work still use the lumped electrodes, future research can experiment with traveling-wave electrodes to achieve wider bandwidth.

2.2.3 Domain Inversion

Although most EO crystals can be utilized in EO devices, they normally are composed of one single domain with one spontaneous polarization direction and only the index under the external E-field will change. To achieve larger EO effect, domain inversion is introduced and is carried out to invert the initial spontaneous polarization of the material. By creating two domains with opposite polarization directions in the contiguous crystal, a positive index change $+\Delta n_e$ and a negative index change $-\Delta n_e$ can be established in the two domains respectively when applying an external field on the special crystal. With the index changes in both domains, EO effect is doubled and the deflection angle in these devices is doubled too.

The special EO crystals which are capable of inverting the spontaneous polarization direction are called ferroelectric crystals. The process of the domain inversion is called poling. The material properties and the domain inversion will be introduced in detail in Chapter 3.

Assuming that the domain with spontaneous polarization direction has index change of $-\Delta n_e$ when a voltage is applied, the other domain with inverted polarization direction will have index change $+\Delta n_e$. One can design patterns for the areas of a crystal where the domain will be inverted, to provide the desired optical effect in the EO device.

2.3 EO Deflectors

When an electric field is applied across the two domains in the crystal, the trajectory of the beam is diverted as it travels through the wafer. The electric field induces an index change of opposite magnitude in the adjacent domain regions of the EO device, causing the optical beam to refract at the interfaces. Thus, light beam deflection is obtained.

EO deflectors are usually built using a pattern with a series of prisms. The prism areas are first poled to invert the polarization direction, during the manufacture of the EO device, and an external voltage is applied across the whole crystal to achieve beam deflection in the operation of the device. The two regions with prism shapes have different refraction indices as shown in Fig. 2.3.1. By defining the vertex of each prism, the travel path of light beam can be determined.

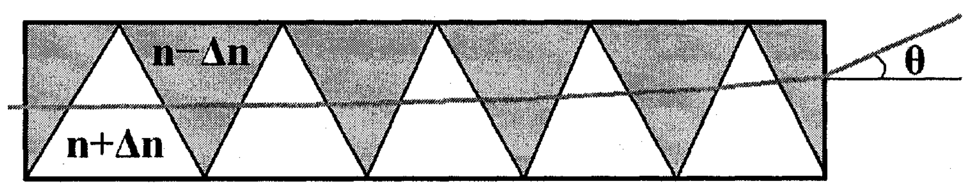

Fig. 2.3.1 Two domains in a rectangular shaped 1x2 EO device

The relationship between the change in index of refraction at the interfaces and the applied electric field is given by the equation:

$$\Delta n = n_0^3 r_{33} \frac{V}{D} \tag{7}$$

In this case, n_0 is the original index; r_{33} is the corresponding electro-optic coefficient of the substrate along the z-axis, V is the applied electric field along the direction of the dielectric polarization, and D is the thickness of the substrate.

Since the Δn_e is much larger than Δn_x, from now on, a prism with index

$n-\Delta n_e$ in a uniform media of index $n+\Delta n_e$ is the focus of study.

2.3.1 Ray Tracing in Prisms

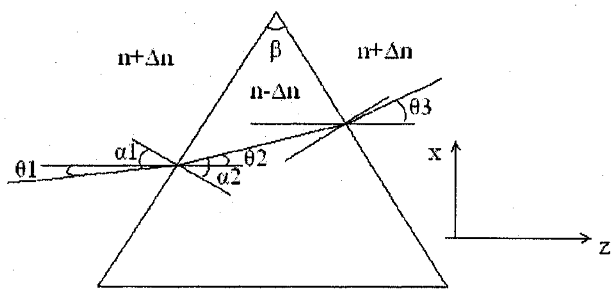

Fig. 2.3.2 Prism induced beam refraction

Since the pattern is obtained using a series of prisms (as the one shown in Fig.2.3.2), the analysis begins by examining the behavior of the beam as it crosses each prism. Given that the outer index is greater than the index inside the prism, the light beam bends up. Since each prism presents two boundaries, they each provide two consecutive deflections. The beam passes from a region of index $n_1 = n + \Delta n$ into a second region of index $n_2 = n - \Delta n$ and vice versa.

$$n_1 \sin(\frac{\beta}{2} + \theta_1) = n_2 \sin(\frac{\beta}{2} + \theta_2) \tag{8}$$

$$n_2 \sin(\frac{\beta}{2} - \theta_2) = n_1 \sin(\frac{\beta}{2} - \theta_3) \tag{9}$$

Given that the actual index difference between the two regions is in the order of 10^{-3}, and the incident and output angles are very small, the simplification will be:

$$\frac{\sin(\frac{\beta}{2} + \theta_1)}{\sin(\frac{\beta}{2} + \theta_2)} = \frac{n_2}{n_1} = \frac{\sin(\frac{\beta}{2} - \theta_3)}{\sin(\frac{\beta}{2} - \theta_2)} = \frac{\sin(\frac{\beta}{2} + \theta_1) + \sin(\frac{\beta}{2} - \theta_3)}{\sin(\frac{\beta}{2} + \theta_2) + \sin(\frac{\beta}{2} - \theta_2)} \tag{10}$$

$$\frac{n_2}{n_1} \approx 1 - \frac{2\Delta n}{n} = 1 - \frac{\Delta\theta}{2}\cot(\frac{\beta}{2}) \tag{11}$$

Assuming that the incident and output angles are very small, (10) becomes:

$$(10) \approx \frac{\sin(\frac{\beta}{2}) + \theta_1\cos(\frac{\beta}{2}) + \sin(\frac{\beta}{2}) - \theta_3\cos(\frac{\beta}{2})}{\sin(\frac{\beta}{2}) + \theta_2\cos(\frac{\beta}{2}) + \sin(\frac{\beta}{2}) - \theta_2\cos(\frac{\beta}{2})} = 1 - \frac{\Delta\theta}{2}\cot(\frac{\beta}{2}) \tag{12}$$

where, $\Delta\theta = \theta_3 - \theta_1$

The prism deflection angle is governed by the formula:

$$\Delta\theta = \frac{4\Delta n}{n}\tan(\frac{\beta}{2}) \tag{13}$$

For the whole prisms series, the total deflection angle is expressed as:

$$\Delta\theta = \sum_k \frac{4\Delta n}{n}\tan(\frac{\beta}{2}) = \frac{4\Delta n}{n}\sum_k \frac{L_k/2}{W_k} \tag{14}$$

Where L_k is the length of the kth prism, W_k is the width of the kth prism.

In rectangular shaped devices, since W_k (width of the kth prism) are all the same in each prism, (14) can be simplified to:

$$\Delta\theta = \frac{4\Delta n}{n}\sum_k \frac{L_k/2}{W_k} = \frac{2\Delta n}{n}\frac{L}{W} \tag{15}$$

where, L is the total length, and W is the uniform width of the device.

From (15), the total deflection angle in rectangular shaped devices depends only on the device's length and width. The number of prisms is no longer important if there are more than 10 prisms, as per [8].

2.3.2 Ray Equation in Gradient Index Materials

Another common structure of the EO deflectors is based on the gradient index material as Fig. 2.3.3 shows. In Chapter 4, the equivalence of this structure and the prism structure under some requirement will be proved.

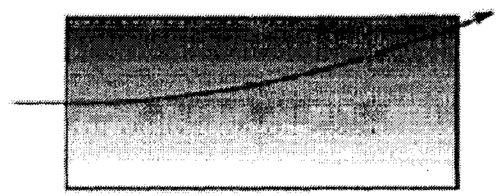

Fig. 2.3.3 Material with gradient index

In that material, a light ray obeys the following [9]:

$$\frac{d^2X}{dz^2}=\frac{d\theta}{dz}=\frac{\nabla n}{n_0}=\frac{1}{n_0}\frac{\partial n}{\partial X}=\frac{2\Delta n}{n_0}\frac{1}{W(z)} \tag{16}$$

Where *W(z)* is the total width of the device at z coordinate.

From which the following relationship for the deflection angle is obtained:

$$\Delta\theta=\int\frac{2\Delta n}{n_0}\frac{1}{W(z)}dz \tag{17}$$

2.4 Limitation of Rectangular Deflectors

Rectangular devices are most commonly used in EO deflectors. But since rectangular devices require a larger device width to cover the entire bended light path, their performance is limited. When considering a rectangular deflector as Fig. 2.3.1 shows, the device width is made to be much larger than the spot size of the incident beam, to accommodate the full bipolar deflection of the beam at the exit. Thus, the width is unnecessarily large and the deflection angle θ is limited. In this section, the limitation of the rectangular shaped deflector will be quantified for the first time as described below.

According to the shape and the beam bending, the relationships between the length L, width W, beam waist w, and the deflection angle θ are as follows:

$$W^2 = wW + L^2 \frac{V}{D} n^2 r_{33} \qquad L = \sqrt{\frac{W^2 - wW}{\frac{V}{D} n^2 r_{33}}} \tag{18}$$

This implies that W needs to be larger than w.

To better assess these limitations, the upper and lower bounds of the performance of the rectangular devices should be provided.

In rectangular deflectors, the width of the device needs to be large enough to accommodate the full deflection of the beam.

$$W = waist + \theta L \tag{19}$$

Therefore $\frac{L}{W} < \frac{1}{\theta}$ (20)

Simultaneously, $\theta = \frac{n^2 r_{33} V}{D} \frac{L}{W}$ (21)

$$\text{and therefore } \theta < \sqrt{\frac{n^2 r_{33} V}{D}} \tag{22}$$

The number of prisms in EO devices should be at least 10 [8]. Considering the ratio of device length and width, which usually is large, the deflection and reflection loss in the prism interfaces could be a lot while there are only a few interfaces/prisms. Assume a minimum of 11 prisms is required inside each device, and all prisms are assumed to have an identical apex angle of 60°,

$$\frac{L}{W} > 11 * 2 * \tan(30°) \approx 13 \tag{23}$$

$$\text{therefore } \theta > 13\frac{n^2 r_{33} V}{D} \tag{24}$$

$$\text{and finally } 13\frac{n^2 r_{33} V}{D} < \theta < \sqrt{\frac{n^2 r_{33} V}{D}} \tag{25}$$

In conclusion, the deflection angle of rectangular devices has an upper bound. In the common case of V/D=1/500 kV/μm, and where r_{33} is 30×10^{-12} m/V, θ can never be greater than 17 mrad. Even in a case where V/D=1/150 kV/μm, θ still is smaller than 31 mrad. These results are very important, since they demonstrate that, irrespective of the design, the deflection angle obtained using rectangular devices is always smaller than $\left[n^2 r_{33} V / D\right]^{1/2}$.

2.5 Literature Review

A literature review of existing EO devices and their performance is provided in Table 2.5.1. Until now, the focus of these applications was mainly limited to rectangular shaped devices.

Table 2.5.1 Literature review of existing EO devices

Electro-Optic Beam deflector [10] The demonstrated device was fabricated on a 0.5 mm thick z-cut single-crystal $LiTaO_3$ substrate with the following dimensions: 10 x 0.75 mm^2. A He-Ne laser (633 nm) was employed as the light source. The scanning angle was about 4 mrad at 600 V.	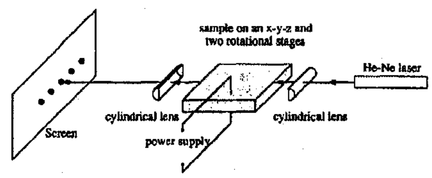
Rectangular Electro-Optic beam deflectors [11] The device is an EO deflector in 1 mm thick KTP. The deflector (L x d = 10 mm x 100 μm) is located at the center. The measured Δn is 1.1×10^{-4} /kV, and the maximum angle is 0.57° using a beam with a 0.6328 μm wavelength.	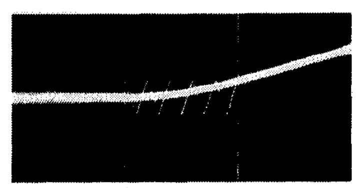
Rectangular EO beam deflectors [8] The experimental $LiTaO_3$ device has a width of 1 mm, an effective length of 8.5 mm, a substrate thickness of 0.5 mm, and exhibits 5.0 mrad/kV deflection sensitivity when working with a He-Ne laser.	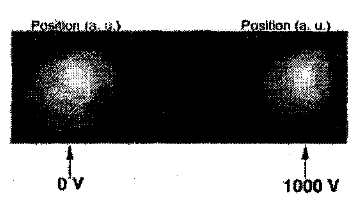

Trapezoidal EO beam scanners [12] The BPM simulation results show that when the index is 1.85, the Δn $1.76\text{x}10^{-3}$ /kV, the middle point width 600 um, the device length 10 mm, and W_0/W_R ranges from 1.0 to 0.15, the scanning sensitivity will be between 1.0 and 2.6.	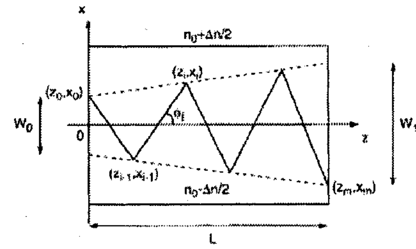
Shape-optimized EO beam scanners [13] Here, a linearly polarized He-Ne laser (633 nm) was used. The entrance width of the horn-shaped scanner is 92 μm, and the exit width is 678 μm. The thickness of the z-cut $LiTaO_3$ substrate was 150 μm. The external deflection of the scanner was measured to be 91 mrad at 1 kV.	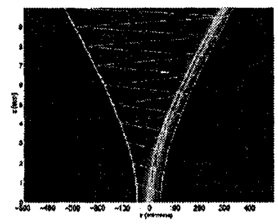

Untill now research mainly focused on rectangular shaped devices. Some researchers [12], [13] started to consider non-rectangular EO deflectors, such as trapezoidal or horn shaped devices. Their efforts are commendable and very useful. But since their research and devices are for EO scanners, which require continuous voltages and positive and negative voltages, the devices are not optimized for EO switches.

In chapter 4, an optimized EO deflector design for the application of EO switches, which only have on and off status, will be proposed for the first time. In that chapter, further analysis reveals that among all possible deflector shapes, the parallel-parabola shaped deflector exhibits the largest deflection angle. In addition, several new nonrectangular geometry designs, which are capable of further enhancing the deflection performance, are proposed and compared.

2.6 Conclusion

The EO effect constitutes the basis of all EO devices. In this chapter, the EO effect is described and equations are given for the refraction index change. Ray tracing and integral tracing are different ways to analyze the performance of the EO deflector. The response time of the EO effect is also discussed.

Rectangular shaped EO devices are often used in all kinds of applications. In this chapter, the original limitation of the rectangular devices is analyzed, simulated, and quantified. The bounds of the deflection angles that the rectangular device can provide are identified for the first time. These results can serve as the guide for the future design of all EO deflectors.

A summary of the literature survey is also given in this chapter. Based on previous research, the optimal EO deflectors and some other new shaped EO deflectors for the application of EO switches will be proposed in Chapter 4.

To better understand EO devices, EO materials and the manufacture of EO devices will be introduced in the next chapter. The EO materials, the procedure to invert domains, the patterns, the deposition of electrodes, and more will be described step by step in chapter 3. With this understanding, new deflectors and packaged EO switches will be proposed in chapters 4 and 5.

2.7 References

[1] B. E. A. Saleh and M. C. Teich, *Fundamentals of Photonics.* New York: Wiley, 1991, ch. 18, pp. 696–736.

[2] I. P. Kaminow, *An Introduction to Electrooptic Devices,* New York:Academic, 1974, ch. 2, pp. 39–70.

[3] E.J. Tremblay, C. Pulikkaseril, E. Shoukry, B. Bahamin, Y. Zuo, M. Mony, P. Langlois, V. Aimez, and D.V. Plant, "A 1x2 fast fiber-optic switch based on electro-optic beam scanning," Vol. 1, pp. 2, *Conference on Lasers and Electro-Optics (CLEO),* May 16-21, 2004, IEEE, San Francisco, CA, USA.

[4] Y. Zuo, B. Bahamin, P. Langlois, V. Aimez, D. V. Plant, "Packaging and Performance of an Ultra-Fast 1x4 Optical Switch," Vol. 2, pp. 1031-3, *Conference on Lasers and Electro-Optics (CLEO)*, May 22-27, 2005, IEEE, Baltimore, MD, USA.

[5] Y. Zuo, B. Bahamin, E. J. Tremblay, C. Pulikkaseril, E. Shoukry, M. Mony, P. Langlois, V. Aimez, and D.V. Plant, "1x2 and 1x4 Electro-optic Switches for Agile All-Photonic Networks," *Photonics Technology Letters*, Vol.17, No.10, 2080-2082, 2005.

[6] T. Sueta and M. Izutsu, "High Speed Guided-Wave Optical Modulators," Journal of Optical Communications, Vol.3, No.2, pp. 52-58, 1982.

[7] E. L. Wooten, K. M. Kissa, A. Yi-Yan, E. J. Murphy, D. A. Lafaw, P. F. Hallemeier, D. Maack, D. V. Attanasio, D. J. Fritz, G. J. McBrien, and D. E. Bossi, "A Review of Lithium Niobate Modulators for Fiber-Optic Communications Systems," IEEE Journal of Selected Topics in Quantum Electronics, Vol. 6, No. 1, pp. 69-82, 2000.

[8] Y. Chiu, R.S.Burton, D.D. Stancil, and I.E.Schlesinger, "Design and Simulation of Waveguide Electrooptic Beam Deflectors," *Journal of Lightwave Technology*, Vol. 13, No. 10, pp. 2049-2052, 1995.

[9] B. E. A. Saleh and M. C. Teich, *Fundamentals of Photonics*. New York: Wiley, 1991, ch. 1, pp. 1–39.

[10] Q. Chen, Y. Chiu, D. N. Lambeth, T. E. Schlesinger, and D. D. Stancil, "Guided-Wave Electro-Optic Beam Deflector Using Domain Reversal in $LiTaO_3$," *Journal of Lightwave Technology*, Vol. 12, No. 8, pp. 1401-1404, 1994.

[11] J. F. Lotspeich, "Electrooptic light-beam deflection," *IEEE Spectrum*, pp. 45–52, 1968.

[12] Y. Chiu, J. Zou, D. D. Stancil, and T.E. Schlesinger, "Shape-Optimized Electrooptic Beam scanners: Analysis, Design, and Simulation," *Journal of Lightwave Technology,* Vol. 17, No. 1, pp. 108-114, 1999.

[13] J. C. Fang, M. J. Kawas, J. Zou, V. Gopalan, T.E. Schlesinger, and D. D. Stancil, "Shape-Optimized Electrooptic Beam scanners: Experiment," *Photonics Technology Letters, IEEE*, Vol. 11, No. 1, pp. 66-68, 1999.

Chapter 3: Fabrication of EO Devices

3.1 Introduction

Chapter 2 introduced the EO effect and prism based EO deflectors. The concatenated prisms are obtained by domain inversions using electric field poling. As Chapter 2 presented, by inverting the spontaneous polarization direction in the concatenated prism area, two domains in a contiguous crystal can be created. When an external voltage is applied to the crystal, positive and negative index changes are achieved in the different domains. In this way, the deflection angle is doubled when compared to unpoled EO crystals.

In this chapter, EO ferroelectric materials are first investigated in Section 3.2. Section 3.3 describes how the optimally designed prism geometries are sketched as electrode patterns in photomasks that in turn are lithographical defined and metallized onto the EO substrates to create poling electrodes. The spontaneous domains of the prism regions are then inverted by electric field poling as Section 3.4 describes. Conclusions and references are given in Section 3.5 and 3.6, respectively.

3.2 EO Materials

3.2.1 Ferroelectric Materials

The permanent electric dipole moment of some crystals may, in certain cases, be reoriented by the application of an electric field. Such crystals are called ferroelectric, a term first used by analogy with ferromagnetism [1-5]. The EO deflectors in chapter 2 have different indices in their different domains. The two kinds of domains, with either a positive or a negative index change in one congruent substrate, cannot be constructed using natural crystals, and thus are constructed using ferromagnetic materials in which domain inversion is performed. The polarization vector of a material is expressed by the density of permanent or induced electric dipole moments. Usually, a spontaneous polarization follows the z-direction, the direction parallel to the optical axis of the material. The original (spontaneous) polarization and the inverted polarization, identified by a positive or negative sign as shown in Fig. 3.1.1, are parallel to the z-axis.

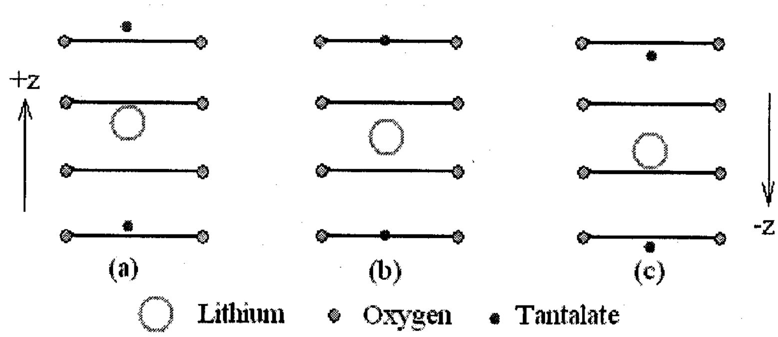

Fig. 3.2.1 Three dipole states of $LiTaO_3$: (a) positive, (b) normal, (c) negative

$LiNbO_3$ and $LiTaO_3$ are the two main ferroelectric materials used in most EO deflectors. In these materials, the metal ions Li and Nb can be shifted along the optical axis (Fig. 3.2.1). Thus, the spontaneous polarization can be reversed or reoriented by the application of an electric field larger than the coercive field of the crystals. This displacement of the metal ions persists even in the absence of an electric field. Fig. 3.2.2 illustrates the spontaneous polarization direction and the reversed polarization direction after the application of an external E-field.

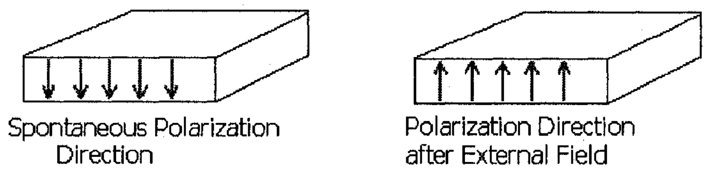

Fig. 3.2.2 Polarization directions of the crystal. Left: spontaneous polarization direction; Right: the direction after the application of an E-field

$LiNbO_3$ and $LiTaO_3$ are uniaxial crystals with n_x=n_y and n_z=n_e. As demonstrated by their index ellipsoids in Fig. 3.2.3, their spontaneous polarization follows the z-axis with an index n_e. The other two indices along the x and y coordinates are n_0. The structure of a z-cut single crystal wafer with the surface perpendicular to the z-axis is also shown in the index ellipsoid.

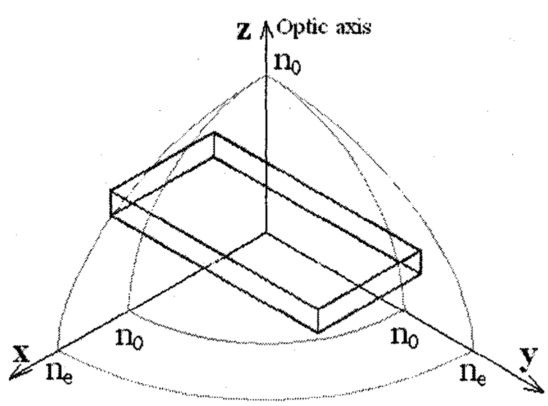

Fig. 3.2.3 Index ellipsoid of a z-cut $LiTaO_3$ crystal

3.2.2 Parameters of the Wafer

Three-inch $LiTaO_3$/ $LiNbO_3$ wafers, z-cut, 0.5 mm thick, purchased from Foctek Photonics, Inc. served as substrates in our experiments. Table 3.2.1 lists some of the parameters of these wafers to gain a better understanding of the crystals. The small value for hardness reveals that the wafers are fragile and the Curie temperature indicates the temperature during fabrication cannot exceed 1160°C for $LiNbO_3$ or 600 °C for $LiTaO_3$. A wavelength of 1310 nm was used in the measurements of the EO systems since the index is larger at lower wavelength [6], which leads to a larger deflection angle in the EO devices. Being ferroelectric materials, the spontaneous polarization direction of $LiNbO_3$ and $LiTaO_3$ can be reversed; the theory and the process of the domain inversion will be presented in detail in section 3.4.

Table 3.2.1 Properties of $LiNbO_3$ / $LiTaO_3$ crystals (the datasheet is from Eoctek Photonics, Inc.)

Parameter	$LiNbO_3$	$LiTaO_3$
Melting Point	1250°C	1650°C
Curie Temperature	1160°C	607 °C
Crystal System	Trigonal	Trigonal
Point Group	3m	3m
Hardness (Mohs)	5	6
Crystal Density	$4.64x10^3kg/m^3$	$7.465\ x10^3kg/m^3$
TE mode index: n_0 At 1310 nm	2.14	2.176
TM mode index: n_e At 1310 nm	2.22	2.18
Dielectric Constant	29	44
EO co-efficient: r_{33}	$31x10^{-12}mV^{-1}$	$30.5\ x10^{-12}mV^{-1}$
EO co-efficient: r_{13}	$8.6\ x10^{-12}mV^{-1}$	$8.4\ x10^{-12}mV^{-1}$
Transmission Range, μm	0.35-5.5	0.45-5.0
Coercive fields	21kV/mm	21kV/mm

3.2.3 The Wafer Process

The z-cut $LiTaO_3$ materials come as 3" 500μm thick wafers, each capable of producing 10-15 different devices. Patterned masks are sketched for both the poling electrodes and driving electrodes, which are lithographed, metal evaporated, and lifted off on the substrates. The design of the patterns of the poling and driving electrodes is introduced in the next section. A high voltage electric field (10 kV) is applied through the poling electrodes to invert the spontaneous polarization domains on the wafers. The Poling process will be described in section 3.3. The driving electrodes are metallized on the same surface as the poling electrodes, while the back side of the wafer is all covered by electrodes which serve as ground. After metallization of the wafer is complete, the EO devices are diced out of the substrate and are polished on the left and right facets to produce EO deflectors or EO switches. The EO devices are then ready for testing and later packaging.

3.3 Mask Design

Two types of electrodes are used to generate the external electric field applied to the wafers: the poling electrodes for the purpose of domain inversion and the driving electrodes for the purpose of index change in the substrates. Usually, one mask contains both of the electrode patterns as two layers. In our experiments, the masks were sketched in AutoCAD and fabricated by Adtek Photomask Inc.

3.3.1 The two Layers in the Mask

The two-layer masks are confined in a circle of radius 3” that corresponds to the contour line of the wafer as Fig. 3.3.1 shown. The first layer of the mask contains the patterns of the poling electrodes, built of concatenated prisms with each prism’s vertex following a designed geometry. A Matlab program calculates the coordinates of the points of prisms; defines these prisms in the format of AutoCAD command; and creates a file with an SCR extension (Appendix A). Through the *scr* command, AutoCAD uses this file to create the electrode patterns.

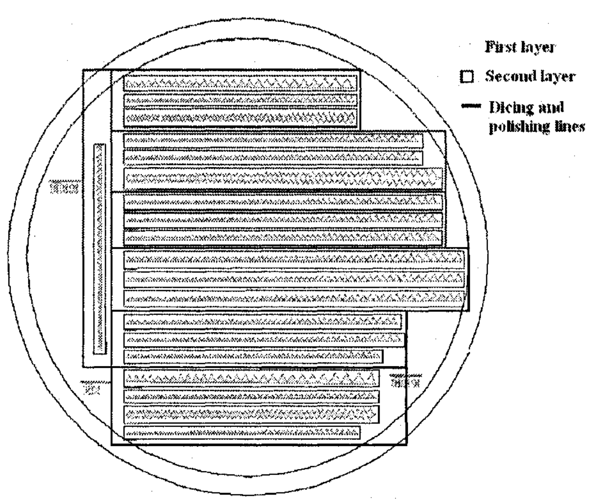

Fig. 3.3.1 Two-layer mask with dicing lines

The second layer of the mask contains the patterns of the driving electrodes, which are the electrodes used to generate the external E-field to utilize the EO effect. The exact outer shape for a domain inverted substrate should follow the contour area as shown in Fig. 3.3.2 (a). However, rectangular contour lines as shown in Fig. 3.3.2 (b) are also acceptable when the light beam only transmits along the prism region after the application of E-field.

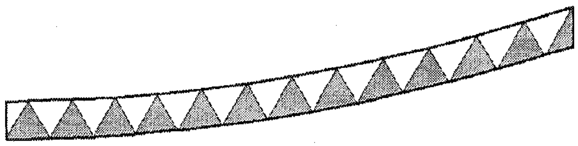

(a)

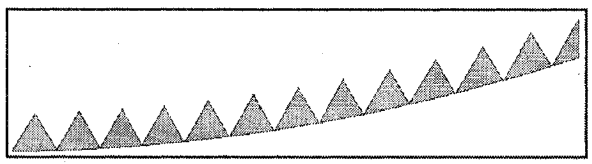

(b)

Fig. 3.3.2 Outer shape for the parabola shaped device. (a) exact outer shape; (b) rectangular contour lines.

Several EO device patterns are arranged in one 3" mask to reduce the manufacturing cost as shown in Fig. 3.3.1. The devices are then diced out according to the dicing lines also shown in Fig. 3.3.1. Instead of one device, a group of 3-4 devices in one final piece is introduced to reduce the probability of broken devices during the dicing and polishing process due to the super-slim device shape.

3.3.2 Photolithography and Metallization

All the procedures described here, such as patterning, photolithography, metal evaporation, and liftoff, were carried out by the University of Sherbrooke.

The same processes of photolithography and metallization are used for both types of electrodes. During the photolithography, the cleaned wafer is spread with a combination of Lift-off resist (LOR) and regular photo-resist, which ensures the best lithographic results with $LiTaO_3$. The wafer is then exposed to UV light through the patterned mask, using a mask aligner, and developed by immersion in a special developer adapted for photo-resist and LOR. After that, the wafer is rinsed with deionized water, dried with nitrogen, and descumed with oxygen plasma.

Evaporation and metallization are performed in a thermal evaporator. Chromium and gold with thicknesses of 20 nm and 80 nm, respectively, are deposited through evaporation. Using the LOR solvent and heat, the LOR is lifted off and the residues are removed by solvent filtration. The wafer is then cleaned with acetone and isopropanol and dried with a nitrogen jet. The patterned electrodes are now deposited on the substrate.

3.4 Wafer Poling

As described in chapter 2, by applying voltages to the designed areas, the domains in those areas can be inverted. Thus, different polarization directions in one contiguous substrate are accomplished. The prism-shaped pattern is chosen according to the discussion in chapter 2 and is metallized as the poling electrodes on the –z surface. Fig. 3.4.1 shows one of the rectangular patterns, and the 3D viewing of the two domains (a head to tail polarization direction) in the crystal after poling.

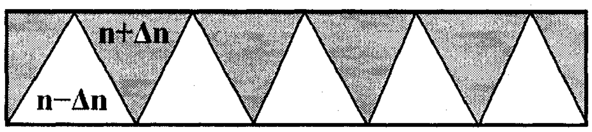

(a)

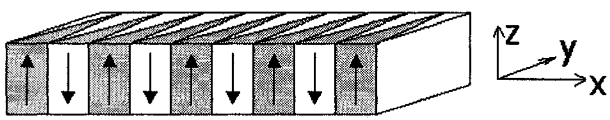

(b)

Fig. 3.4.1 Rectangular patterns. (a) top view of the pattern; (b) 3D viewing of the poled crystal

The process used to invert the spontaneous polarization direction of the ferroelectric material is called poling. Various methods of poling are available, such as chemical, heating, and application of an electric field [7]. Among them, the electric field poling offers a practical means, considering the facilities that are available in our lab.

Steady-state voltage application and pulsed-voltage application are two methods used to invert domains [8]. In the first poling method, a constant voltage is applied to the substrate through the entire domain inversion period. In the second method, a series of high voltage pulses is applied to the substrate and each pulse can partially reverse the dipole moment within the poling area. Although the poling by a steady-state electric field can induce the process of domain inversion faster, it is difficult to control and handle due to the fast switching time of the domains, which is usually 200-2300 μm/s. Conversely, the switching time of domains in the pulsed voltage application is slower, but by monitoring the current during the reversal of the dipole moment, the series of pulses can be controlled more easily and it is the method that we chose.

3.4.1 Setup for Wafer Poling

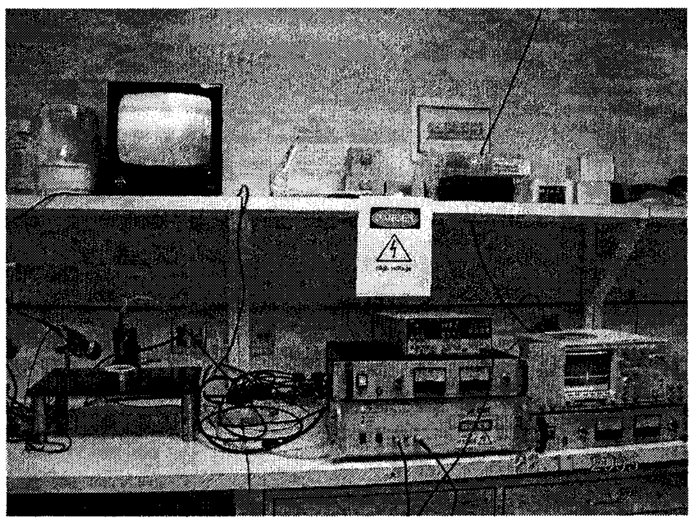

Fig. 3.4.2 Lab setup for wafer poling

During the electric field poling process, a voltage of 10 kV is applied between the -z and +z surfaces. The poling electrodes are deposited on the –z surface because the spontaneous polarization direction is from +z to -z surfaces. An entire layer of conductive grease connects the metallized +z surface of the wafer to the brass trunk.

The brass trunk connects the +z surface of the wafer to the negative high voltage supply of -15 kV. Another high voltage power supply provides up to 1 kV pulses to the wafer surface with driving electrodes. The total electric field must exceed the coercive fields of the material, which is approximately 11 – 12 kV. High voltage pulses of eight microseconds are applied to the wafers repeatedly until the dipole moment is completely reversed. The setup of the poling is shown in Fig. 3.4.3, while the lab setup is shown in Fig. 3.4.2.

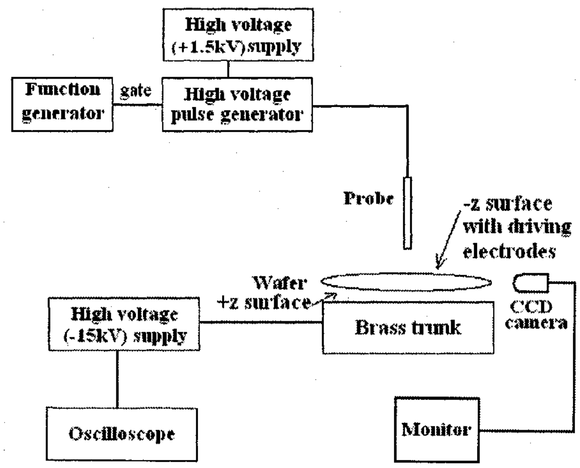

Fig. 3.4.3 Schematic of the poling setup

3.4.2 Wafer Mounting

Substrates that are to be poled are mounted on the brass trunk in steps as follows:

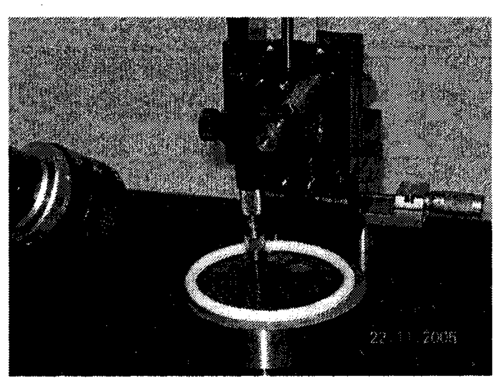

Fig. 3.4.4 Wafer mounted on the poling setup

Step 1) Evenly spread a thin coat of conductive grease on the surface of the mounting trunk.

Step 2) Rinse the wafer with acetone and dry it with nitrogen gas. Place the wafer face-up (electrodes up) on the mounting trunk using tweezers.

Step 3) Cover the wafer with a piece of paper filter, which has been immersed in mineral oil; punch a small hole in the filter for the spring probe to go through. Place a Teflon o-ring on top of the filter. Both the filter and the o-ring prevent arcing.

Step 4) Slowly push down the spring probe through the hole toward the wafer and monitor it until it almost reaches the wafer surface.

Step 5) Use a voltmeter to verify proper contact between the probe and the electrodes: connect the black lead of the voltmeter to the probe; replace the red lead with the Nano-clip contact and bring it near the electrodes on the wafer. The Nano-clip has an extremely soft hook, which can protect the wafer from compressive stress. Push the spring probe down until it finally touches the electrodes.

Step 6) Connect the probe to the positive high voltage cable. The mounted wafer and the setup are shown in Fig. 3.4.4.

After these steps, the wafer is mounted on the stage and high voltage can be applied to invert the spontaneous polarization directions.

3.4.3 Poling Procedures

The connections are established using the setup shown in Fig. 3.3.3. The output of a 15 kV high voltage power supply is slowly decreased from 0 V to -12 kV till it reaches coercive field. The +1.5 kV high voltage power supply is set to 800 V, which provides the voltage for the high voltage pulse generator. The pulse is generated by a function generator set to 5 V, 8 ms duration, and single manual shot. The threshold E-field of 500 μm $LiTaO_3$ is 11.5 kV, which is half of the coercive field (23 kV/mm). Including the 800 V pulses, the starting domain-switching voltage on the -15 kV high voltage power supply is approximately - (1150 - 800) = -10.7 kV. The coercive voltage cannot accurately be predetermined as the thickness of the wafer may not be exactly 0.5mm. Pulses are therefore applied to the substrate while the supporting voltage decreases step by step. Once the threshold voltage is achieved, the dipole moment will start to be reversed and a small current, as shown in Fig. 3.4.5, will occur during the inversion, which can be detected through the current monitor provided by the -15 kV power supply. More pulses might be needed after the voltage exceeds the threshold to ensure a complete reversal of the domain. Once the current pulse stops, the entire voltage application can be terminated and the process of poling is complete.

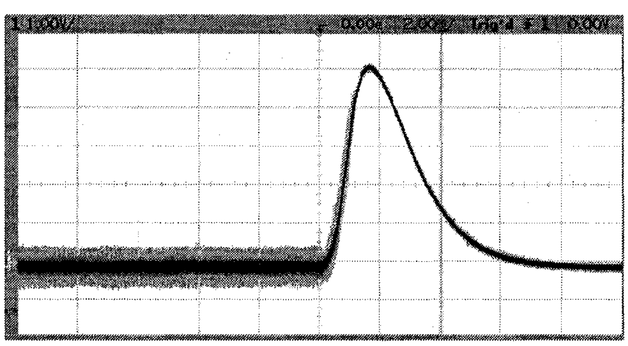

Fig. 3.4.5 Current pulse when poling occurs

After poling, the spring probe, the ring, and the paper are removed; the wafer is gently pushed aside using the wafer tweezers; and the wafer is immersed and cleaned in soapy water, rinsed with acetone, and dried with nitrogen gas.

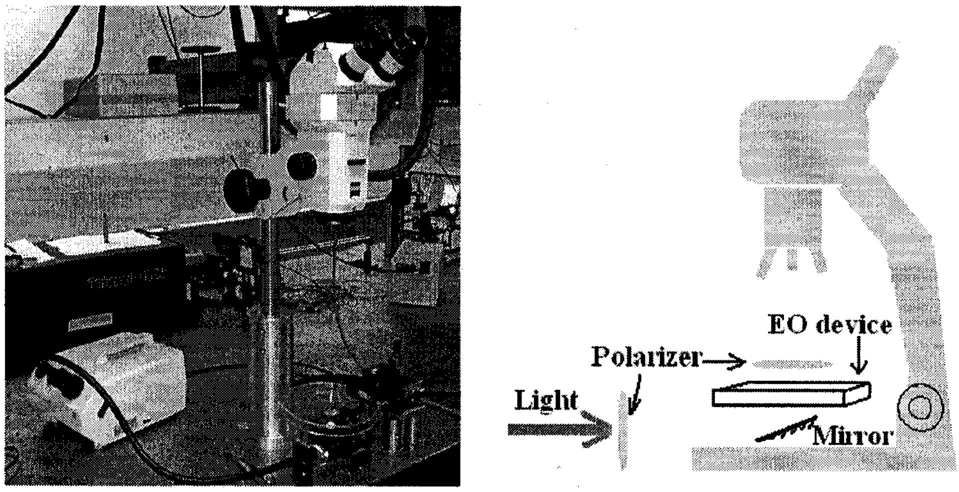

Fig. 3.4.6 Microscope setup to check the domains

The poling results can be examined under a microscope with cross polarizers [9]. Fig. 3.4.6 shows the setup and the equipment used in the lab. Fig. 3.4.7 and Fig. 3.4.8 show successful and unsuccessful poling results.

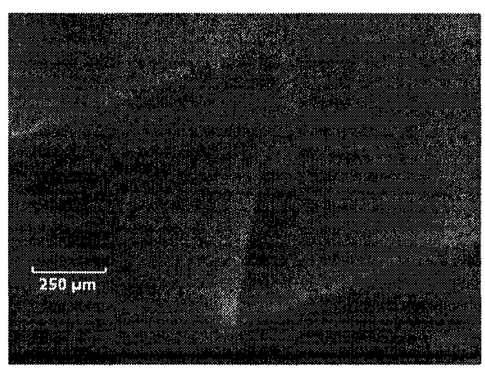

Fig. 3.4.7 Poled domains under cross-polarizers

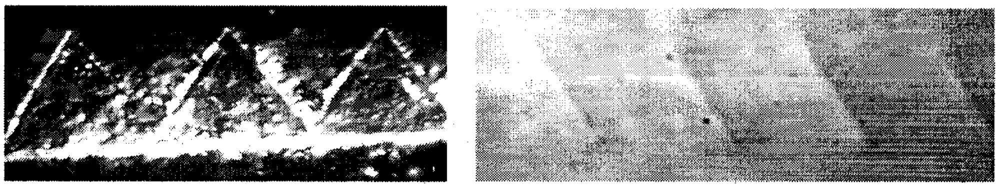

Fig. 3.4.8 Examples of domains which are over poled and under poled

Some problems may occur during the poling process. Sometimes, no poling occurs if the electrodes are metallized on the +z surface instead of the –z surface. Another common problem is arcing. Arcing is the flow of electricity through the air from one conductor to another, which can produce visible flashes and flames along with a crackling sound. Normally, 10 kV voltages arc over a 3 mm distance of a dry air gap [10]. In the procedure of poling, arcing can not only damage the spring probe, but also crack the crystal.

Arcing might happen if the voltage is too high or the pulse setting is too long, or if the electrodes are designed too close (less than 3 mm) to the contour line of the wafer. If there are some connections between the ground and the electrodes, as can happen when conductive grease gets smeared onto the top surface of the wafer, arcing might happen as well. And once arcing happens, the spring probe should be replaced immediately to prevent further problems.

After poling, the driving electrodes and ground electrodes are deposited on the wafer. EO devices are diced out from the substrate and each facet is polished. These devices will then be used in the non-rectangular shaped EO deflectors as described in chapter 4 or in the packaged EO switches as described in chapter 5.

3.5 Conclusion

In this chapter, EO ferroelectric materials are first investigated. The optimally designed geometries of the prisms are sketched as electrode patterns in photomasks. The poling electrodes are lithographed and metallized onto the EO substrates from these photomasks, and the spontaneous domains of the prisms regions are then inverted by electric field poling. After a second photolithography, metallization and lift-off, the driving electrodes are deposited on the substrates. The wafer then is diced and polished to get the designed EO devices.

3.6 References

[1] S.N. Zhu, Y.Y. Zhu, Z.Y. Zhang, H. Shu, H.F. Wang, J.F. Hong, C.Z. Ge, and N.B. Ming, "$LiTaO_3$ crystal periodically poled by applying an external pulsed field," *Journal of Applied Physics*, Vol. 77, pp.5481-5483, 1995.

[2] L.E. Myers, R.C. Eckardt, M.M. Fejer, R.L. Byer, W.R. Bosenberg, and J. W. Pierce, "Quasi-phase-matched optical parametric oscillators in bulk periodically poled $LiNbO_3$," *Journal of the Optical Society of America B*, Vol. 12, pp. 2102-2116, 1995.

[3] A.V. Golenishchev-Kutuzov, V.A. Golenishchev-Kutuzov, and R.I. Kalimullin, "Induced domains and periodic domain structures in electrically and magnetically ordered materials," *Physics-Uspekhi*, Vol. 43, pp.647-662, 2000.

[4] V. Gopalan and T.E. Mitchell, "In situ video observation of 180° domain switching in $LiTaO_3$ by electro-optic imaging microscopy," *Journal of Applied Physics*, Vol. 85, pp. 2304-2311, 1999.

[5] V. Gopalan and T.E. Mitchell, "Wall velocities, Switching times, and stabilization mechanism of 180° domains in congruent $LiTaO_3$ crystals," *Journal of Applied Physics*, Vol. 83, pp. 941-954, 1998.

[6] U. Schlarb and K. Betzler, "Refractive indices of lithium niobate as a function of temperature, wavelength, and composition – a generalized fit," *Physical Review B*, Vol. 48, pp. 15613-15620, 1993.

[7] Measuring high voltages by spark length
http://www.kronjaeger.com/hv/hv/msr/spk/

[8] V. Gopalan, S.S.A. Gerstl, A. Itagi, Q.X. Jia, T.E. Mitchell, T.E. Schlesinger, and D.D. Stancil, "Mobility of 180° domain walls in congruent $LiTaO_3$ measured using in-situ electro-optic imaging microscopy," *Journal of Applied Physics*, Vol.

86, pp. 1638-1646, 1999.

[9] V. Gopalan and M.C. Gupta, "Origin of internal field and visualization of 180° domains in congruent $LiTaO_3$ crystals," *Journal of Applied Physics*, Vol. 80, pp. 6099-6106, 1996.

[10] Measuring high voltages http://www.kronjaeger.com/hv-old/hv/tbl/measure.html.

Chapter 4: New Geometrical Shapes for EO Deflectors

4.1 Introduction

In Chapter 2 the concept of EO deflectors was introduced and in Chapter 3 the fabrication procedure of the EO devices was described, including domain inversion and electrodes deposition. In this Chapter, some new geometrical EO deflectors are proposed. These deflectors are specially designed for the application of EO switches and are based on non-rectangular shapes. The optimal design that is proposed for EO switches was fabricated and tested. Some other devices using new shapes are presented with experimental results. These new deflectors are compared to existing EO deflectors using the deflector figure of merit presented in section 4.3. Analysis in this chapter shows that the new proposed deflectors demonstrate better deflection capabilities than any other bulk devices. Also, the concept of non-blocking 2x2 EO switches based on the new deflectors is described in this chapter.

The analysis and theory derivation are presented in section 4.2; the new deflectors are introduced in Sections 4.4 and 4.6. The deflection performances of existing EO deflectors are compared and analyzed in Section 4.5. Experimental results of the new devices, such as deflection angles, output spots, insertion loss, crosstalk, response time, and other parameters are presented in Section 4.7. Conclusions are given in Section 4.8, and Section 4.9 lists all the references.

4.2 Equivalency Theory

Previously in Chapter 2, the two common structures used for EO deflectors, the prism and the gradient index are introduced. [1], [2] have proved that for a deflector with rectangular shape, the performance of the prism and linear gradient deflector is identical for given device dimensions and maximum index difference as Fig. 4.2.1 shows. Based on that, a new equivalency theory [3], developed as part of this thesis work, extends the existing equivalency theory to any deflector shape, not just rectangular deflectors.

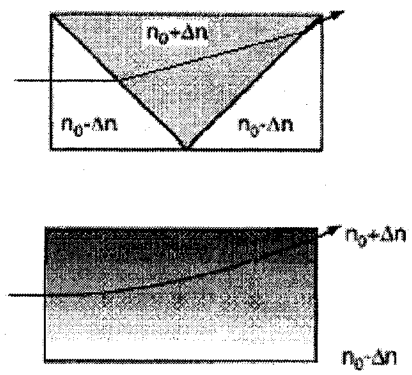

Fig. 4.2.1 Two deflectors with different structures [2]

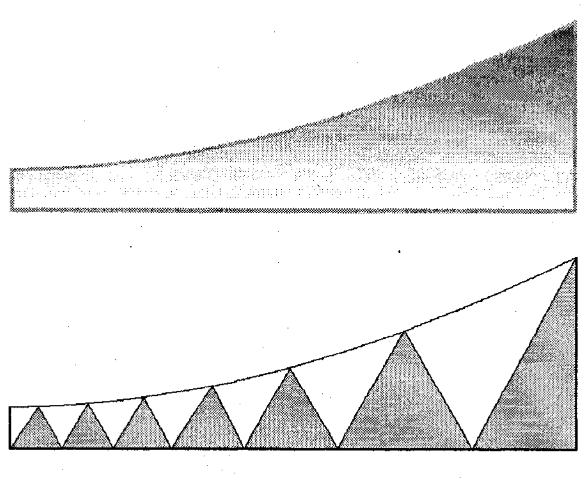

Fig. 4.2.2 Two deflector types: the first is a gradient index structure and the second is a prism type structure

To prove this equivalency theorem, a special prism deflector was built as shown in Fig. 4.2.2. The deflector has a constant transverse index created by using a cascade of prisms across its length. These prisms are placed side-by-side and parallel to one another. The apex and base of all the prisms are aligned with the upper and bottom edges of the deflector respectively.

Since all prisms have a constant apex angle β, the whole region can be divided into small regions where each one corresponds to one prism. The total length of the device is equal to the sum of the lengths of all the prism bases. Given such a structure, the integration in the z direction can be expressed as a summation of the contribution of each prism. Equation (17) in Chapter 2 can be rewritten as:

$$\Delta\theta = \int \frac{2\Delta n}{n_0} \frac{1}{W(z)} dz = \sum_i \frac{2\Delta n}{n} \frac{z_i}{W_i} = \frac{4\Delta n}{n} \sum_i \frac{L_i / 2}{W_i} \tag{1}$$

By comparing (1) and (14) in Chapter 2, it can be concluded that the deflection performance of prism shaped designs and gradient index based designs are identical. Furthermore, for any EO device shape, the iterated-prism structure is entirely equivalent to its corresponding constant transverse index gradient structure.

My new conclusion is very useful in EO device design. Indeed, instead of a complicated deflector structure analysis, a simple ray tracing analysis can be used to determine the performance of any EO device shape. Simulation in Code V and BPM, as well as the experimental results in later of this chapter and chapter 5 all proved that the theory does work and is useful in the design and analysis.

4.3 Deflector Figure of Merit

Equations (1) has reveal that the total deflection performance depends on several variables such as length, initial width and shape of the device, thickness of the substrate, and applied electric field. Several EO device designs have been documented both in the present study and in the literature. In the latter, deflection sensitivity is defined as "the deflection angle per applied voltage." However, as mentioned previously, many other variables also should be considered when defining deflection sensitivity. In an attempt to compare all devices, the product of the applied E-field and the electrode length is defined as a figure of merit for the EO deflectors. Although it is the first time this product is used as a figure of merit with EO deflectors, it is widely used with EO modulators [4]. By definition, this product which we call deflector figure of merit, is given by:

$$\text{Figure of Merit} = VL/D \tag{2}$$

where V is the applied voltage on the device, D is the thickness of the substrate, L is the device length, and V/D represents the E-field in the device. The typical applied voltage in bulk material is around 1000 V while this voltage might be lower in thin-wafer devices.

Also, deflectors can be based on either bulk materials (500 μm) or on thin substrates (100 μm). When comparing the deflectors, we also report the incident diameter of the light beam for more clarity. The detailed values for different kinds of devices will be given in section 4.5, after proposing more deflectors. The comparison and analysis will also be given in that section.

4.4 Optimal Geometry Design

4.4.1 New Geometry with Best Deflection Angle

Non-rectangular shaped deflectors are advantageous because of their better steering performance, and thus are welcomed in many applications. Previous literature has mentioned some non-rectangular devices, which are for the application of optical scanning [2]. Here, more optimal designs are proposed for the application of optical switching. Instead of applying continuous positive and negative voltages, switching applies only discrete voltages on the devices and the geometry designs are optimized differently. Here, the design of a deflector is to determine the best contour or envelope of the prisms since different contours provide different optical path and thus the deflection angles are different. Once the contour is determined, a series of equilateral triangles will fill in with vertices located on the contours.

Specifically, the design with the best deflection performance satisfies the following requirements. First, the entire light beam needs to be encapsulated by the prism structures to reduce the exhibited insertion loss. Second, the center of the light beam should meet the interfaces of each prism at its center as shown in Fig. 4.4.1. This will ensure that the largest beam spot is obtained and that losses on the output side are minimized.

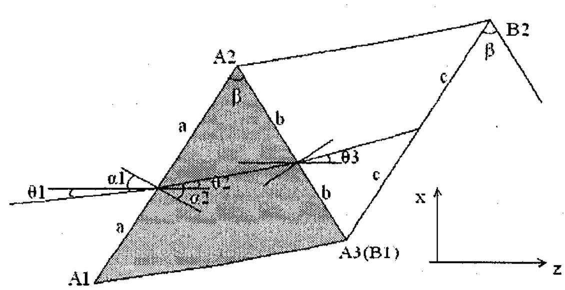

Fig. 4.4.1 Light trace at each interface

As shown in Fig. 4.4.1, a two prism model has been demonstrated for analysis. In this model, the dark region has a lower index and the light region has a higher index. Two prisms have the same vertex angles β. The light beam meets the interfaces of the prisms at the center of A1A2, A2A3, and A3B2, respectively. Assuming the incidence angle and refraction angle at each interfaces are θ_1, θ_2, and θ_2, θ_3, the length c is derived and calculated as follows:

$$\begin{aligned} c &= b\frac{\sin(\beta+\theta_3)}{\sin(\beta-\theta_3)} = a\frac{\sin(\beta+\theta_3)}{\sin(\beta-\theta_3)}\frac{\sin(\beta-\theta_2)}{\sin(\beta+\theta_2)} \\ &= a\frac{\cos(2\beta+\theta_3-\theta_2)-\cos(\theta_2+\theta_3)}{\cos(2\beta+\theta_3-\theta_2)-\cos(\theta_2+\theta_3)} \end{aligned} \tag{3}$$

Since $\theta_3-\theta_2$ is typically very small, $c \approx a$.

Since all prisms have an identical apex angle, which is 60°, and a constant half edge length, all the prisms should be identical. The upper and bottom edges of the device should be parallel. Considering (1), when using a constant prism width W, the obtained deflection performance is superior to any variable width device implementation.

Assuming the initial incidence angle is zero, the total deflection angle after N prisms is:

$$\begin{aligned} \theta_k &= \Delta\theta = \frac{2\Delta n}{n}\sum_i \frac{L_i/2}{W_i} = \frac{2\Delta n}{nW}\sum_i LM_i \\ &= \frac{2\Delta n}{nW} z_{middle} = \frac{\Delta n}{nW} z \end{aligned} \tag{4}$$

where LM_i is the distance between the middle points of each prism, and z_{middle} and z are the z-axis values of the middle point and edge point, respectively.

Furthermore,

$$\theta_k \approx \tan(\theta_k) = \frac{\Delta x}{\Delta z} \tag{5}$$

$$\frac{\Delta x}{\Delta z} = \frac{\Delta n}{nW} z = \frac{dx}{dz} \qquad\qquad x = \frac{\Delta n}{2nW} z^2 \tag{6}$$

Equation (6) indicates that the beam follows a parabolic trajectory through the prisms. Since it is required that the beam traverse through the middle of each prism, the outer shape of the device is also parabolic. Fig. 4.4.2 illustrates the resulting shape of the EO deflector.

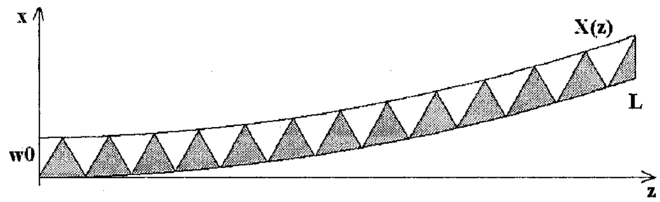

Fig. 4.4.2 Parabola shaped design with prisms

The same conclusion can be derived from ray equations too. According to the device structure, the index changes linearly along the z-axis as follows,

$$n = n_0 + \frac{X(z) - M(z)}{W_0} \Delta n \tag{7}$$

Thus, according to the equations (16) and (17) in Chapter 2, which is based on the gradient structure analysis, deflection angle θ and trajectory x can be derived:

$$\theta_P = \frac{\Delta n L}{n_0 W} \qquad\qquad x = \frac{\Delta n}{2 n_0 W} z^2 \tag{8}$$

Equation (8) indicates that longer device length and narrow device width can provide larger deflection angles.

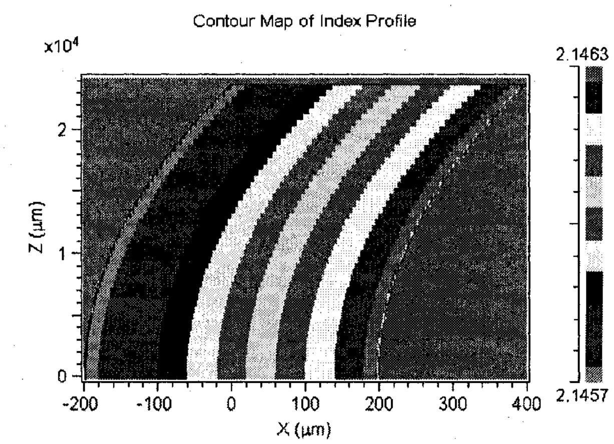

Fig. 4.4.3 Gradient index profile in BPM simulation

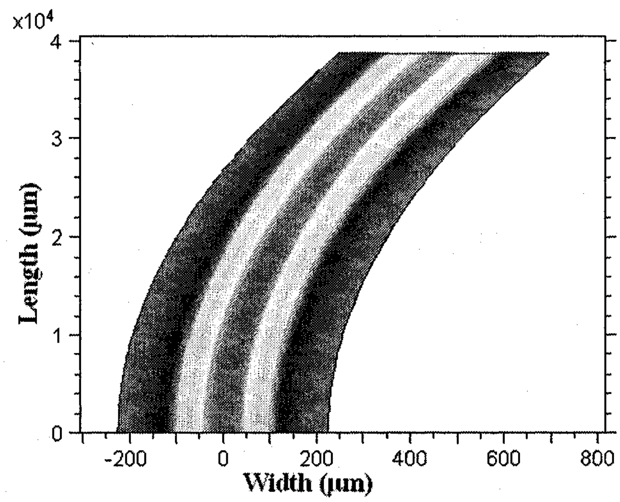

Fig. 4.4.4 Beam trace in BPM simulation

Simulations using commercial software, such as Code V and RSoft BPM (Beam Propagation Methods) were developed to verify the initial designs. Based on the results of equation (8), a deflector of parabolic shape with linear gradient index can be defined in BPM as Fig. 4.4.3 shows. The simulated beam trace is provided in Fig. 4.4.4. Also, another model was built in Code V. The structure is created by a series of prisms with different indexes and the interfaces are defined in Fig. 4.4.5. The simulated beam bending, shown in Fig. 4.4.6, indicates that this prism model gives the same result as the gradient structure model. Thus, the equivalent theory is proved in these simulations. The deflection angles of Matlab, Code V, and BPM simulation are summarized in Table 4.4.1.

Table 4.4.1 Comparison of Matlab, Code V and BPM results for a device with 400 um width, and 23.67 mm length under 1000 V voltage

Voltage	Deflection Angle:		Deflected Distance:		
	CODE V	Matlab	CODE V	Matlab	BPM
1.0 kV	2.02°	2.14°	0.190 mm	0.203 mm	0.204 mm

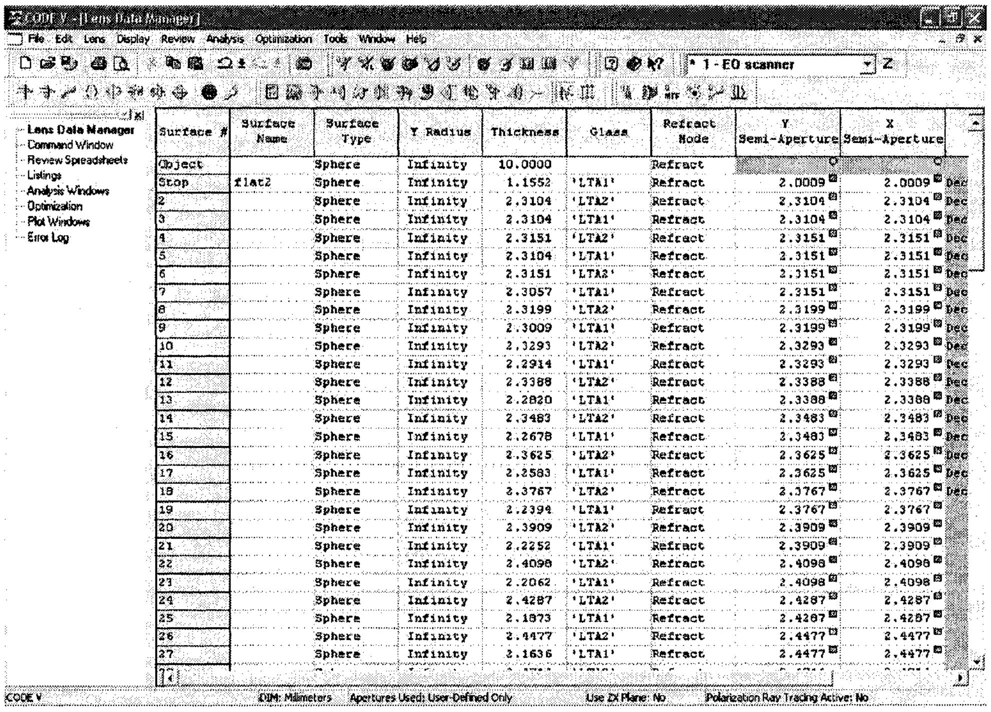

Fig. 4.4.5 Interfaces definition in Code V

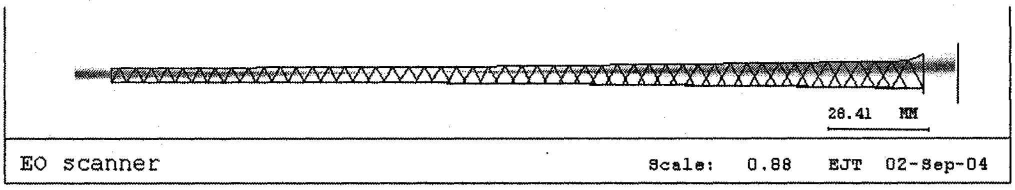

Fig. 4.4.6 Beam trace in Code V simulation

4.4.2 Other New Geometry

Another geometry can be derived using ray equations. The nonrectangular scanners such as the horn shaped devices [5], [6] are modified, and a half-horn shaped device is proposed.

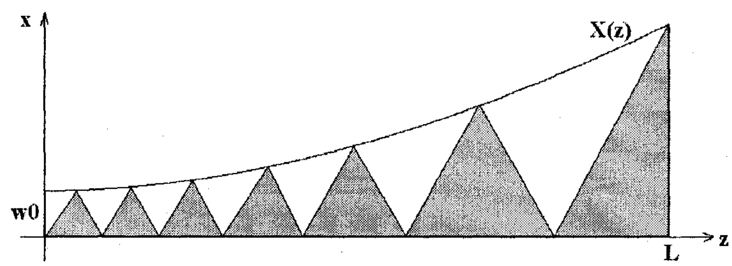

Fig. 4.4.7 The Half-Horn shaped design with prisms

In this structure, we assume that the bottom line of the device has the same index of $n_0 - \Delta n/2$, and that the index changes linearly along the z direction until it reaches $n_0 + \Delta n/2$ at the top edge, as Fig. 4.4.7 shows. Here the index is,

$$n = n_0 - \frac{\Delta n}{2} + \frac{\Delta n}{W(z)} X \tag{9}$$

where *W(z)* is the width of the device across its length, and W_0 is the width at the input end. According to gradient structure analysis, as presented in Equation (16) and (17) of Chapter 2, the shape of the device is computed as follows,

$$\frac{dW}{dz} = \sqrt{\int 2 \frac{\Delta n}{n_0} \frac{1}{W(z)} dz} = \sqrt{\frac{2\Delta n}{n_0} \ln(\frac{W(z)}{W_0})} \tag{10}$$

Since at *z=L*,

$$\theta = \sqrt{\frac{2\Delta n}{n_0} \ln(\frac{W(L)}{W_0})} \tag{11}$$

Since no closed form solution for *W(z)* can be obtained from expressions (10) and (11), numerical solutions, such as Matlab simulations, were developed to analyze the performance of the devices. Fig. 4.4.8 shows the deflection angles increase as the length of the device increases. Another curve in this figure indicates that the deflection angle provided by the half-horn devices is smaller than that of the parabola shaped devices. Also, when the initial width of the device is determined, the different device lengths to achieve a given deflection angle or the different deflection angles for a given device length are given in Fig. 4.4.9.

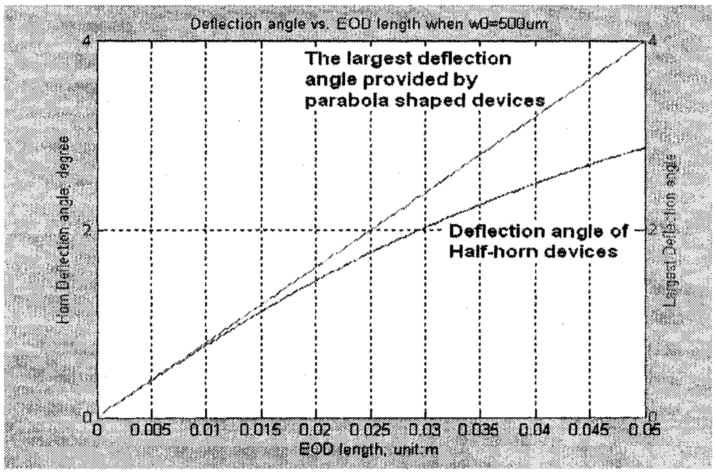

Fig. 4.4.8 Deflection angle vs. EOD length (at the width of 500 μm)

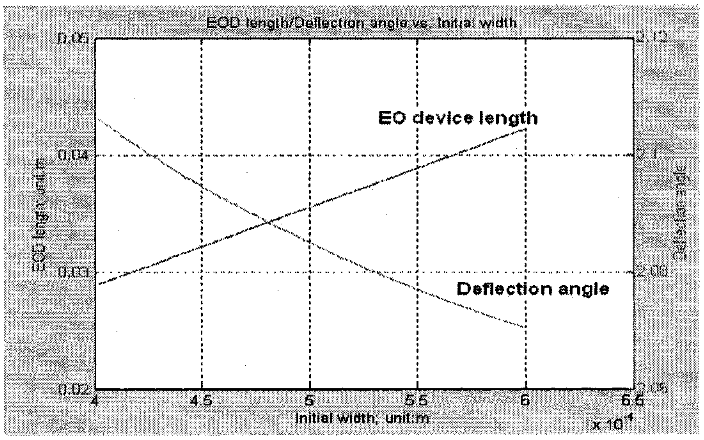

Fig. 4.4.9 EOD length/deflection angle vs. initial width

Although the upper and bottom edges of the half-horn devices are not parallel to each other, for a given voltage, beams from various incident positions trace parallel trajectories, and follow the half-horn shape as shown in Fig. 4.4.10. We can conclude that the beam traces within the devices won't be affected by the outer shape of the devices.

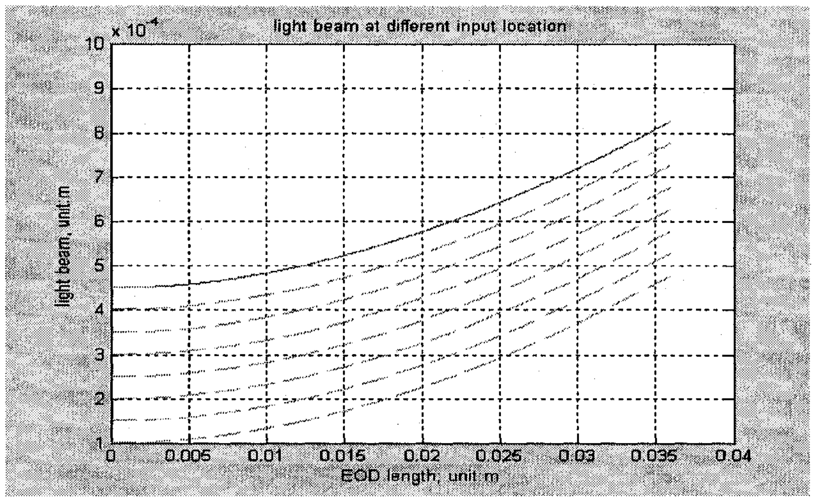

Fig. 4.4.10 Beam traces at different incident locations

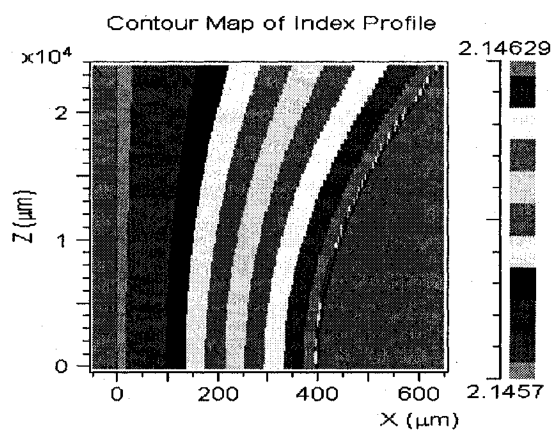

Fig. 4.4.11 Index profile in BPM simulations

Other simulations were developed to verify the initial designs, using a variety of professional software packages, such as Code V and RSoft BPM. The gradient index model in BPM is established as Fig. 4.4.11. Instead of operating at one voltage, continuous voltages can be applied on these EO devices and different deflection angles can be achieved. Fig. 4.4.12 and Fig. 4.4.13 show the beam tracing of 1000V voltage and 500V voltages. These devices usually work in applications that require an optical beam scanner. The results in Table 4.4.2 are comparisons of Matlab, Code V, and BPM simulation results and they are similar to each other.

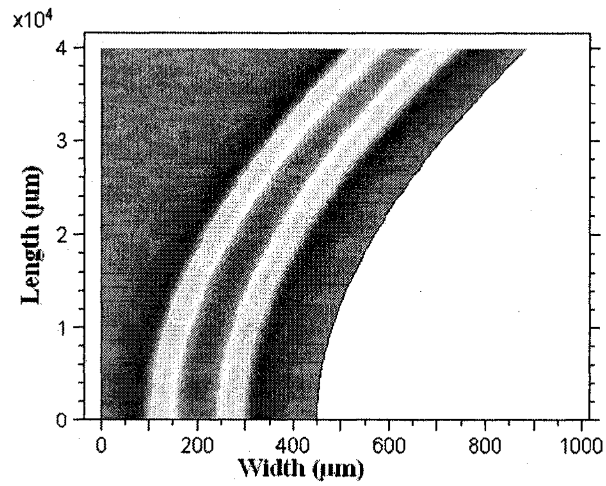

Fig. 4.4.12 BPM simulations of the half-horn shaped deflectors at 1000V voltage

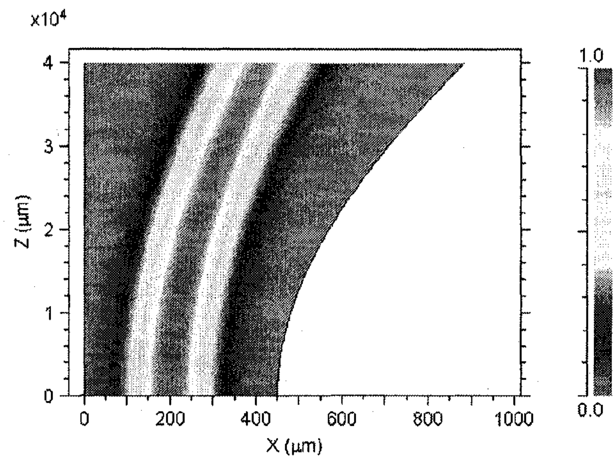

Fig. 4.4.13 BPM simulations of the half-horn shaped deflectors at 500V voltage

Table 4.4.2 Comparison of BPM, Code V, and Matlab results

Voltage	Deflection Angle:		Deflected Distance:		
	CODE V	Matlab	CODE V	Matlab	BPM
1.0 kV	2.0657°	2.164°	0.257 mm	0.275 mm	0.276 mm

4.5 Comparisons of Existing EO Deflectors

Two novel geometries are proposed in this section and other geometries described in the literature were introduced previously. Their performances can be compared by the deflector figure of merit introduced in Section 4.3. The lower the product of E-field and device length, the better the device is.

Table 4.5.1 compares several geometries according to their structure, bulk (500 μm thick) or thin wafer (100 μm thick). From the table, we can conclude that the parabola shaped device has the smallest product; the half-horn shaped device has the second smallest value, followed by the horn and the trapezoidal shaped devices.

Table 4.5.1 Comparison of different designs

Type /Source	Length(mm) x Width(μm)	Deflection angle	Figures(10^2)
Bulk (500 μm thick)			
Parabola	40x 450	25.8 mrad	31
Rectangular [7]	8.5x460	5.37 mrad	32
Trapezoidal [2]	10x300	22.2 mrad	36
Half-Horn	40x450	20 mrad	40
Rectangular [6]	10x750	2.3 mrad	52
Horn	40x450	11 mrad	73
Thin wafer (100 μm thick)			
Parabola	10x92	105 mrad	6.4
Rectangular [8]	10x100	12 mrad	8.3
Half-Horn	10x92	55 mrad	12
Horn [9]	10x92(678)	41.7 mrad	16

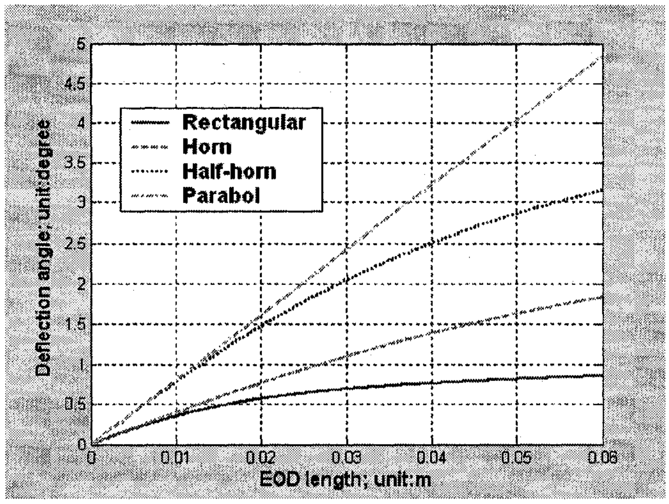

Fig. 4.5.1 Comparison of the deflection angles vs. device length

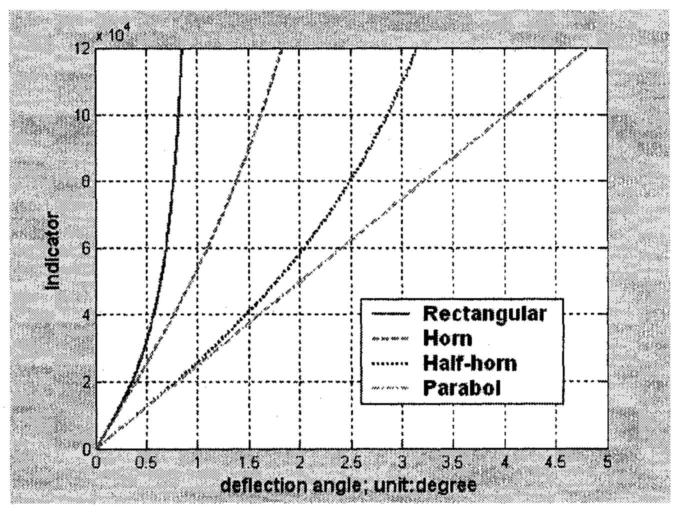

Fig. 4.5.2 Comparison of the deflection performance indicators of different geometry designs

For a given device length and applied electrical field, a comparison of (21) in Chapter 2, and (8) in Section 4.4, clearly indicates that the parabolic device will provide a deflection far greater than that obtained using a traditional rectangular shaped device. Fig. 4.5.1 is a comparison of the deflection angle obtained using the rectangular, horn, half-horn, and parabola shaped devices. Here, a device entrance width of 450 μm and an applied voltage of 1000 V on a 500 μm z-cut $LiTaO_3$ crystal were assumed. It is shown in Fig. 4.5.1 that even if the device length is large, the deflection angle of the rectangular shaped device will not exceed 15 mrad. Fig. 4.5.2 shows the deflector figure of merit of these devices for different deflection angles. To obtain 1° of deflection angle, Fig. 4.5.2 shows that figures of 15×10^4, 5.4×10^4, 2.6×10^4 and 2.5×10^4 are required in the rectangular, horn, half-horn, and parabolic geometries, respectively. Also, since the figure of merit is a non-linear function with respect to the deflection angle, Fig. 4.5.2 shows that much larger values are needed for the first three geometries, when larger deflection angles are required. The figures tell us that under similar dimension conditions, the parabola shaped device has the best deflection performance.

4.6 EO Deflectors Based on New Geometries

4.6.1 Deflector Designs

In Section 4.4, new Parabolic and Half-Horn geometries were proposed. Here, two novel optimally designed deflectors are proposed based on these geometries as shown in Fig. 4.6.1. The top sub-figure shows a deflector with a half-horn shaped envelope, the top edge of which can be expressed by (12). The bottom one shows a deflector with a parabola shaped envelope, which has a contour expressed by (13).

$$x = \frac{\Delta n}{2n_0 W} z^2 \tag{12}$$

$$\frac{dW}{dz} = \sqrt{\int 2\frac{\Delta n}{n_0}\frac{1}{W(z)}dz} = \sqrt{\frac{2\Delta n}{n_0}\ln(\frac{W(z)}{W_0})} \tag{13}$$

According to Section 4.4, in both structures, when applying a constant voltage, the trajectory of the light beam incident from Input *A* is diverted, as it travels through the prism shaped regions. Refractive beam deflection occurs at the boundaries of the prisms and the outgoing beam is detected by the receiving collimator *C*. When no voltage is applied, the incoming light beam from collimator *A* travels along a straight line and is collected by collimator *D*.

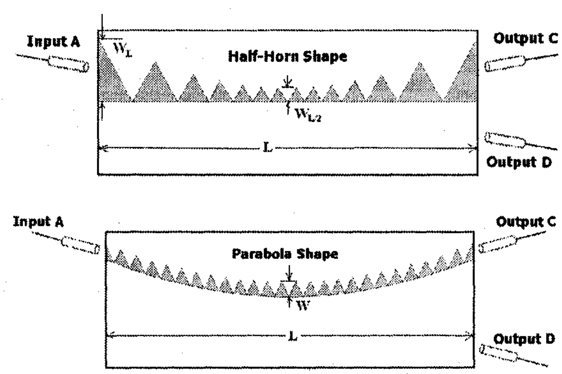

Fig. 4.6.1 Schematic of the deflectors: Top: half-horn shaped deflector; Bottom: parabola shaped deflector.

Based on the derivation and calculation of (8) and (11) in Section 4.4, the deflection angles for these geometries are:

$$\theta_{half-horn} = 2\sqrt{\frac{2\Delta n}{n_0}\ln(\frac{W_L}{W_{L/2}})} \tag{14}$$

and $$\theta_{parabola} = \frac{\Delta nL}{n_0 W_0} \tag{15}$$

Here L is the length of the device. W_0 is the height of each prism of the parabola shaped device. W_L of the half-horn shaped device is the height of the largest prism, while $W_{L/2}$ is the height of the smallest prism.

Assume a bulk device model built on $LiTaO_3$ with an index of 2.18 and an index change Δn of 1e-3. Assume the $W_{L/2}$ and W_0 are both equal to 450 μm. Fig. 4.6.2 shows the deflection angles achieved in these two devices as a function of device length L. From the plot, we notice that the angles are increasing with longer device lengths, but the increase in the parabolic shape is greater than in the half-horn shape.

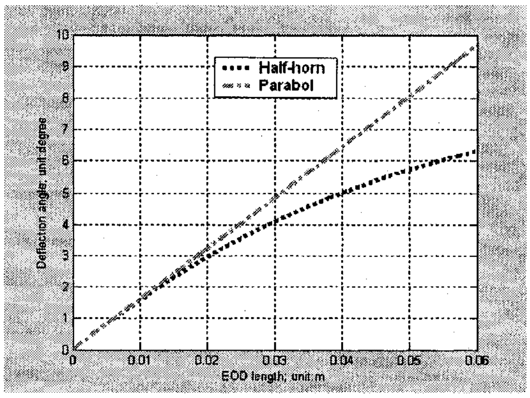

Fig. 4.6.2 Deflection angles of parabola and half-horn devices.

4.6.2 Design of the 2x2 Non-blocking Parabolic Switches

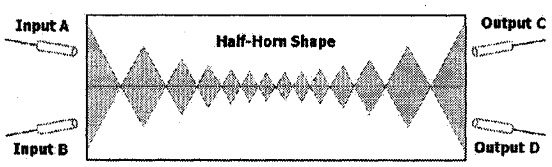

(a)

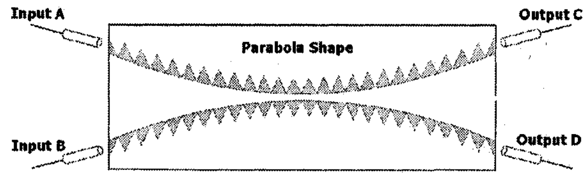

(b)

Fig. 4.6.3 The schematic of the deflectors. (a): half-horn shaped deflector; (b): parabola shaped deflector.

Non-blocking 2x2 optical switches can be constructed based upon these deflectors. A second incident collimator *B* is introduced into the deflectors (Fig. 4.6.3). The light beam from B travels along a straight line and is detected by collimator *C* when there is no outside voltage. If a proper voltage is applied, the light beam incoming from *B* will travel alongside the pre-defined half-horn (or parabola) trajectory and is collected by collimator *D* at the output. The bar and cross status of the switches can be obtained, as shown in Fig. 4.6.4.

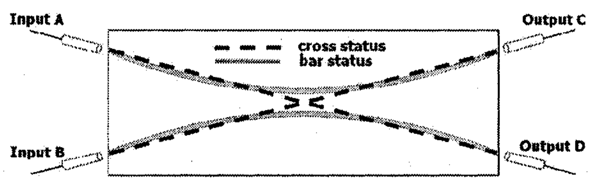

Fig. 4.6.4 The cross and bar status of the non-blocking optical switch based on the EO deflectors

In the non-blocking 2x2 switch, two input beams have to travel to the same two output receivers in both Cross and Bar status. Thus the distance between the upper and lower channel becomes critical. The amount of distance between the upper and lower deflectors has to be considered as Fig. 4.6.5 shows.

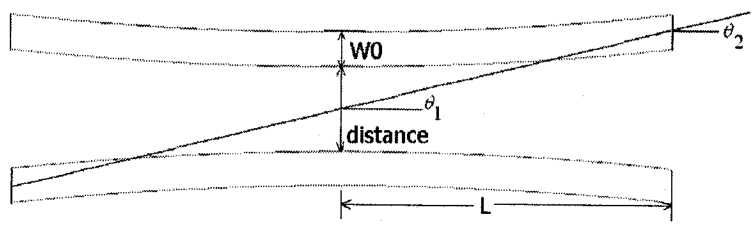

Fig. 4.6.5 Distance, length, and beam waist of the parabola shaped switches

Assume that the device length is L, the device width is W_O, the distance between the two is *dis*, the deflection angle of one channel is θ_2, and the index change is Δn once an E-field is applied. In the parabola deflectors, the deflection angle θ_2 should be equal to the θ_1 in Fig. 4.6.5.

$$\tan(\theta_1) \approx \theta_1 = \frac{1}{L}\left(\frac{\Delta n}{2n_0 W_0}L^2 + \frac{W_0}{2} + \frac{dis}{2}\right) = \frac{\Delta n L}{n_0 W_0} \tag{16}$$

Thus, $$dis_{parabola} = \frac{\Delta n}{n_0 W}L^2 - W \tag{17}$$

Equation (17) indicates that once the width and the length of the device are determined, the distance between two channels can be calculated.

The distance between the two channels is zero if Equation (18) is satisfied. In this case, the deflection angle is given by (19). Usually, in a 500μm thick bulk material with index of 2.2 and index change of 10^{-3}, the angle is around 1.3, which is the minimum angle when distance between the two channels changes.

$$\frac{\Delta n}{n_0 W}L^2 = W \text{ or } L = W\sqrt{\frac{n_0}{\Delta n}} \tag{18}$$

$$\theta = \sqrt{\frac{\Delta n}{n_0}} \tag{19}$$

When distances between the two channels increase, the device length L increases too, as well as the deflection angle as follows,

$$L = \sqrt{\frac{n0}{\Delta n}(W_0 * dis + W_0^2)} > L_{dis=0} = \sqrt{\frac{n0}{\Delta n}} * W_0 \tag{20}$$

$$\theta_1 = \frac{\Delta n L}{n_0 W_0} = \sqrt{\frac{\Delta n}{n_0}(\frac{dis + W_0}{W_0})} > \theta_{dis=0} = \sqrt{\frac{\Delta n}{n_0}} \tag{21}$$

These results indicate that first, the length of the device has to be long enough to obtain a positive distance value as (17) shows. Secondly, the deflection angle and the device length increase (Fig. 4.6.6) when the distance between the two channels increases, which benefits the switch design.

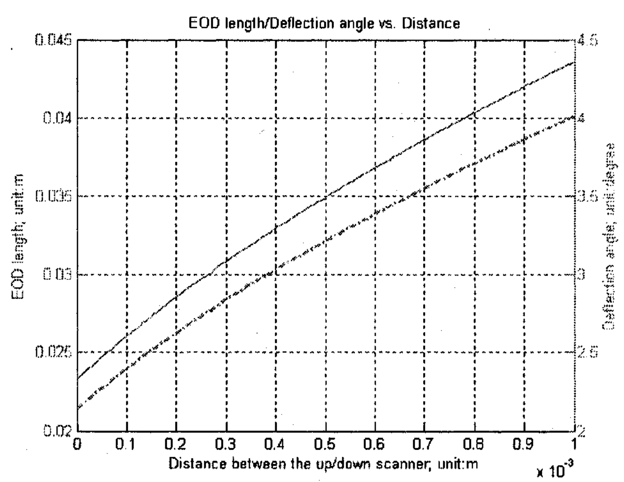

Fig. 4.6.6 EO device length/deflection angle vs. distance

4.6.3 Design of the 2x2 Non-blocking Half-horn Switches

Similar assumptions can be drawn concerning the half-horn shaped switches. Due to the difference of the width in the device, *W(L)* is defined as the width at device length *L*.

$$\tan(\theta_1) = \frac{X(L) + \frac{dis}{2}}{L} = \sqrt{\frac{2\Delta n}{n_0} \ln(\frac{W(L)}{W_0})} \tag{22}$$

Where $W(z)=X(z)+W_0/2$

$$W(L) + \frac{dis}{2} - \frac{W_0}{2} = L * \sqrt{\frac{2\Delta n}{n_0} \ln(\frac{W(L)}{W_0})} \tag{23}$$

$$dis_{half-horn} = 2\left[L * \sqrt{\frac{2\Delta n}{n_0} \ln(\frac{W_L}{W_{L/2}})} - W_L \right] + W_{L/2} \tag{24}$$

Equation (24) calculates the distance between two channels in half-horn shaped devices. The initial width is first determined according to the light beam profile. The minimum length, which ensures a positive distance value, is then decided according to (24). The *dis* is decided once the length *L* is decided. Matlab simulations plot the distance/deflection angle vs. the EO device length as shown in Fig. 4.6.7. The changing length (33 mm), which corresponds to the zero distance of the half-horn design, is longer than the changing length of the parabola design (23.5 mm), proving once again that parabola devices perform better on the deflections.

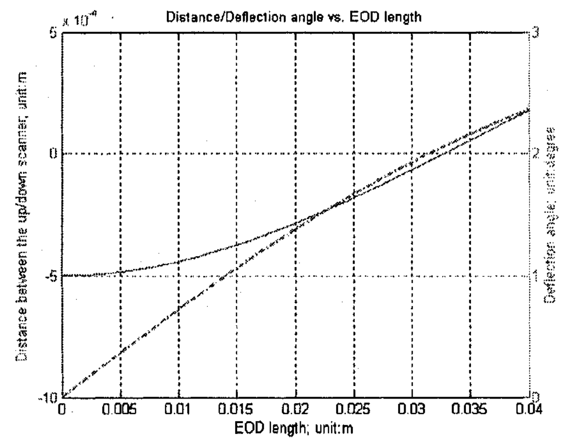

Fig. 4.6.7 Distance/deflection angle vs. EO device length

Although the half-horn shaped devices generally provide smaller deflection angles than their parabolic counterparts, their shape yields well to the implementation of 2x2 devices when considering fabrication. When the distance (*dis*) between the upper and lower channel is zero, as illustrated in Fig. 4.6.3, the prisms in both channels can be joined together without any space between them. Thus, only one poling electrode and one poling procedure are required.

4.7 Test and Experimental Results

Based on the designs of previous sections, devices are fabricated and tested. 500 μm z-cut $LiTaO_3$ single crystal wafers are first poled to obtain the inverted domains with designed patterns. After the deposition of the driving electrodes, the substrates are diced into pieces for tests. A linearly polarized, fiber coupled laser source provides 2 mW of light at 1310 nm wavelength in the testing system. A PM collimator connected to the laser directs the collimated Gaussian beam to the fabricated devices. The Gaussian beam has a 400μm beam waist and a 100 mm working distance; its beam waist is located 40 mm from the collimator. An IR camera or another collimator is employed to detect the outgoing beams from the EO devices. When a 1000V voltage is applied, the light beam bends up and when no voltage is applied, the light beam travels straight. The camera captures the two output spots, or the receiving collimator detects the output power. The deflection angles of each channel are then measured.

Two types of devices were fabricated and tested. The first type consists of devices with new parabolic and half-horn geometries. The second consists of deflectors based on these new geometries as shown in Section 4.5.1 and Section 4.5.2. Table 4.7.1 defines the devices tested, indicating their dimensions and theoretical values of deflection angles. In the table, the width refers to the entrance width in the half-horn configurations, or the uniform width in the parabola configurations, or the minimum width in the half-horn deflector, or the uniform width in the parabola deflector. The distance means the distance between the upper deflector and lower deflector in the two incident lights deflectors as introduced in Section 4.5.3. The devices H1 and H2 have the configuration shown in Fig. 4.4.7; devices P1 and P2 have the configuration shown in Fig. 4.4.2; devices DH1, DH2, DH3, and DH4 have the envelope shown in Fig. 4.6.3 (a); and devices DP1, DP2, DP3, and DP4 have the envelope shown in Fig. 4.6.3 (b).

Table 4.7.1 Fabricated and tested devices

name	Description	Dimension Width (μm)	Length (mm)	Distance (mm)	Theoretical deflection angle
New Geometries					
Half-horn, H1	1x2 deflector	450	40.1 mm	NA	2.45
Half-horn, H2	1x2 deflector	500	39.3	NA	2.3
Parabola, P1	1x2 deflector	450	38.6	NA	3.09
Parabola, P2	1x2 deflector	500	41.8	NA	3.01
Deflectors					
Half-horn, DH1	2x2 switch	550	66	1.09	1.89
Half-horn, DH2	2x2 switch	500	60	1	1.89
Half-horn, DH3	2x2 switch	500	52	0.66	1.68
Half-horn, DH4	2x2 switch	450	48	0.643	1.72
Parabola, DP1	2x2 switch	500	50	0.72	1.49
Parabola, DP2	2x2 switch	450	56	1.25	1.81
Parabola, DP3	2x2 switch	500	60	1.25	2.17
Parabola, DP4	2x2 switch	550	64	1.26	2.1

4.7.1 New Geometries Test

The performance of new geometries, half-horn and parabola, are first measured using the setup illustrated in Fig. 4.7.1.

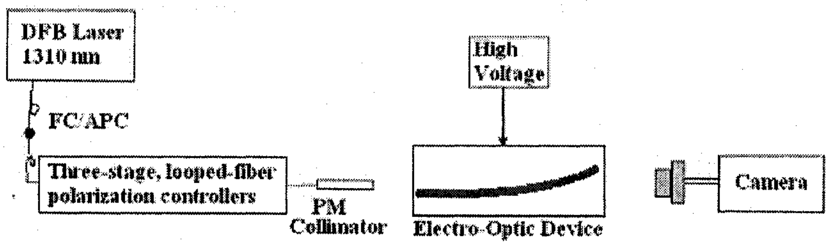

Fig. 4.7.1 Setup of the deflection angle of the parabola or half-horn 1x2 deflectors

In this test, the EO devices are placed or aligned parallel to the input collimator to ensure a horizontal incident light. The three-stage, looped-fiber polarization controllers are employed here to precisely control the polarization of the incident beam. The applied high voltage is 1 kV. The camera captures two beam spots. The deflection angle of the devices can be calculated as follows, and the total distance is shown in Fig. 4.7.2.

$$\text{the deflection angle} = \frac{\text{the distance between the two spots in the camera}}{\text{the distance from the device end to camera}}$$

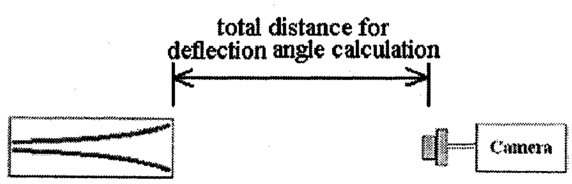

Fig. 4.7.2 Total distance for the deflection angle calculation

Devices with different dimensions are tested and their deflection angles are listed in Table 4.7.2. Fig. 4.7.3 illustrates captured spots of device P1.

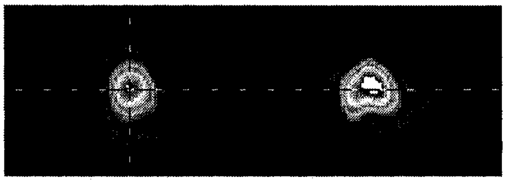

Fig. 4.7.3 Two output beams for the Parabola geometry (P1) with 38.6mm long and 450μm wide.

Table 4.7.2 Theoretical and Measured deflection angles

Shape	Mark	Length x Width (mm) x (μm)	Theoretical Deflection angle	Measured Deflection angle
Parabola	P2	41.8 x 500	2.24°	3.01°
	P1	38.6 x 450	2.74°	3.09°
Half-Horn	H1	40.1 x 450	2.45°	2.45°
	H2	39.3 x 500	2.2°	2.3°
Rectangular		40 x 612	NA	1.18°

From Table 4.7.2, compared with the deflection performance of the rectangular (1.18°) deflectors, these two new configurations provide a steering improvement factor of approximately 2 to 3.

4.7.2 Deflector Test

Deflectors based on new geometries were also fabricated and tested using a setup similar to the one used in the previous test and illustrated in Fig. 4.7.4.

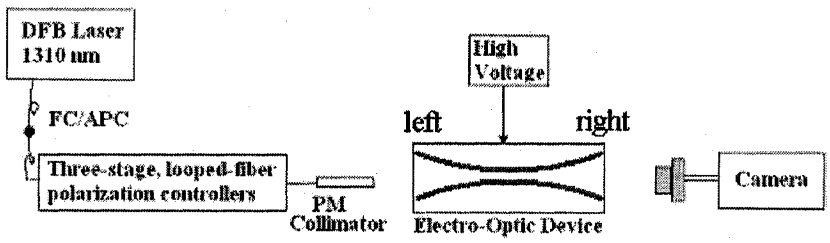

Fig. 4.7.4 Deflection angle and switch test of the devices

The deflectors are fabricated with envelopes shown in Fig. 4.7.5. Two symmetric deflectors, upper and lower ones, are fabricated in one device with some distances in between. In this way, two channels can be tested together and the potential 2x2 EO switches can be proved.

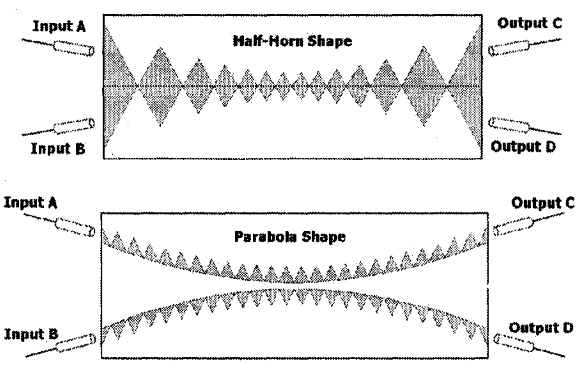

Fig. 4.7.5 Schematic of the deflectors

According to the design, the input collimators are strictly aligned tangent to the trajectory curve at the point of the incidence and are thus positioned at fixed angles with respect to the input facet of the crystal. Suppose that the light is captured as output spot *C*, when a 1kV voltage is applied; and that the light is captured as the output spot D, when there is no external field. Two output spots, C and D, from incident beam A or B of the half-horn device can be captured by an IR camera. The deflection angles are calculated from the distance measurements of these two output spots when the light beam is launched from A or B as follows,

$$\text{deflection angle} = \frac{\text{the distance between the two spots in the camera}}{\text{the distance from the device end to camera + half of the EOD length}}$$

Where, the total distance in the denominator is shown in Fig. 4.7.6.

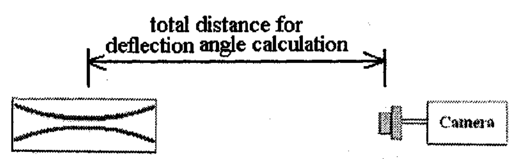

Fig. 4.7.6 Total distance in the deflection angle calculation

Instead of the rotated input collimators, the experiments show that if the light is aimed horizontally at the center of the devices as Fig. 4.7.7 shows, the output spots are distorted. Unlike the rectangular shapes, where the incident light is perpendicular to the interface, the nonrectangular shapes establish an interface which is almost parallel to the incident horizontal light. At that small angle between the incident light and the interface, total internal reflection (TIR) occurs, and the output is distorted.

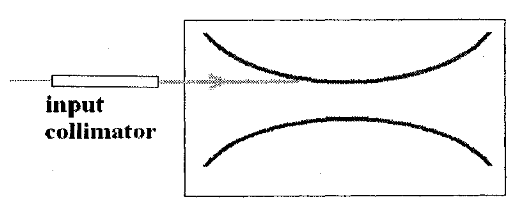

Fig. 4.7.7 Input light beam parallel to the center of the devices

Assuming that the light travels from media with an index n_1 to media with an index n_2 and $n_1 > n_2$, the incident angle in the interface is θ_i, which is equal to 90° (the angle between the incident light and the interface), as per [3]. The reflection of the total light is $R = [(n_2 \cos\theta_i - n_1 \cos\theta_t)/(n_2 \cos\theta_i + n_1 \cos\theta_t)]^2$ and the transmission of the total light is $T = 1 - R$. According to Shell's law, TIR happens when $n_2 \sin\theta_t = n_1 \sin\theta_i$, that is at $\theta_t \approx 89.0°$. From these calculations, when the incident horizontal light is parallel to the interfaces of the devices, more and more light is reflected and less and less light is transmitted. After reaching the TIR angle, no light is transmitted in the nonrectangular shaped devices, which explains the experimental phenomenon.

The incident light is launched into the device with a small rotation angle and the distances of the two output spots change according to the rotation angle of the incident light, as Fig. 4.7.8 and Fig. 4.7.9 show. The distance of the two spots achieves its maximum when the rotation angle of the incident light matches the deflection angle.

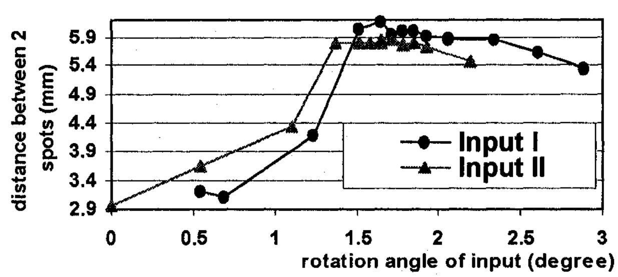

Fig. 4.7.8 Distance between the two output spots vs. rotation angle of the input in the half-horn

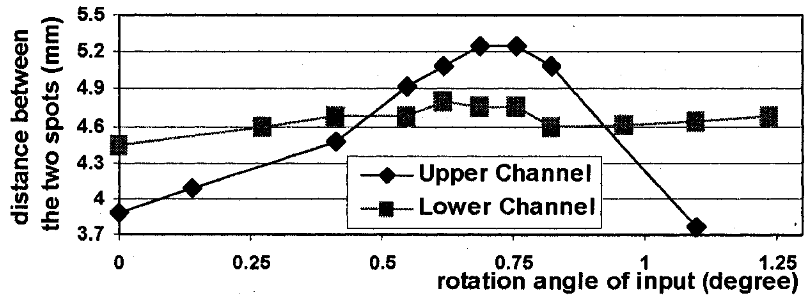

deflector

Fig. 4.7.9 Distances between the two output spots vs. rotation angle of the input in the parabola deflector

The output spots from two channels are captured separately. The locations of the spots are reported in each channel when the camera is fixed on the same place. By comparing the locations of spots from different channels, the functionality of the 2x2 switch can be assessed. The captured two spots are shown in Fig. 4.7.10, Fig. 4.7.11, and Fig. 4.7.12.

Two spots from upper channel, Spot 1 is on the left; Spot 2 is on the right.

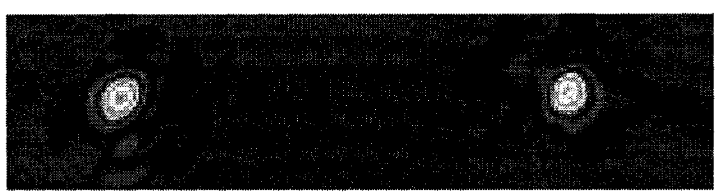

Two spots from bottom channel, Spot 1 is on the left; Spot 2 is on the right.

Fig. 4.7.10 Locations of the output spots of the 2x2 half-horn switch (DH1)

Fig. 4.7.11 Two output spots of the 2x2 parabola switch for the upper channel

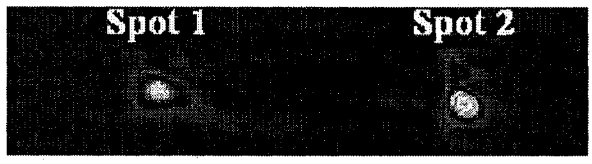

Fig. 4.7.12 Two output spots of the 2x2 parabola (DP4) switch for the lower channel

The calculated deflection angles from measurements of different shaped deflectors are listed in Table 4.7.3. It shows the deflection angle in the upper channel and the lower channel for parabola shaped and half-horn shaped switches, respectively. The deflection angles are very large compared to those produced by usual rectangular devices [10]. The experimentally measured angles are the largest angles of deflector ever reported on bulk EO deflectors. The difference between the experimental results and the simulation is due to the undesired change of the material refraction index after the electric field poling. The poling process, which is essential to the domain inversion, causes some permanent change of index within the area of polling. These effects will be discussed in the next chapter.

Table 4.7.3 Theoretical deflection angles and the test results of the 2x2 switch

Half-Horn shaped 2x2 switch	Theoretical Value	Test result
The deflection angle of the Half-Horn deflector (450μm for the entrance width; 24mm long)	1.72°	1.5°
The deflection angle for input I	3.44°	3.2°

The deflection angle for input II	3.44°	3.0°
Parabola shaped 2x2 switch		
The deflection angle of the Parabola deflector (550μm wide; 32mm long)	2 °	1.6°
The deflection angle for upper channel	4°	3.1°
The deflection angle for lower channel	4°	2.9°

Table 4.7.4 Insertion Loss and Crosstalk of the EO deflectors; tested by camera

Shape	Length x Width (mm x μm)	Locations	Insertion Loss (dB)	Crosstalk (dB)
Half-horn	66 x 550	Upper; Spot1	4.39	10
Half-horn	66 x 550	Upper; Spot2	3.75	21
Half-horn	66 x 550	Lower; Spot1	3.57	12
Half-horn	66 x 550	Lower; Spot2	3.28	28
Parabola	64 x 550	Upper; Spot1	2.87	14
Parabola	64 x 550	Upper; Spot2	2.42	17
Parabola	64 x 550	Lower; Spot1	2.45	19
Parabola	64 x 550	Lower; Spot2	2.57	7

The insertion losses of the devices are first measured using the Sensors Unlimited InGaAs camera, which has high linearity in the infrared spectrum. The camera is first calibrated to the apertured optical beam (to represent the aperture of the receiving collimator) without passing through the EO deflectors. And this power will serve as the reference for the remaining measurements. Then the different devices are inserted into the optical set-up, aligned, and the powers of the optical beam with the same aperture are recorded as the insertion losses. Table 4.7.4 list the insertion loss of the Half-horn and Parabola devices. Since the facets of the deflector were not antireflection coated, the loss thus caused was calculated and removed from the results.

To measure the crosstalk through the camera, the extrapolated aperture is used once again. The aperture is first placed to a best-fit location over the beam spot on the camera, the device is then switched to another state, and the power in the aperture is measured. To make this measurement, the beam is half blocked with a razor blade, and the attenuation of the input beam is decreasing until the power within the aperture is measured the same as previous insertion loss on the same state. The attenuation is then taken as the crosstalk as shown in Table 4.7.4.

Table 4.7.5 Insertion Loss and Crosstalk of the EO deflector; tested by collimator

Device (DH1)	Length x Width (mm x μm)	Locations	Insertion Loss (dB)	Crosstalk (dB)
Half-horn	66 x 550	Upper; Spot1	4.42	>41
Half-horn	66 x 550	Upper; Spot2	5.02	>42
Half-horn	66 x 550	Lower; Spot1	4.98	>41
Half-horn	66 x 550	Lower; Spot2	8.8	>34

These crosstalk tested by camera are not very accurate due to the way of measurement. Receiving collimators are then introduced at the outputs to detect powers. The collimator is first aligned to the one output of the each channel, the device is then switched to another state, and the measured power difference in the same location of receiving collimator is recorded as the crosstalk. Table 4.7.5 shows the measured insertion loss and crosstalk from fiber collimator to fiber collimator on the Half-horn device (DH1). The loss caused by the non-antireflection coated facets of the deflector was calculated and removed from the results.

4.8 Conclusion and Future Work

In this chapter, the previous equivalent theory is now expanded from rectangular shapes to all kind of shapes. Simulation in Code V and BPM, as well as the experimental results in this chapter and Chapter 5 all proved that the theory does work and is useful in the design and analysis. A novel merit factor, the deflection performance indicator, is proposed in Section 4.3, to compare different EO deflectors. Comparison of different shaped devices is given in Section 4.5.

Two new geometries are proposed in this chapter, which are a better fit for optical switching applications. These geometries follow a parabolic and half-horn shape. Their performances are compared to existing devices by the deflection performance indicator in both simulation and experiments.

Based on the new non-rectangular geometries, two novel EO deflectors were designed and built. The average deflection angles are 3.0 ° and 3.1° for the parabola and half-horn shaped 2x2 switches, respectively. Based on that, non-blocking 2x2 optical switches were designed and tested for the first time. 2x2 switching functionality was achieved in free space test in the lab and the switches exhibited large deflection angles and easy fabrication.

In the future, steps will be taken to improve the deflection angle of the switches. The EO devices will be optically polished on the left and right edges, which are the interfaces for the input and output light beams. Research and experimental work will take into account the poling theories to obtain better domain walls. High-speed tests will be conducted on the future EO devices to measure their switching time.

The packaging of the 2x2 optical switches will also be improved in the future. Using the same inner and outer package, as well as the same PM collimators, and electrical connectors, the packaged 2x2 optical switches will be demonstrated. The performance of the packaged devices, such as insertion loss, crosstalk, and channel-to-channel speed will be measured. Fig. 4.8.1 shows the 3D model of the future packaged 2x2 optical switch. There won't be any additional optical components in the package to further separate the beams due to the larger deflection angles provided by the new shaped deflectors.

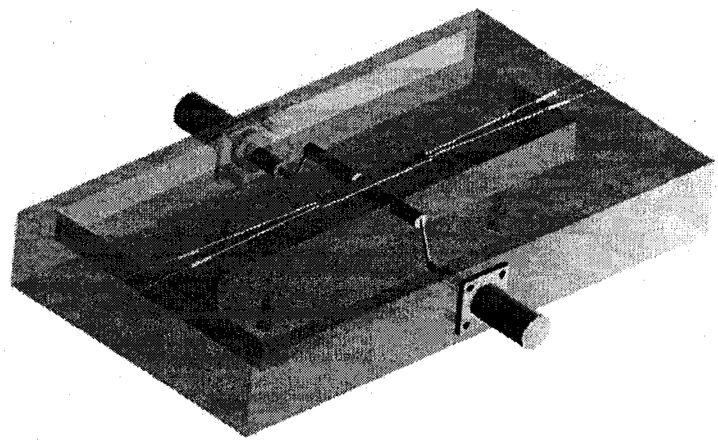

Fig. 4.8.1 3D model of the packaged 2x2 optical switch

4.9 References

[1] J. F. Lotspeich, "Electrooptic light-beam deflection," *IEEE Spectrum*, pp. 45–52, 1968.

[2] Y. Chiu, J. Zou, D. D. Stancil, and T.E. Schlesinger, "Shape-Optimized Electrooptic Beam scanners: Analysis, Design, and Simulation," *Journal of Lightwave Technology*, Vol. 17, No. 1, pp. 108-114, 1999.

[3] Y. Zuo, M. Mony, B. Bahamin, V. Aimez, and D.V. Plant, "Bulk Electro-Optic Deflector Based Switches," *Applied Optics*, Submitted, Dec., 2006.

[4] E. L. Wooten, K. M. Kissa, A. Yi-Yan, E. J. Murphy, D. A. Lafaw, P. F. Hallemeier, D. Maack, D. V. Attanasio, D. J. Fritz, G. J. McBrien, and D. E. Bossi, "A Review of Lithium Niobate Modulators for Fiber-Optic Communications Systems," IEEE Journal of Selected Topics in Quantum Electronics, Vol. 6, No. 1, pp. 69-82, 2000.

[5] S. Zhu, Y. Zhu, Z. Zhang, H. Shu, H. Wang, and N. Ming, "$LiTaO_3$ crystal periodically poled by applying an external pulsed field," *Journal of Applied Physics*, Vol. 77, pp. 5481-5483, 1995.

[6] Q. Chen, Y. Chiu, D. N. Lambeth, T. E. Schlesinger, and D. D. Stancil, "Guided-Wave Electro-Optic Beam Deflector Using Domain Reversal in $LiTaO_3$," *Journal of Lightwave Technology*, Vol. 12, No. 8, pp. 1401-1404, 1994.

[7] J. Li, H. C. Cheng, M. J. Kawas, D. N. Lambeth, T. E. Schlesinger, and Daniel D. Stancil, "Electrooptic wafer beam deflector in $LiTaO_3$s," *Journal of Lightwave Technology*, Vol. 8, No. 11, pp. 1486-1488, 1996.

[8] J. F. Lotspeich, "Electrooptic light-beam deflection," *IEEE Spectrum*, Vol. 5, pp. 45–52, 1968.

[9] J. C. Fang, M. J. Kawas, J. Zou, V. Gopalan, T.E. Schlesinger, and D. D. Stancil,

"Shape-Optimized Electrooptic Beam scanners: Experiment," *Photonics Technology Letters, IEEE*, Vol. 11, No. 1, pp. 66-68, 1999.

[10] Y. Zuo, B. Bahamin, P. Langlois, V. Aimez, D. V. Plant, "Packaging and Performance of an Ultra-Fast 1x4 Optical Switch," In *Conf. Lasers and Electro-Optics*, Baltimore, MA, USA, 2005, CTuW2.

Chapter 5: Optical Switches: 1x2 and 1x4

5.1 Introduction

EO beam deflectors have been described in Chapter 2 and Chapter 4. Here, two packaged optical switches, 1x2 and 1x4 electro-optical switches, are introduced as applications of those EO deflectors. These EO switches feature high-speed and low-loss and are aimed at future agile all-photonic networks.

These optical switches are built from rectangular shaped EO deflectors. The $LiTaO_3$ crystals have been poled to obtain domain inversions as discussed in Chapter 3. By applying an electrical field through the driving electrodes across the crystal, the trajectory of the beam is diverted as it travels through the poled wafer. The electric field induces an index change of an opposite sign in the adjacent domain regions in the EO device, causing the optical beam to refract at the interfaces. The choice of whether to apply an E-field or not determines the path on which a light beam travels. Thus, the optical switch is created. By combining these EO deflectors with fiber collimators and high voltage packaging, high-speed optical switches are built and characterized [1].

The remainder of this chapter is organized as follows: Section 5.2 briefly describes the design of the 1x2 and 1x4 optical switches. Section 5.3 describes the testing of the EO elements. Section 5.4 provides details regarding the packaging and section 5.5 focuses on optical and high-speed testing of the 1x2 and 1x4 switches. And section 5.6 presents the conclusion.

5.2 Design and Simulation

Previously, Chapter 2 and Chapter 4 described various shapes of EO deflectors. The present chapter describes how the optical switch is built using rectangular shaped EO deflectors. By controlling the external electrical field on the EO deflector, the optical beam changes its path, and thus optical switches are made.

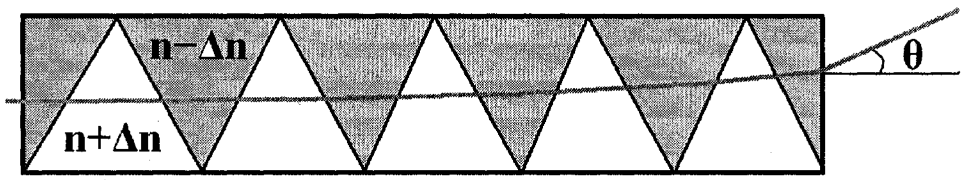

Fig. 5.2.1 Two domains in the rectangular shaped 1x2 EO switch

The 1x2 EO switch has two domains as shown in Fig. 5.2.1. According to Chapter 2, the index change is given by equation (1) and the deflection angle inside the substrate is given by equation (2):

$$n_{\pm} = n_0 + \frac{n_0^3}{2} r_{33} \frac{V}{D} \tag{1}$$

$$\theta = n_0^2 r_{33} \frac{V}{D} \frac{L}{W} \tag{2}$$

Here, n_0 is the index of refraction (=2.18), r_{33} is the electro-optic coefficient of the substrate along the z-axis (=30.5 pm/V), V is the external voltage, D is the thickness of the substrate, L is the device length, and W is the device width.

By choosing the appropriate L and W, optical switching can be obtained. The dimensions of individual prisms and the number of prisms do not affect the deflection performance, since only the overall dimensions of the deflector are relevant, as per [2].

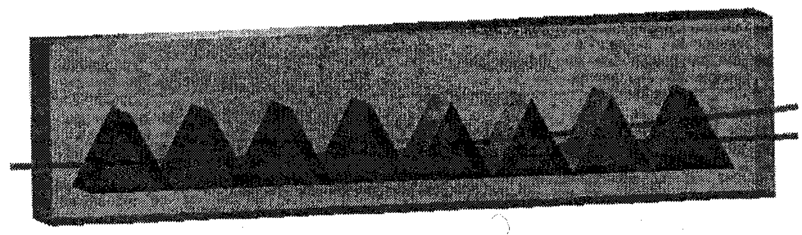

Fig. 5.2.2 Three-D model of the 1x2 optical switch

Using these concepts, the 1×2 optical switch is designed as shown in Fig. 5.2.2. The conceived deflector has an effective length of 18.5 mm and a width of 0.57 mm.

Subsequently, a 1×4 optical switch also can be created using a cascade of two 1×2 switches on a contiguous substrate as shown in Fig. 5.2.3. The first stage operates in a manner similar to that of the 1×2 switch, whereas the second stage is designed to be wide enough to deflect both the original and deflected beams fed by the first stage. Using this approach, four states can be obtained depending on the configuration of the electric field applied to the EO device. The four output spots or the four channels are labeled as follows: 00, 01, 10, and 11. Using this notation, 00 indicates that no voltage is applied to either stage; 01 indicates that a voltage is applied only to the second stage; 10 indicates that a voltage is applied only to the first stage; and 11 indicates that a voltage is applied to both stages simultaneously. Accordingly, the four receivers are labeled as 00, 01, 10 and 11 collimators.

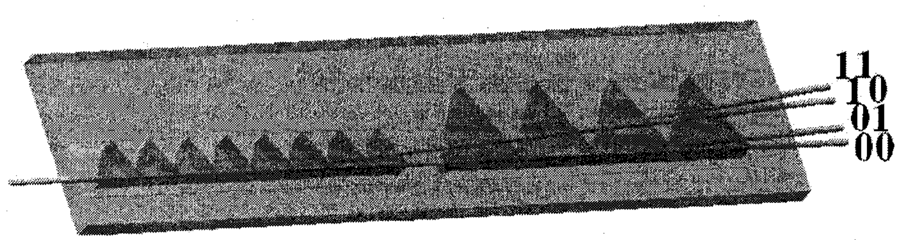

Fig. 5.2.3 Cascaded structure of 1x2 optical switch

To achieve the 1x4 switch, the length and width of the first and second stages have to be optimized to get the largest and yet similar separation between the four outgoing beams. Also, the total length of the device is confined by the wafer diameter

(6 inches). Assuming that the length and width of the first and second stages are *L1* and *L2*, *W1* and *W2*, respectively, they satisfy:

$$\begin{cases} \theta_1 = n_0^2 r_{33} E \dfrac{L_1}{W_1} \\ \theta_2 = n_0^2 r_{33} E \dfrac{L_2}{W_2} \\ \theta_3 = n_0^2 r_{33} E (\dfrac{L_1}{W_1} + \dfrac{L_2}{W_2}) \end{cases} \tag{3}$$

$$\text{And} \begin{cases} \theta_2 \approx 2\theta_1 \\ \theta_3 \approx 3\theta_1 \\ L_1 + L_2 < 76.2 \\ W_2 \geq W_1 + D \end{cases} \tag{4}$$

where D is the deflected distance at the first stage (unit: mm).

Matlab programs were written to find the optimal *L1*, *L2*, *W1*, and *W2*. A graphical user interface was created for the designer convenience to modify the wavelength, index, and property of the EO material, or the PM collimators. After programmed calculation, the *L1*, *L2*, *W1*, and *W2* were chosen; and the final dimensions of the two active regions were determined to be 21.9 mm×0.6 mm and 15.5 mm×0.8 mm, respectively. The fabricated 1x4 switch is shown in Fig. 5.2.4. The simulated beam transmission and outgoing beam spots are shown in Fig. 5.2.5.

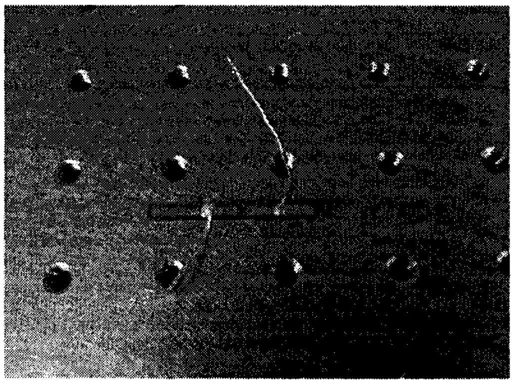

Fig. 5.2.4 1x4 EO deflector with wires

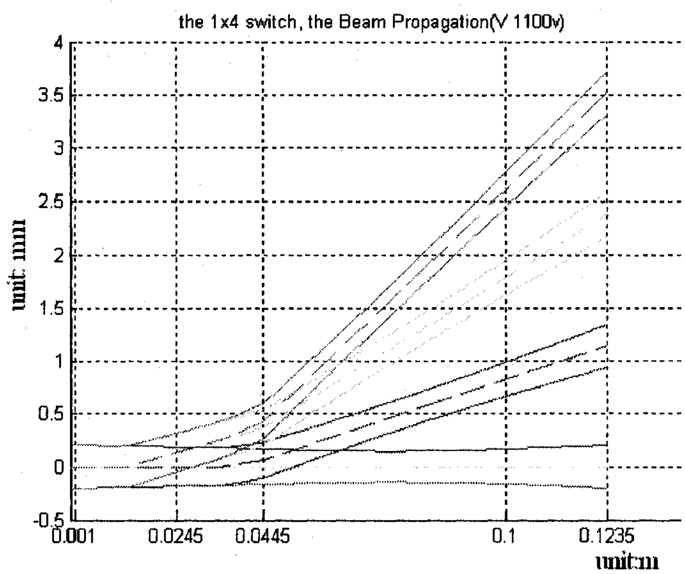

(a)

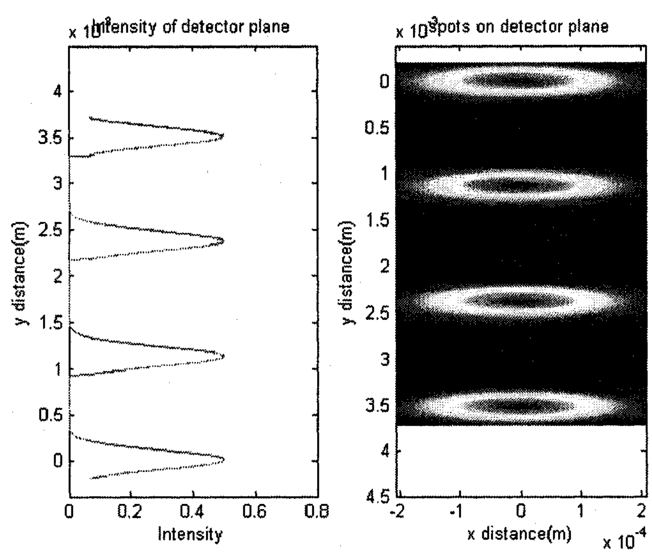

(b)

Fig. 5.2.5 Matlab simulation results. (a) beam deviation of the 1x4 switch; (b) deviation of the four beams (note: the scale of the x and y axes are different).

5.3 Free Space Test

This section describes the tests that were performed to verify the switching designs. Other features of the EO switches are also demonstrated.

5.3.1 Testing the Deflection Angle

In Fig. 5.2.4 of last section, the two stages of the 1x4 switch device are shown. Wires are soldered to each stage to connect to the external voltage (which in turn will generate the necessary E-field). When only considering the first stage, a 1x2 switch is obtained.

The first test focuses on the deflection performance of the 1x2 and 1x4 switches. Fig. 5.3.1 shows the setup for the free space test, and Fig. 5.3.2 is a photo of the main setup. PM fiber collimators are used to launch the TM linear polarized light into the device. The voltage is applied through a spring probe that touches the surface of the devices. On the receiving end, a sensitive IR camera serves as the receiver to capture the output spots.

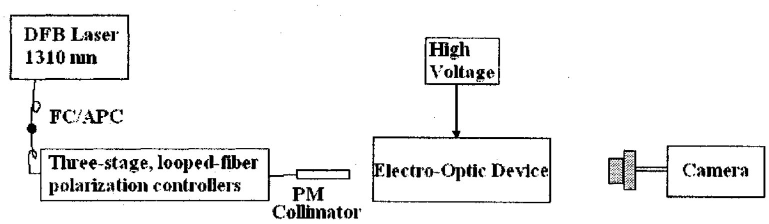

Fig. 5.3.1 Schematic setup for the free space test

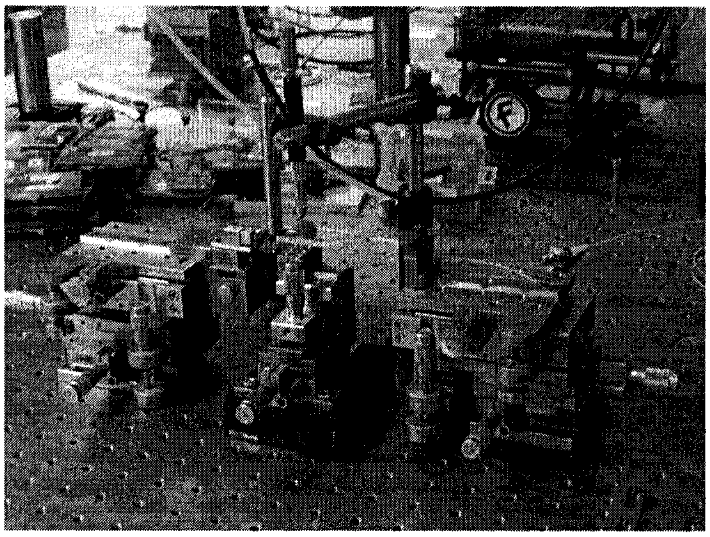

Fig. 5.3.2 Test setup in lab

The distances between the output spots on the camera are recorded and used to calculate the deflection angle as follows:

$$\tan\theta = \frac{\text{Beam distance between the stage 0 to the target stage}}{\text{total distance from the end of the device to the camera}} \tag{5}$$

Since θ is usually smaller than 5°, $\theta \approx \tan\theta$

The two spots captured under 1200 V of the 1×2 optical switch are shown in Fig. 5.3.3. Fig. 5.3.4 plots the deflection angle vs. voltage and also the theoretical values (dots in the figures) of the angle. All these experimental results verified the original design parameters shown in Section 5.2.

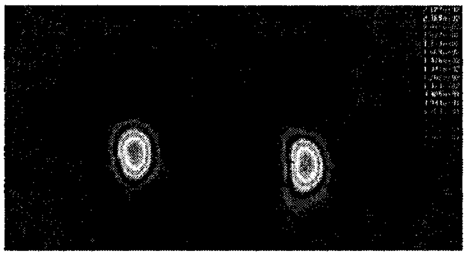

Fig. 5.3.3 Two spots of the 1x2 optical switch captured at 1200 V

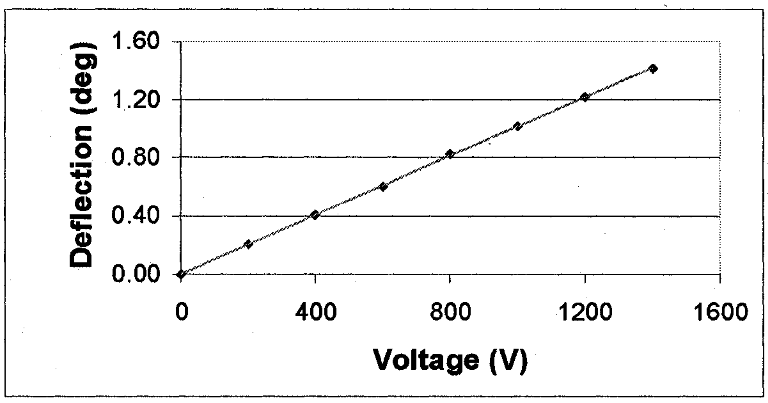

Fig. 5.3.4 Deflection angle vs. voltage in the 1x2 optical switch. Solid line: experimental results; Dots: theoretical value.

The same setup as the 1x2 switch is used to test the deflection performance of the 1x4 EO switch. When testing stage 11, the two wires shown in Fig. 5.2.4 connect together and apply voltage. The four output spots are illustrated in Fig. 5.3.5. Fig. 5.3.6 and Fig. 5.3.7 plot the four spots locations on the camera vs. voltage and the angle vs. voltage. The experimental and theoretical values for stage 01 and 10 match better than stage 11 because the latter has a more complicated structure.

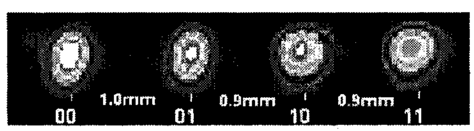

Fig. 5.3.5 Four spots of the 1x4 optical switch

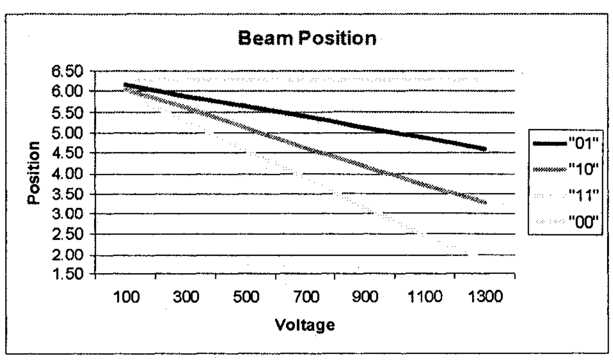

Fig. 5.3.6 Spots locations on camera vs. voltage for all channels in the 1x4 switch

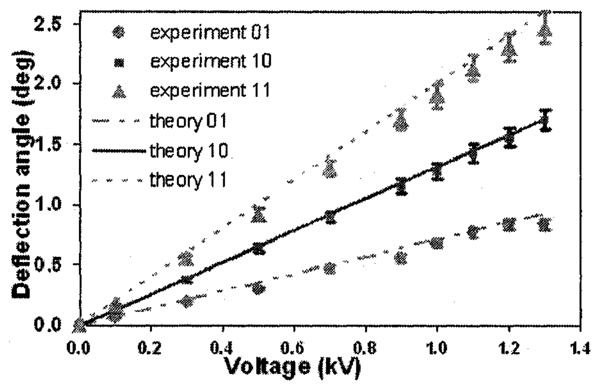

Fig. 5.3.7 Theoretical and experimental results for the deflection angle vs. voltage

5.3.2 Polarization Test Results

These EO switches are polarization dependent due to the property of the EO material and the misalignment of the polarization angle which dramatically affects the performance of the optical switches. In this section, the effect of polarization misalignment is quantified by the insertion loss and crosstalk. By analyzing these results, which we do in the next section, we acquire a better understanding of the mechanism of the polarization dependence of the EO switches.

To obtain a larger deflection angle, a larger index change is required. According to chapter 2, the index change in the z-axis is much larger than those in the x and y coordinates since r_{33} is three times r_{13},. Thus, a linear light source with an electrical field parallel to the z-axis should be utilized and the polarization angle is set at zero in this situation. Any divergence of the incident light with the polarization angle will cause a portion of the light power to propagate in the x-axis and decrease the power in the z-axis. Due to the different index changes in the x and z axis, the light power is deflected differently, which in the end, introduces a loss in the corresponding receivers.

To better describe this dependency, the insertion loss and crosstalk was tested for the 1x4 optical switches under 1.1 kV driving voltage when the polarization is rotated away from the z-direction (vertical polarization) of the crystal. The polarization test setup was as follows:

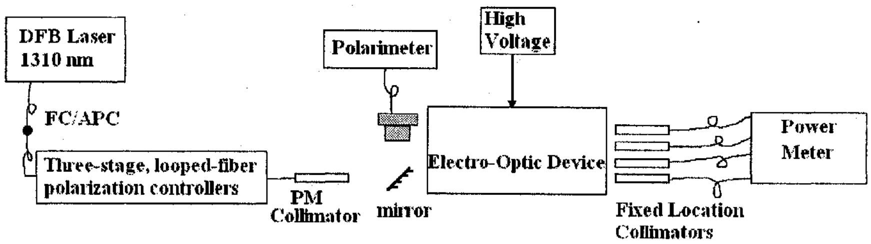

Fig. 5.3.8 Schematic setup for the polarization test

First, the four output collimators are aligned to the exact receiving locations with minimum loss, and are fixed there. The three-stage looped-fiber polarization controller is connected between the light source and the incident fiber to modify the polarization angle. A removable mirror is placed in front of the EO switches to reflect the incident light to the polarimeter, which is the equipment used to test the properties of the polarizations. Once a polarization angle is set, the mirror is removed, and high voltages are applied to the EO device. All the readings from the power meters of the four collimators are recorded. By controlling the voltages applied to the two stages, the readings represent the insertion loss or crosstalk for each channel. For example, when no E-field is applied to either of the stages, the readings describe the insertion loss for channel 00, and crosstalk for channels 01, 10, and 11. Table 5.3.1 and 5.3.2 demonstrate the polarization extinction ratios when the polarization angle is 0° and 5°. Similar data are obtained for other angles as 10°, 15°, 20°, 30°, 45°, 60°, and 90°.

Table 5.3.1 Power meter reading of all channels and all voltage settings with 0° polarization angle (the values in blue represent the insertion loss)

Polarization Angle is 0°				
PER (dB)	"00"	"01"	"10"	"11"
"00"	3.8	27	32	38.7
"01"	42.1	4.1	32.8	39.6
"10"	42.8	39.4	4.2	34.1
"11"	42.4	42.4	41.3	4.5

Table 5.3.2 Power meter reading of all channels and all voltage settings with 5° polarization angle (the values in blue represent the insertion loss)

Polarization Angle is 5°				
PER (dB)	"00"	"01"	"10"	"11"
"00"	3.8	17.5	25.3	35.6
"01"	41.7	4.6	31.8	34.1
"10"	42.2	41.4	4.4	33.9
"11"	42.4	42.4	41.3	4.6

Considering the total insertion loss and crosstalk for different polarization angles, plots of the polarization performance can be drawn in relation to the different channels from these testing results. These results will be described in the next section.

5.3.3 Analysis of Polarization Test

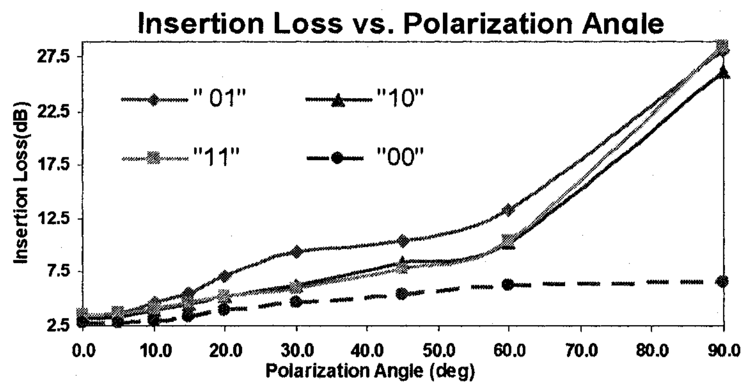

Fig. 5.3.9 Insertion loss vs. polarization angle of all channels

It is reasonable to assume that the insertion loss increases when the polarization angle increases. Chapter 3 states that the index on the z-axis is n_e and the other two indices along x and y coordinates are n_0. When the incident light has a polarization direction parallel to the z-axis, or the polarization angle is 0°, the power of light propagates on the z-axis, and the EO effect is best utilized. This explains why in Fig. 5.3.9 the insertion losses for all four channels at 0° have minimum values. When the polarization is rotated away from the z-axis, the polarization angles increase and the power of light on the z-axis decreases, while the power on the x-axis increases. Thus, the insertion losses of channel 01, 10, and 11 increase as shown in Fig. 5.3.9. Assuming that the polarization angle is θ_p, the power of light on the z-axis and x-axis as shown in Fig. 5.3.10 can be expressed as:

$$P_z = \cos^2 \theta_p \qquad\qquad P_x = \sin^2 \theta_p \tag{6}$$

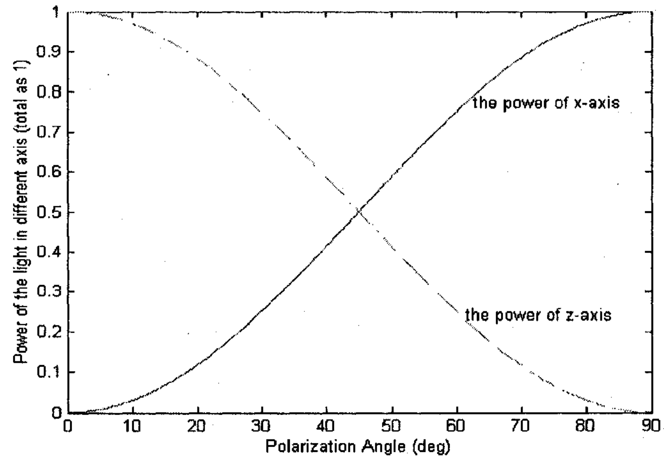

Fig. 5.3.10 Light power in x-axis and z-axis vs. polarization angle

At the extreme case of θ_p = 90°, all the light power propagates on the x-axis. Without any external field, the EO device works as a polarizer and only part of the light can pass (loss would be 7dB as shown in Fig. 5.3.10). With an external E-field, besides the 7 dB loss, other losses occur.

According to chapter 3, n_O (x-axis) is smaller than n_e (z-axis); r_{13} is one third of r_{33}; the index change of Δn_e is proportional to n_e as $\Delta\theta_e \propto n_e^2 r_{33}$; the index change of Δn_O is $\Delta\theta_o \propto n_o^2 r_{13}$; and $\Delta\theta_o \approx \Delta\theta_e / 3.65$. The total power can be divided to P_z and P_x, and the deflection distance can be described as D_z and D_x where D_z or D_x are the deflection distances of the light with power only on the x-axis or the z-axis. When the E-field is applied to the EO devices, D_x = 0.274.

Due to the fixing of the receiving collimators, the different deflection distances D_z and D_x introduce additional losses to the insertion loss and crosstalk. The schematic of the beam diameter, collimator diameter, and spots location is shown in Fig. 5.3.11:

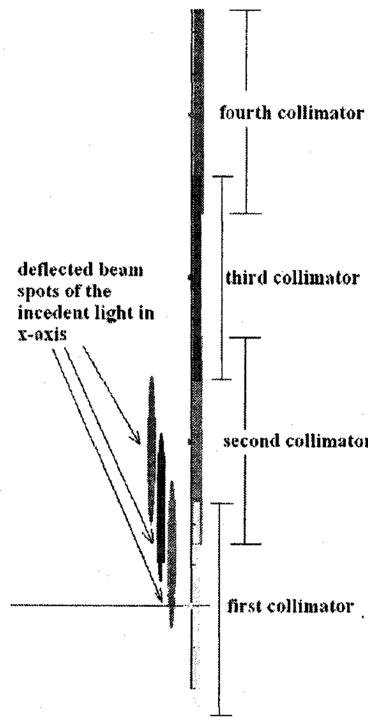

Fig. 5.3.11 Locations and diameters of the output beams and collimators

The distances between all fixed collimators are around 1.1 mm, and the beam waist is 0.5 mm. As Fig. 5.3.11 shows, the beams deflected by Δn_o overlap. Also the 01, 10, and 11 collimators can detect nothing or very little power of the light deflected by Δn_o. Since the power on the z-axis is weaker when the polarization angle increases, the insertion losses of these channels increase. At the polarization angle θ_z, the valid power which can be detected by the collimators is $cos^2\theta_z$, as shown in Fig. 5.3.10. These plots of power match the insertion losses shown in Fig. 5.3.9. In conclusion, the insertion losses in each channel (except channel 00) decrease dramatically.

The crosstalk on different channels also depends on the polarization. For example, a reading of the power of the 00 collimator not only includes the power of the 00 channel but also the light power deflected by Δn_o from the 01, 10, and 11 channels as shown in Fig. 5.3.12. Expressed in equations, the power in x-axis and z-axis are:

$$P_z = \cos^2\theta_p \quad P_x = \sin^2\theta_p \;; \quad \text{and} \quad D_x = 0.274\, D_z \qquad (7)$$

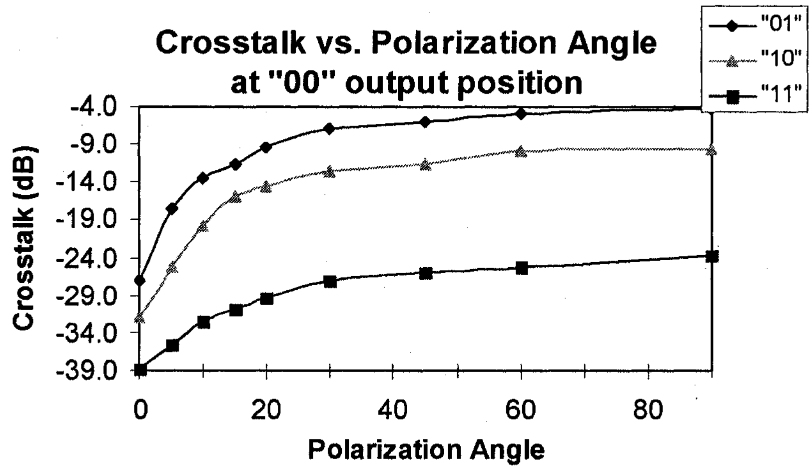

Fig. 5.3.12 Crosstalk vs. polarization angle at the 00 output position

If the voltage is only applied on the second stage, ideally, the power will be received by collimator 01. However, since only $\cos^2\theta_z$ of the whole power remains on the z-axis, the other $\sin^2\theta_z$ of the total power will also be deflected and the deviated length is D_x:

$D_x = 0.274\, D_z = 0.274 * 1.1 = 0.30$ mm

Considering the beam diameter (1.0 mm) and the collimator diameter (1.4 mm), almost all the light deflected by Δn_o is detected by collimator 00 instead of collimator 01. The larger the polarization angle, the more power is detected by collimator 00 as crosstalk. When the polarization angle is 90°, the crosstalk in channel 00 reaches its highest level, which is comparable to the insertion loss.

If the voltage is only applied on the first stage, ideally, the power is received by collimator 10. But actually, $\sin^2\theta_z$ of the total power deviates D_x:

$D_x = 0.274 * 2 * D_z = 0.60$ mm

This deflected light locates at the middle point of the two outputs of 00 and 01.

At that location, both collimators 00 and 01 detect some of the total power. That explains the crosstalk curve in both channel 00 shown in Fig. 5.3.14 and channel 01 shown in Fig. 5.3.15. Since the power is split into two parts for two receivers, the crosstalk of each channel is a little better than the crosstalk caused by the 01 stage.

If the voltage is applied on both stages, ideally, the power is received by collimator 11. But actually, $\sin^2\theta_z$ of the total power deviates D_x:

$D_x = 0.274 * 3 * D_z = 0.90$ mm

This deflected light locates near the center of collimator 01. The power is detected mainly by collimator 01 and in small part by collimator 00. Thus, the crosstalk of channel 00 is better than that shown in Fig. 5.3.12. At the same time, the crosstalk of channel 01 as shown in Fig. 5.3.13 is severe. Since a small part of the power is detected by collimator 10, some power exists in channel 10 as shown in Fig. 5.3.14.

All the analyses above indicate that the polarization directions of the incident light affect the crosstalk, and this influence can be calculated and estimated.

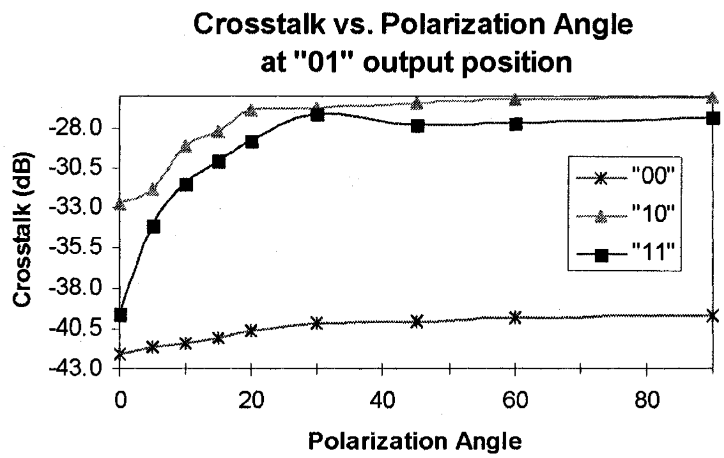

Fig. 5.3.13 Crosstalk vs. polarization angle at the 01 output position

A similar analysis can be conducted for the 01 output position. The crosstalk caused by channel 10 and channel 11 are severe. Channel 00, which is the lower channel, does not affect the higher receivers as Fig. 5.3.11 demonstrates.

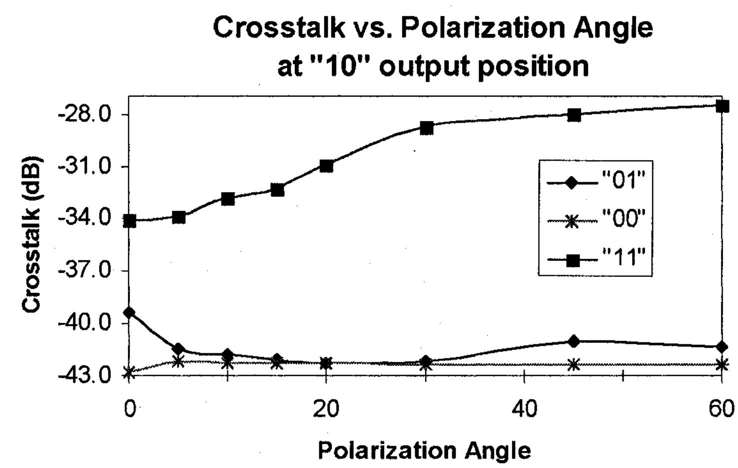

Fig. 5.3.14 Crosstalk vs. polarization angle at the 10 output position

Similar plots and analyses can be derived for the crosstalk at collimator 10 as shown in Fig. 5.3.14.

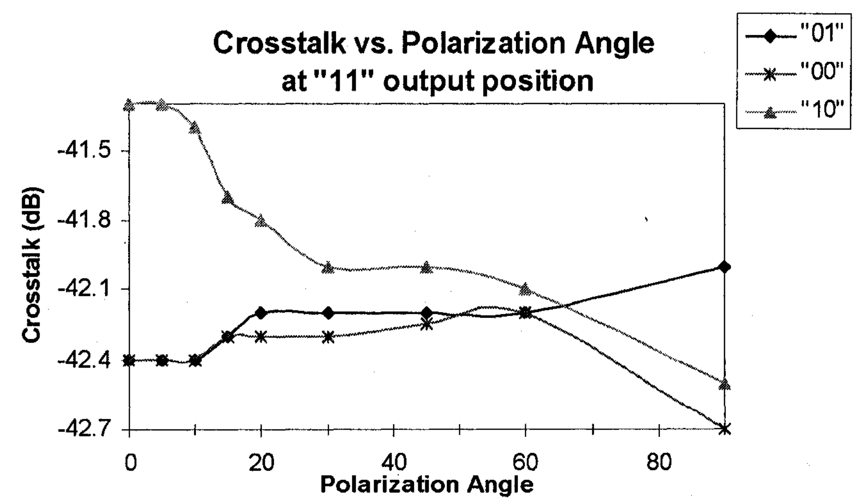

Fig. 5.3.15 Crosstalk vs. polarization angle at the 11 output position

In the 11 output position, none of the channels affect the receiver. All crosstalk are around –42 dB with little change (less than 2 dB) as shown in Fig. 5.3.15. The dropping of the crosstalk in this plot is the result of inaccuracy in the experiment.

The analysis shows that all the polarization extinction ratio values from experiments are reasonable and can be predicted. Also, according to these results, the incident polarization angle should keep within 10° - 15° to maintain a better switching performance with respect to the insertion loss and crosstalk. Thus linearly polarized laser source and polarization maintaining (PM) fiber are required, which have been widely applied in commercial products.

5.3.4 Misalignment Test

In the last two sections, the power meter of the collimators measures the insertion losses and crosstalk. Since any misalignment of the collimator pair affects all the measurements, the tests on the alignment of the collimator pairs are produced in this section. From the experimental results shown later, a strict coupling of the light beam from incident collimator to the receiving collimators is required.

Fig. 5.3.16 Schematic setup for the misalignment test

A test was designed to plot the insertion loss vs. misalignment and the setup is shown in Fig. 5.3.16. To achieve better measurement, an EO device is not present between the pair of collimators. The collimators are at a 100 mm distance from each other, and they are adjusted on the 6 axes stages to achieve minimum insertion loss. By moving the receiving collimator away from its accurate positions along the x-axis, different insertion losses are obtained. The plot of the insertion loss vs. the translational misalignment is shown in Fig. 5.3.17. Similarly, by rotating the receiving collimator through different angles and reading the insertion loss, the plot of the insertion loss vs. the pitch misalignment is obtained as shown in Fig. 5.3.18. Typically, a translational or pitch misalignment of the collimators of 50 μm and 0.04°, respectively, results in an additional loss of approximately 1 dB.

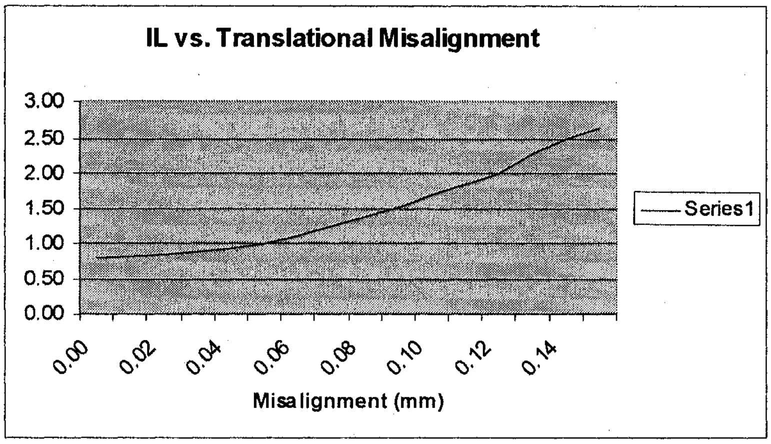

Fig. 5.3.17 Insertion loss vs. translational misalignment

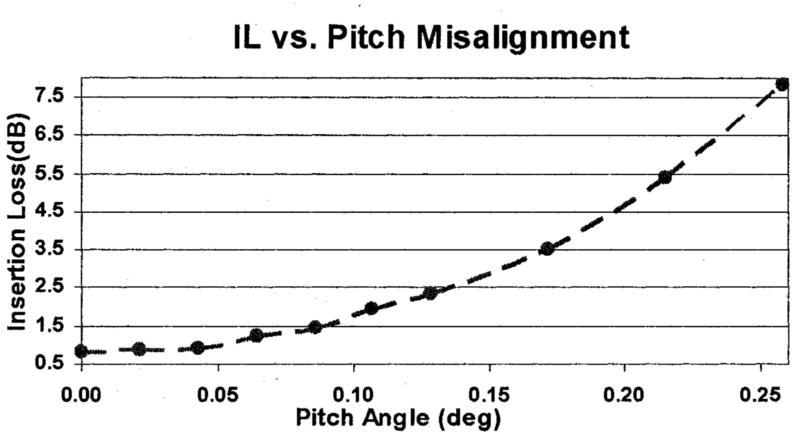

Fig. 5.3.18 Insertion Loss vs. pitch misalignment

Compared to other measurements, the insertion loss caused by misalignment of the collimator pairs is most significant, and so the initial alignment of the collimators must be perfect before producing any other measurements.

5.4 Packaging

Packaging plays a critical role when building a switch. Good packaging not only supports all the optical and electrical components, but also assures the reliability of the optical path and electrical control. The reliability, functionality, and ease of operation are the main considerations of the package.

The design of the mechanical part is first described in section 5.4.1, which includes the consideration of the base, the outer package, and the accessories of the optical and electrical components. The performances of the packaged switches are demonstrated in section 5.4.2, showing the deflection angle, the insertion loss, and crosstalk figures of the 1x2 and 1x4 EO switches.

5.4.1 Design of the package

Acrylic plastic, a commonly used material, was chosen for the package. Acrylic plastics are transparent and can transmit and control light; have superior dimensional stability; and have an excellent combination of structural and thermal properties [3]. In short, most of the properties of acrylic plastics apply to the application of EO switching package.

The whole package is divided into two parts: the inner part (or the base) and the outer part. The base is secured on the outer package using 4 screws. All the optical components, such as the pair of collimators, the EO devices, and the optical prism or mirror sets are all arranged on the base.

The polarization maintaining (PM) fiber collimators, which were purchased from Koncent, are aligned at the input and output of the package and glued to the base by using UV epoxy. The working distance of the PM collimators is 100 mm in air; the extinction ratio is 25 dB; the beam divergence is 0.3 degrees; the beam waist is 0.4

mm; the housing diameter of the metal tube is 1.3 mm; and the housing length is 8 mm. Factoring in the greater refraction index within the EO device and the prism, the required distance between the input and output collimators is 133 mm, as given by:

$$D = (100 - L) + L * n = 100 + (n - 1) * L = 133 \text{ mm}$$

Here, L is the length of the device, which is about 70 mm, D is the moderated distance.

Assuming that the metal tube of the collimators is glued to the base, an extra length should be included in the base. Also, a tolerance in the base length should be considered due to the different lengths of different devices. Thus a base length of 141 mm is determined. By moving the pair of collimators towards the center or away from the center, a shorter or longer EO device can be fitted. The width of the base is 30 mm to fit thinner and wider devices.

A rectangular pit for holding additional optical components is hollowed out 5 mm from the right edge of the base. The pit is 17 mm long, 9 mm wide, and 3 mm deep, a depth which is sufficient for the thickness of the glue (0.5 mm) and the thickness of the optical component.

For safety reasons, a pillar opening is designed on the base to guide the electrical wires, which are connected to the high voltage connectors. This pillar opening has a 3.8 mm radius, a 2 mm depth, and is located 37 mm from the left edge. The high voltage wire from Surplus Sales Inc. can support 5 kV voltages.

Another acrylic container was designed as an outer package to support the base, the connector for the electrical cables, and the fiber pigtail of the collimators. The outer package has a rectangular opening for the base to sit in. This opening is 12.7 mm deep, which is the same depth as the base. Also, it has a total length of 18 cm and a width of 10 cm. Four screws are used to join the outer package and the base together. The fiber pigtail of the collimators is glued on the right and left edges of the outer package. Two SHV cable connectors are fixed on the outer package at the same location as the pillar opening. The electrical power is delivered from the high voltage supplies through these connectors and the electrical wires to the EO devices. The schematic of the package with 1×2 switch on the base is presented in Fig. 5.4.1.

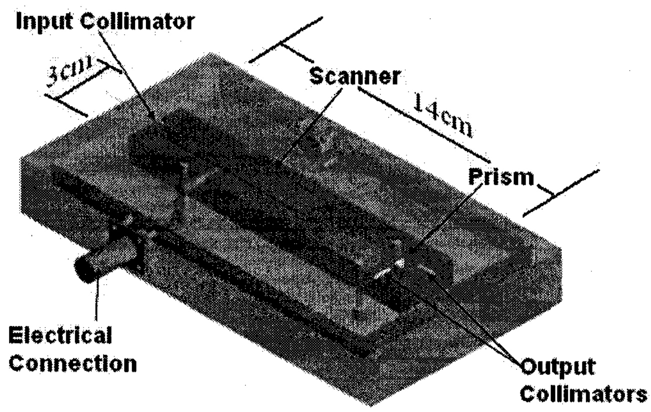

Fig. 5.4.1 Schematic of the 1x2 package

5.4.2 Packaging of 1x2 and 1x4 EO switches

In the 1x2 switching package, the EO crystals, which are 18.5 mm long and 0.57 mm wide, are mounted on the acrylic base. A 0.5 mm thick glass plate is used to help the mounting and ensure the glue thickness. A PM fiber collimator is then aligned and mounted at the left end of the base to serve as the input. Another fiber collimator is mounted at the right end of the base as one receiver, after it is aligned to receive the maximum power without any external E-field.

A knife-edge right-angle prism is incorporated in the 1×2 optical switch package to further separate the two beams at the output. The EO device provides an initial beam separation of 1.9 mm. The beams are directed towards a right-angle prism and then deviated towards the collimator, which is glued on the side of the base. The right angle prism with edge dimensions of 5 mm and a drawing of this right-angle prism is shown in Fig. 5.4.2. The second fiber collimator is mounted at the side edge of the base, after it is aligned to receive maximum power with a proper external E-field. A photo of the packaged 1x2 switch is shown in Fig. 5.4.3.

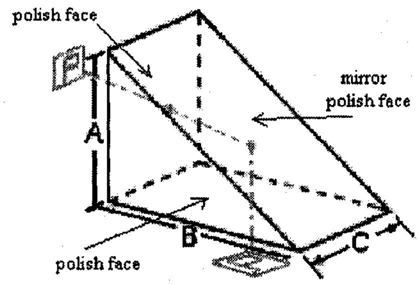

Fig. 5.4.2 Polished faces of the right angle prism

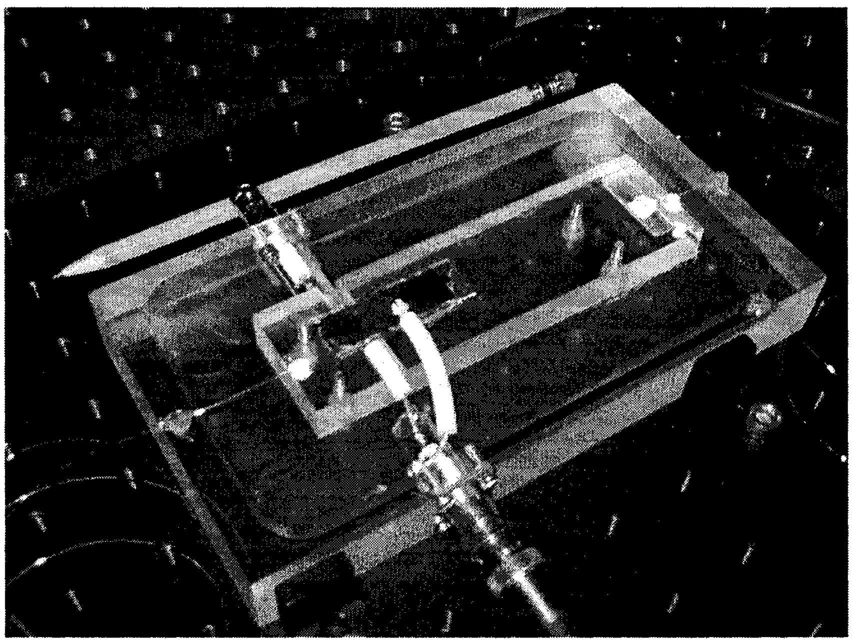

Fig. 5.4.3 Packaged 1x2 EO switch

The packaging of the 1x2 switches is reused in the 1x4 switch. A similar fabrication process was reproduced. A schematic of the 1x4 packaged switch is shown in Fig. 5.4.4 and the photo of the assembled package is shown in Fig. 5.4.5.

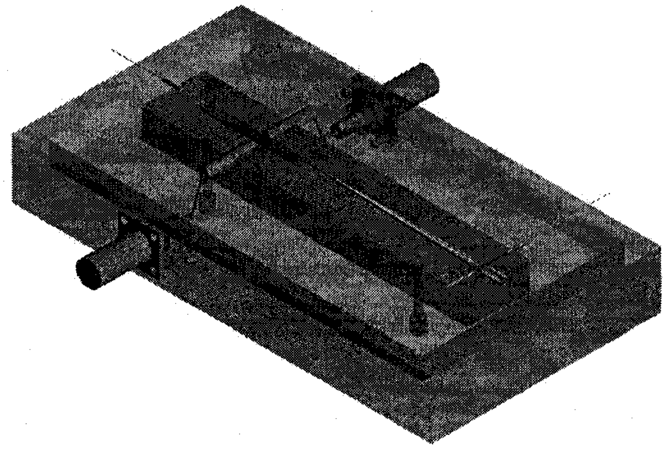

Fig. 5.4.4 Schematic of the 1x4 optical switch

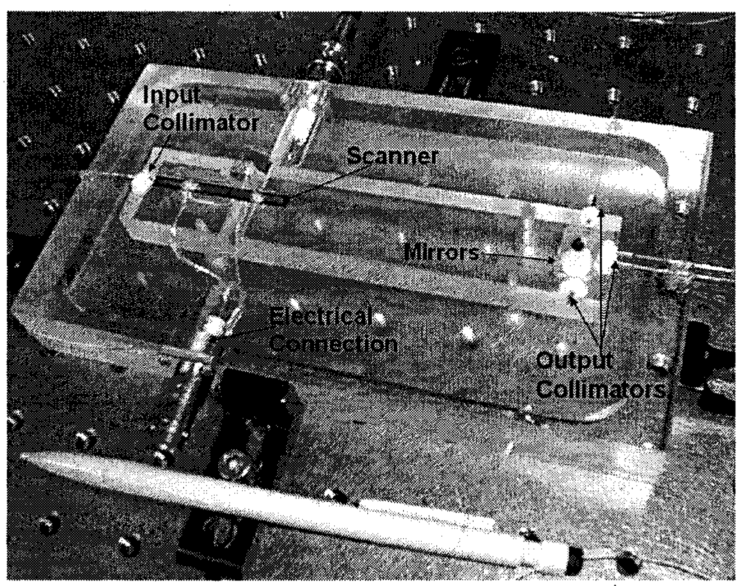

Fig. 5.4.5 Packaged 1x4 Electro-optical switch

Similarly, a special mirror set can provide a greater separation between the four beams in the 1x4 optical switches. By using this special mirror, the 1st spot and the 4th spot can be separated by enough distance (2.8 mm) so that the two parallel collimators can be glued side by side. The optical path of the two center beams are bent 90° to the side edges, which is similar to the bending in the 1x2 packaged optical switches.

This custom mirror set has a "V" shaped groove that is obtained by using two 1.1 mm wide reflective surfaces tilted at 45°. The mirrors work similarly to the right-angle prism and deflect the two center light beams by ±90° toward the collimators glued to the side of the base. The edge beams are unaffected by the prism and pass through to the edge collimators (Fig. 5.4.6). Before entering the prism, the distances between each light beam are measured to be 1.0 mm, 0.9 mm, and 0.9 mm. Given a beam waist of around 0.4 mm, these distances are sufficient. These V shaped mirror sets were produced by JDS Uniphase as custom made products.

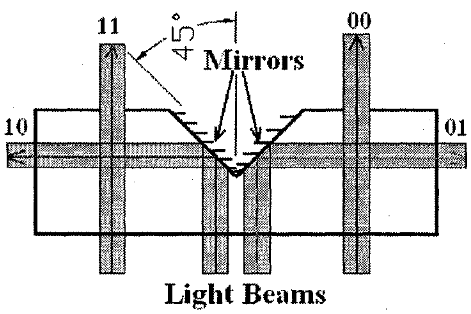

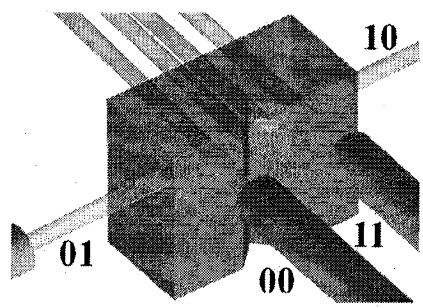

Fig. 5.4.6 Top view and 3D view of the mirror set

5.4.3 Performances of the Packaged 1x2 and 1x4 EO switches

A 1310 nm linearly polarized fiber coupled laser source is used to test the performance of the 1x2 EO switch. The aligned PM fiber input collimator was measured and found to produce a maximum polarization angle misalignment of 2.2° and a polarization extinction ratio of 26 dB. Deflection and power measurements for the packaged switch are shown in table 5.4.1. Since the facets of the deflector are not AR (Anti Reflective) coated, the loss thus caused was calculated and removed from the results. All measurements of the packaged switches were obtained using driving voltages of 1200 V.

Table 5.4.1 Insertion loss and crosstalk of the packaged 1x2 switch

Voltage	Deflection (deg)	Insertion Loss (dB)	Crosstalk (dB)
0	0.00	2.37	-39.24
1200	1.22	3.61	-37.31

Again, this laser source and the PM fiber input collimator are used in the testing of the 1x4 EO switch. Tables 5.4.2 present the insertion loss, crosstalk performance, and deflection angles. Since the facets of the deflector are not AR coated, the loss thus caused is calculated and removed from the results. All measurements are obtained using driving voltages of 1100 V for the 1×4 switch.

Table 5.4.2 Insertion loss, crosstalk, and deflection angle of the 1×4 packaged switch

Switch Stage	Loss (dB) in Collimator Positions (IL in Blue; CT in Black)				Deflection (deg)
	"00"	"01"	"10"	"11"	
"00"	2.9	-24.7	-32.9	-37.8	0
"01"	-40.2	3.7	-37.0	-35.1	0.77
"10"	-39.9	-40.2	2.8	-21.4	1.43
"11"	-40.5	-40.6	-30.4	3.4	2.13

In summary, the 1×2 switch exhibits a best-case insertion loss of 2.4 dB and crosstalk of -39.2 dB. For the 1×4 switch, the obtained values are 2.8 dB and -40.6 dB, respectively.

5.5 High Speed and Damping Test

EO devices provide ultra-fast response time, as discussed in Chapter 2. EO switches based on EO effect demonstrate fast switching times, which is essential in the future all agile photonics networks. EO devices are widely used in digital communications since they can provide 40Gb/s or higher bandwidth. Thus, the bandwidth performances are fundamental in our EO deflectors. In this section, the switching time between different channels of the packaged switches is tested and analyzed, providing the equivalent bandwidth for the application. At the end of this section, a damping test is performed to show how the piezoelectric phenomenon has been overcome.

5.5.1 High Speed Test

Several models as (a), (b), and (c) as shown in Fig. 5.5.1 [4] can be established to simulate the electrical performance of the wafer and the electrodes. To simplify the case, model (a) is chosen. In the model, C1 is low-frequency capacitance, C2 is high-frequency capacitance, and R1 is the wafer resistance related to the temperature parameters, which is large (assuming 1.5 kΩ here). The capacity of the whole wafer can be calculated [5] as:

$$C = \frac{\varepsilon \varepsilon_0 A}{d} \tag{8}$$

where $\varepsilon = 45$; $\varepsilon_0 = 8.85 \times 10^{-12}\ \mathrm{C}^2 / N \cdot m^2$; A is the area of the electrodes; and d is the thickness of the wafer.

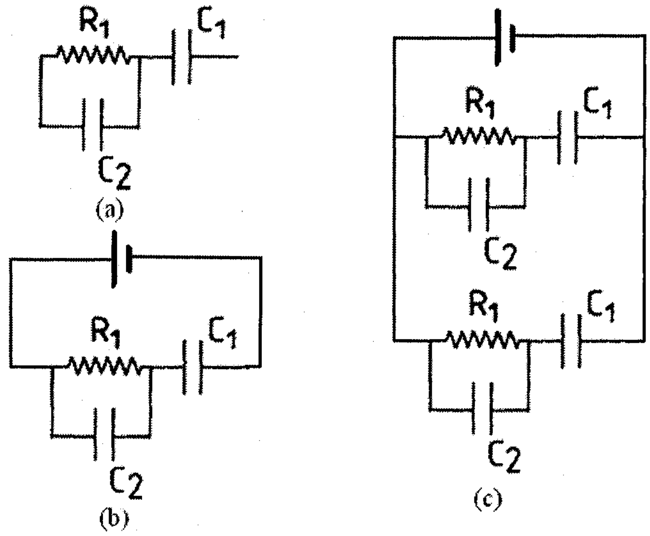

Fig. 5.5.1 Three RC models for the $LiTaO_3$ wafer

The capacities of the two stages can be calculated by measuring the dimension of the driving electrodes:

$$\text{Stage 01: } C_{01} = \frac{\varepsilon\varepsilon_0 A}{d} = \frac{8.85\times10^{-12}\times45\times16.5\times2\times10^{-6}}{0.5\times10^{-3}} = 26pF$$

$$\text{Stage 10: } C_{10} = \frac{\varepsilon\varepsilon_0 A}{d} = \frac{8.85\times10^{-12}\times45\times22.9\times1.6\times10^{-6}}{0.5\times10^{-3}} = 29pF$$

The time constants or effective RC in the circuit of different states are as follows:

$$t_{01} = RC = (R_{source} + R_1)\times C_{01} = 41.4ns$$

$$t_{10} = RC = (R_{source} + R_1)\times C_{10} = 46.2ns$$

$$t_{11} = RC = (R_{source} + \frac{R_1}{2})\times (C_{10} + C_{01}) = 46.4ns$$

From the calculation results, the effective RC time constant of all three states is similar. Therefore, the response time for the channels is almost the same. The experimental value confirms the conclusion as discussed later.

The schematic setup for the high speed test is shown in Fig. 5.5.2. A GigaBERT (Giga Bit Error Rate Tester) generator from Hewlett-Packard is utilized to create 32 MHz 50% duty's rectangular pulses as signal references to both the receiver and the high voltage pulse generator (The signal Generator as shown in Fig. 5.5.2). The receiver is a Communication Signal Analyzer (CSA8000) with two optical models, which can detect optical signals through fiber collimator and transfer them to electrical signals.

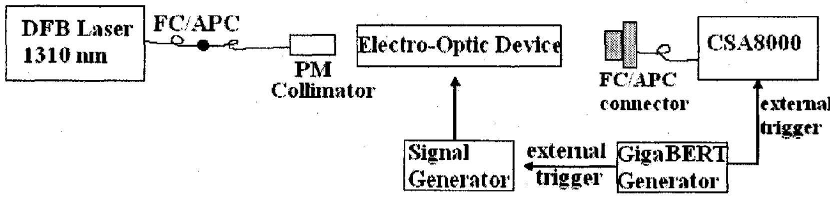

Fig. 5.5.2 Schematic setup for the high speed test

Since the measured switching speed of these devices is limited by the electrical capacitive effects of the $LiTaO_3$ substrate and by the speed of the voltage supply [6], actual speed performance was obtained by measuring the deflection time, which is defined in this context as the time it takes for 90% of the light power emerging from one output collimator to be deflected, and subsequently detected, at the 90% level at a second output collimator. Using this definition, the measured maximum rise time between any two channels is measured to be 86 ns, which corresponds to a maximum switching frequency of 12 MHz. A representative measurement of the switching time obtained as the device is switched between channels 11 and 00 is shown in Fig. 5.5.3 and Fig. 5.5.4.

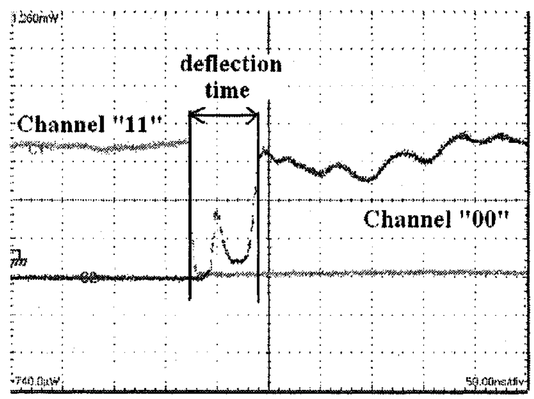

Fig. 5.5.3 Definition of the deflection time when switching from channel 11 to 00

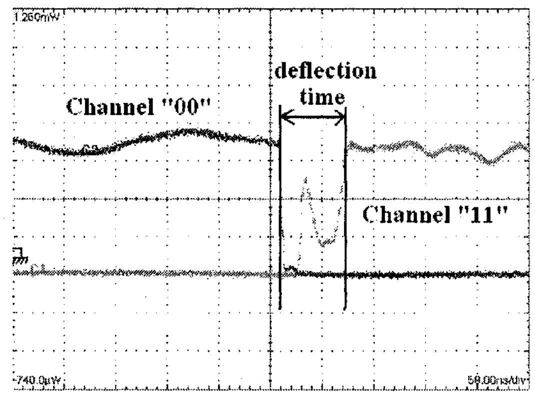

Fig. 5.5.4 Rise and fall time when switching from channel 00 to 11

The deflection time is a little slower when switched between 11 and 00 because the 11 case has a larger equivalent capacitance and resistance than 10 and 01. Also, the distances between the output collimators affect the deflection time. This figure (as well as Fig. 5.5.4, Fig. 5.5.8, and Fig. 5.5.9) is captured from the screen of CSA8000 to demonstrate the response time only; the optical powers of the two input channels haven't been calibrated.

The fall time is much faster than the rise time because of the threshold of the working voltage of the EO device as shown in Fig. 5.5.5. From experiments, the channels expect 00 of the EO devices start to work after the voltage increase over 800 V; and channel 00 stops working after the voltage increase over 200V. Assuming the voltages from the voltage supplier increase and decrease linearly, the voltage changes on the substrates follow the curves shown in Fig. 5.5.6. From the figure, the fall time is much shorter than the rise time. Also, the rising edge will take place after the falling edge, which matches the experimental results shown from Fig. 5.5.3 and Fig. 5.5.4. All the rise time and the fall time are shown in Table 5.5.1.

Table 5.5.1 Measured rise/fall times between channels in the 1×4 packaged switch

Original Channel	Rise/Fall time (ns) to the target channel			
	"00"	"01"	"10"	"11"
"00"	~	46/8	42/7.5	50/7.6
"01"	5/11	~	~	~
"10"	40/14	~	~	~
"11"	40/8.4	~	~	~

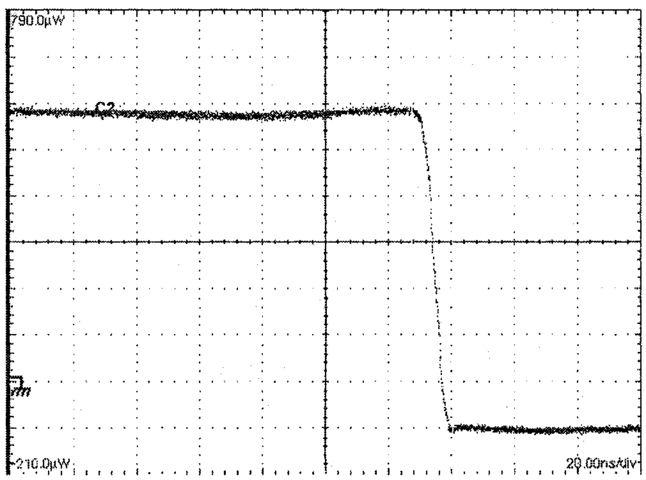

Fig. 5.5.5 Fall time of the 1x4 switch

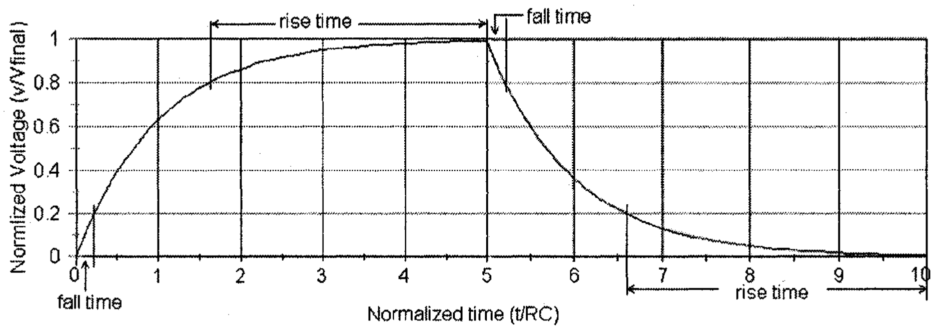

Fig. 5.5.6 RC time constant, rise and fall time

In conclusion, the fastest switching time we obtained was 86 ns, which corresponds to 12 MHz switching frequency. This is limited mainly by the capacity and the electrode structure of the EO device. Instead of the lump electrodes we used here, applying transmission lines with capacity and impedance matching the RF source [7] can provide ever faster switching times or wider bandwidth up to 40 GHz.

5.5.2 Damping Test

The observed ringing phenomenon illustrated in Fig. 5.5.3 and Fig. 5.5.4 occurs due to piezoelectric vibrations of the package. When an electrical signal with high frequency is applied, the device may demonstrate some mechanical vibration due to the soft glues used on the base. The piezoelectric vibration is insignificant when the EO device is tested on the stage without packaging.

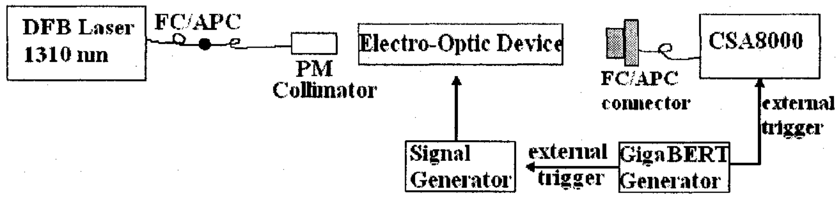

Fig. 5.5.7 Schematic setup for the high speed test

The same setup (Fig. 5.5.7) used for the high-speed test is utilized for the damping test. Several damping materials, such as acoustic-absorbing rubber foam and mineral oil, are fastened on the top of the original electro-optic device to absorb part of the vibration. Fig. 5.5.8 shows the rising edge before and after the attachment of damping material. Results of the ringing at the falling edges are shown in Fig. 5.5.9.

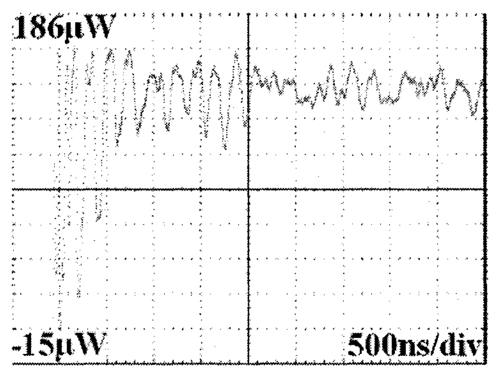

(a)

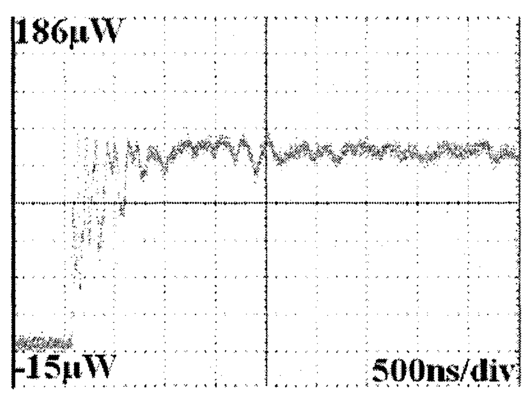

(b)

Fig. 5.5.8 Ringing at the rising edges. (a) before damping, with 32.32% vibration; (b) after the mineral oil damping, with 12.12% vibration.

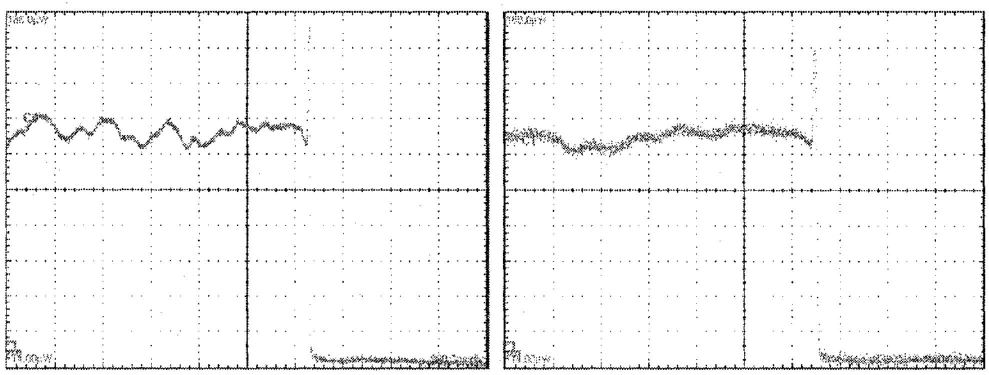

Fig. 5.5.9 Ringing at the falling edges. Left: before damping; Right: after the mineral oil damping.

The power is slightly reduced after damping. The weight of the attached damping material moderately changes the height position of the EO device, affects the optical path, and diminishes the receiving light power.

5.6 Conclusion

To date, the emphasis of existing publications on the EO deflectors has been on scanning applications which do not require fiber-to-fiber packaging. In this chapter, two packaged optical switches that use EO deflectors are reported. By combining these EO deflectors with fiber collimators and high voltage packaging, several multiport packaged high speed optical switches are built and characterized. These switches are 14 cm long and 3 cm wide. The packaged 1×2 optical switches require a driving voltage of 1200 V and exhibits insertion loss of 2.4 dB and crosstalk of -39.2 dB; the 1×4 switch exhibits insertion loss and crosstalk of 2.8 dB and -40.6 dB respectively and operates using a 1100 V voltage source. The maximum deflection time between the channels is 86 ns.

The design of the EO devices and alignment are two essential aspects to produce the packaging of EO switches. The dimensions and positions of the two stages of the 1x4 Electro-optic switches determine the final deflection angles, the additional optical components. And the positions of the receiving collimators. The alignment of the packaging, including the EO deflectors, the input/output collimators, and the optical components, can affect the results greatly.

Some improvements are foreseeable for these packaged optical switches. Several methods applied to the EO devices will reduce the driving voltages. By reducing the voltage to 600 V, mass production or CMOS technology can be used. Also, improvements in the packaging, especially in the alignment, can further reduce the insertion loss and increase the crosstalk in the system. Packaging of 2x2 EO switches which is based on the deflectors introduced in Chapter 4 will also provide improvements.

5.7 References

[1] Y. Zuo, B. Bahamin, E. J. Tremblay, C. Pulikkaseril, E. Shoukry, M. Mony, P. Langlois, V. Aimez, and D.V. Plant, "1x2 and 1x4 Electro-optic Switches," Photonics Technology Letters, Vol.17, No.10, 2080-2082, 2005.

[2] Y. Chiuu, R. S. Burton, D. D. Stancil, and T. E. Schlesinger, "Design and simulation of waveguide electrooptic beam deflectors," *Journal of Lightwave Technology*, Vol. 13, pp. 2049-2052, 1995.

[3] http://www.machinedesign.com/BDE/materials/bdemat2/bdemat2_4.html.

[4] D. C. Sinclair and A. R. West, "Electrical properties of a $LiTaO_3$ single crystal," *Physical Review B*, Vol. 39, pp. 13486-13492, 1989.

[5] A. L. Stanford and J. M. Tanner, *Physics for students of science and engineering*, Orlando: Academic Press, 1985.

[6] B. E. A. Saleh and M. C. Teich, *Fundamentals of photonics*, John Wiley & Sons, Inc., 1991, Chapter 18. pp. 696-736.

[7] E. L. Wooten, K. M. Kissa, A. Yi-Yan, E. J. Murphy, D. A. Lafaw, P. F. Hallemeier, D. Maack, D. V. Attanasio, D. J. Fritz, G. J. McBrien, and D. E. Bossi, "A Review of Lithium Niobate Modulators for Fiber-Optic Communications Systems," IEEE Journal of Selected Topics in Quantum Electronics, Vol. 6, No. 1, pp. 69-82, 2000.

Chapter 6: Discussion, Conclusion, and Future Work

6.1 Introduction

In the bulk EO deflectors, two main concerns arise. The first is the driving voltage. To assist the beam bending, an E-field is applied. All the voltages and the E-field in the previous chapters are above 1000 V, which is high for normal circuit design.

Several methods are introduced in this chapter to reduce the control voltages. In the end, 600 V's control is possible, which is within the range of CMOS circuit design.

Our second concern is that, during the experiments, the experimental results did not perfectly coincide with the expected theoretical values, especially in the EO deflectors with new geometries. As explained before, this mismatch may be a result of the poling. Therefore, in this chapter, details are provided as to how the electric field poling affects the EO materials.

6.2 Methods for Reducing the Voltage

The high driving voltages are always a problem with EO devices. In our devices, 1200 V and 1100 V driving voltages are required. To industrially manufacture packaged switches, lower driving voltages are needed. In this section, several methods for reducing the driving voltage are proposed.

6.2.1 Changing the Device Shape

The optimal designs in chapter 4 can be used to reduce the driving voltages. EO devices using the parabola shape can achieve a given deflection angle with less voltage than rectangular devices of the same length The following equations explain in detail the voltage requirements of the parabola shaped device:

$$\text{Since } \theta = \frac{\Delta n}{n}\frac{L}{WH} \text{ and } \Delta n = n_0^3 r_{33}\frac{V}{D} \tag{1}$$

$$\theta = n_0^2 r_{33}\frac{L}{WH}\frac{V}{D} \tag{2}$$

$$\text{Thus, } V = \frac{D}{n_0^2 r_{33}}\frac{WH}{L}\theta \tag{3}$$

where, *WH* is the width of the device, *L* is the length of the device, *D* is the thickness of the device, and θ is the deflection angle of the device.

For example, when comparing the parabola shaped device to the rectangular shaped device (both having the same dimensions and total deflection angle), *WH* is much smaller in the parabola deflectors, which results in the smaller *V*.

A similar effect can be achieved with the half-horn shaped device, and the control voltage in that device can be reduced as well.

$$\theta = \sqrt{\frac{2\Delta n}{n_0}\ln(\frac{W(L)}{W_0})} \qquad \Delta n = n_0^3 r_{33}\frac{V}{D} \tag{4}$$

$$\theta^2 = 2n_0^2 r_{33}\frac{V}{D}\ln(\frac{W(L)}{W_0}) \tag{5}$$

Thus, $$V = \frac{D}{2n_0^2 r_{33}\theta^2 \ln(\frac{W(L)}{W_0})} \tag{6}$$

6.2.2 Thinner Wafer

Both (3) and (6) have a factor of D, which is the thickness of the wafer. By choosing a thinner wafer, such as a 300 μm thick instead of a 500 μm thick wafer, the control voltage can be reduced to 0.6 of the original value.

However, according to the properties of the wafers described in chapter 3, thinner wafers are more fragile, which introduces more difficulties in the fabrication and poling procedures.

The 300 μm wafers were acquired, photolithographed, and metallized successfully at Sherbrooke University. Successful poling also was accomplished in the lab after initially cracking some substrates. Several recommendations should be followed when poling and handling thin wafers.

- On the wafers, do not press the spring probe against the electrodes. Connect the black lead of a Volt Ohm Meter to the probe. Replace the red lead with the Nano-clip contact and lead out to touch the electrodes on the wafer. This Nano-Clip has an extremely soft hook and can protect the wafer from pressure as Fig. 6.2.1 shows. Push the spring probe down more slowly until it finally touches the electrodes. Monitor the whole procedure on the screen of the monitor using a CCD camera.

- Always leave a layer of foam above and below the wafer when storing it. Avoid violent movements when handling it.
- Increase the first high voltage supply in very small steps to avoid cracking the wafer when poling.

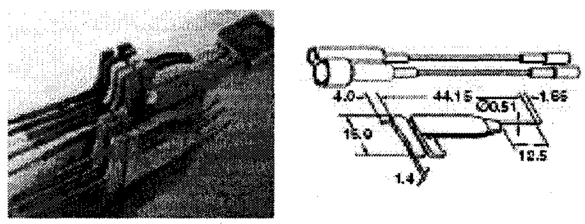

Fig. 6.2.1 Photo of the nano-clip

Our tests have shown that it is possible to develop EO switches on thin wafers and thus reduce the control voltage to 600 V.

EO devices based on waveguide have lower driving voltages because they have only a 10-50 μm layer of $LiNbO_3$ or $LiTaO_3$. With that thickness, the driving voltages can be reduced to 20-100 V or even lower.

6.3 Poling Theory

Although Poling, especially electric field poling, has been widely used in the production of the EO devices, the mechanisms of electric field poling are still under study.

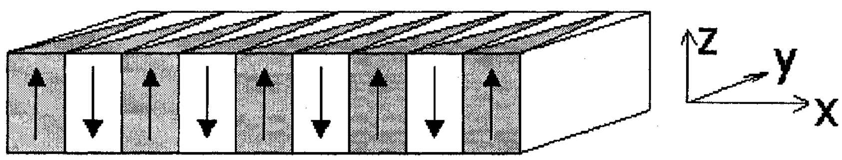

Fig. 6.3.1 The interfaces of the two domains

Studies in [1] – [4] show that the inversed domains grow from small triangular domains within the domain walls perpendicular to the surface as shown in Fig. 6.3.2. By merging these small triangular domains, the whole designed area of the inversed domains can be created. Due to the basic triangular structure, prisms in rectangular shaped deflectors can be created more accurately. Thus, the nonrectangular shaped deflectors might produce an imperfect domain inversion, and the deflection performance may be affected.

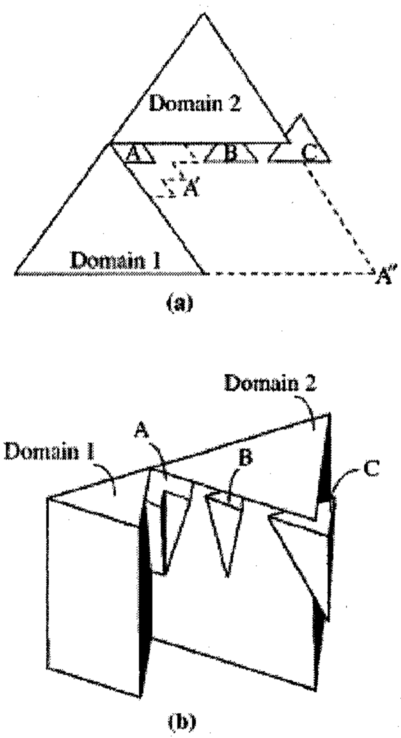

Fig. 6.3.2 Small triangular domains and their merger [2].

6.4 Conclusions

Optical switches are important devices for future agile all-photonic networks that reconfigure on nanosecond time scales and that are based on electronic control. Continually evolving Internet and telecommunication networks require not only larger communication bandwidth, but also faster switching times. For this reason, optical switching technology has become one of the hottest research topics over the past decade. A subset of the current optical switches is a device built from bulk electro-optic (EO) materials, which can provide both high speed and moderate deflection.

Although optical switches such as MEMS have been widely applied to commercial networks, they cannot satisfy the requirement for dynamic provision. Electro-optical switching promises higher speed and a wider flexibility, both of which are essential to the next generation of optical networks. This present study has proposed new designs for packaged optical core switches, which are based on electro-optic deflectors. In addition to having large bandwidth capabilities, low insertion losses, and a fast response time, the devices are generally compact and can be easily fabricated and readily integrated.

Optical switches based on the EO effect are some of the fastest switches demonstrated to date. Two packaged EO switches, ultra-fast 1×2 and 1×4 optical switches, have been successfully fabricated in the lab. The obtained devices are fully characterized. The implementation of a low insertion loss, moderate crosstalk switch capable of sub-nanosecond switching times has been demonstrated. The packaging of these switches is 14 cm long and 3 cm wide. The ultra-fast packaged 1x2 optical switch has a deflection angle of 1.22° with an applied voltage of 1.1 kV. The insertion loss and crosstalk figures are 2.36 dB and -36 dB, respectively. With an applied voltage of 1 kV, the ultra-fast packaged 1x4 optical switch has deflection angles of 0.77°, 1.43°, and 2.13° for the 01, 10, and 11 channels, respectively. The insertion losses are around 3 dB, and the crosstalk is approximately –27 dB. The maximum deflection switching time between the channels is 86 nsec.

In this dissertation, existing theories pertaining to the EO effect are extended, and new EO deflectors are designed. The equivalence of the prism and gradient index analysis is given for nonrectangular shaped devices. The limitations or boundaries of the deflection angles achieved by the rectangular devices are calculated for the first time. Among the two new EO deflectors proposed in chapter 2, the parabola shaped device demonstrated the optimal deflection angle and best sensitivity. When compared to the rectangular shaped devices, the half-horn shaped device achieved better performance in the deflection angle. The parabola shaped and half-horn shaped deflectors provide 2-3 degrees of steering, which is 2-3 times better than the rectangular devices.

Based on the parabolic and the half-horn geometries, novel optical deflectors were successfully designed, built, and tested. These deflectors have the potential to build non-blocking 2x2 optical switches as described in the dissertation. Due to the requirement of precision alignment, different free space tests of different parts of the 2x2 switches were developed. The results of these tests show that 2x2 optical switching is accomplished.

Finally, efforts have been made to reduce the driving voltage requirements of current EO devices. The poling theories are briefly discussed.

6.5 Future Work

Based on the existing parabola shaped and half-horn geometry optical deflectors, non-blocking 2x2 optical switches will be manufactured and packaged soon. The same inner and outer package described in chapter 5 will be reused. With enough deflection angles ensured by the design of the new shapes, additional optical components are not needed. Two PM collimators will be aligned and glued as the inputs, and an additional two will serve as the outputs at the other end. Insertion loss, crosstalk, and the switching time from channel to channel will be tested.

Since procedures such as photolithography, metallization, and poling already have been tested on the thin wafers, EO devices will be fabricated on thin wafers in the next step to reduce the driving voltage. With a wafer thickness of 300 μm, driving voltage can be reduced to 600 V or even lower.

The new geometries of the parabola and half-horn shape will later be tested in waveguide devices. With a thin layer of $LiNbO_3$ or $LiTaO_3$ material, which is around 10 - 50 μm in thickness, the steering performance will be achieved under 30 V. Applications of these waveguide devices that incorporate the new shapes will be developed.

At the same time, more wafers will be poled to compare the effect of the electric field poling in the deflection performance. A combined study and research project on the poling theories is ongoing with the Physics Department at McGill University.

6.6 References

[1] V. Gopalan and M.C. Gupta, "Origin of internal field and visualization of 180° domains in congruent $LiTaO_3$ crystals," *Journal of Applied Physics,* Vol. 80 pp. 6099-6106, 1996.

[2] V. Gopalan, T.E. Mitchell, "In situ video observation of 180° domain switching in $LiTaO_3$ by electro-optic imaging microscopy," *Journal of Applied Physics,* Vol. 85, pp. 2304-2311, 1999.

[3] V. Gopalan, Terence E. Mitchell, "Wall velocities, Switching times, and stabilization mechanism of 180° domains in congruent $LiTaO_3$ crystals," *Journal of Applied Physics,* Vol. 83, pp. 941-954, 1998.

[4] V. Gopalan, S. S. A. Gerstl, A. Itagi, Q. X. Jia, T. E. Mitchell, T. E. Schlesinger, D. D. Stancil, "Mobility of 180° domain walls in congruent $LiTaO_3$ measured using in-situ electro-optic imaging microscopy," *Journal of Applied Physics,* Vol. 86, pp. 1638-1646, 1999.

Appendix: Matlab program depicting AutoCAD masks

```
"fid= fopen('horn_mask.scr','w');              //open a new file.
fprintf(fid,'pline\n');                         //"pline is a AutoCAD command"
fprintf(fid,'%f,%f\n',x(1)*1e6,y1(1)*1e6);      //draw the first point in AutoCAD

while 1
    I = find(y1(i0 : end) - y(i0 : end) > 0) + i0 - 1;
    if length(I) > 0
        cnt = cnt + 1;
        i = I(1);
        y1(i : end) = 2 * y1(i) - y1(i : end);  //Calculate the next point
        fprintf(fid,'%f,%f\n',x(i)*1e6,y1(i)*1e6);
//draw the line to the next point in AutoCAD
        d = 2 * i - i0;
        if d>length(x)
            break
        end
        y1(d : end) = -y1(d : end);
        fprintf(fid,'%f,%f\n',x(d)*1e6,y1(d)*1e6);
//draw the line to the next point in AutoCAD
        i0 = d;
    else
        break
    end
end
```

```
fprintf(fid,'%f,%f\n',x(end)*1e6,-75);      //draw the last point in AutoCAD
fprintf(fid,'%f,%f\n',0,-75);
fprintf(fid,'%f,%f\n',0,0);
fprintf(fid,'C\n');                         //end of the Pline command
fclose(fid)                                 //close the AutoCAD file."
```

Acknowledges

First of all, I would like to thank my supervisor Prof. David V. Plant. He is brilliant, knowledgeable, insightful, and most importantly, always available. In the past five years, he not only taught me the knowledge, the lab experiences, and other aspects in research works. I learned the art of research and the philosophy behind it from him. My presentation abilities are improved greatly under his guidance. Besides the academic, I learned ways to be better human beings. I really enjoyed the studies under his supervision and I feel very lucky to have an adviser as humorous as him.

Many thanks to Prof. Vicent Amiet from Sherbrooke University. All the wafer fabrications, including the photolithograph and matellization are done under his supervision. He also helps a lot on my publications.

I would also like to express my deepest gratitude toward the other members of my committee, Prof. Lawrence Chen and Prof. Jan Bajcsy, for the helpful discussions throughout the course of the thesis. For that, I sincerely thank them.

Let me take this opportunity to acknowledge to some previous and current members of Photonics System Gourp. Madelan Mony discussed with me a lot in techniques, knowledge, lab experiments, and etc. She helped doing experiments, writing of my articles, and we shares the fun conference trips together. Previous PSG members Erric T, Cibby S, Babak B, and Ehab A, who had taken part in the same projects, helped a lot in both the testing and the documents writing. Without them, the projects can never be finished. I also appreciate the suggestions, in both academic and fabrication, from Po Dong and Bakhtazad Aref.

I thank all members of the Photonics System Group for making it a second home for me. Prof. Andy Kirk helped me in the reviewing of academic articles and gave me professional suggestions on my publications. Other members of PSG such as Eric B and Chris Roston also help me in the facilities, and computer settings.

One thousand thanks to my husband Mr. Ren Wu. I don't think I can thank him enough. This dissertation would not be the way it is without him. He was the 1st audience for many of my ideas. He provided useful suggestions and encouraged me whenever I faced difficulties. Without his support on the research work, as well as the housework throughout the ups and downs on this long Ph.D road, I could never finish it.

Finally, I really appreciate the financial support from the organization of Agile All Photonics Networks (AAPN) all these years.